

FINAL REPORT (Revised)
A FAST 4-D TEM SYSTEM FOR UXO CHARACTERIZATION

D.D. Snyder, Scott C. MacInnes, Jennifer L. Hare
Zonge Engineering & Research Organization
Tucson, AZ



ESTCP Project No. 200105

July 30, 2003



Zonge Engineering & Research Organization, Inc.
3322 East Fort Lowell Road, Tucson, AZ 85716 USA
Tel: (520) 327-5501 Fax: (520) 325-1588 Email: zonge@zonge.com

Report Documentation Page				Form Approved OMB No. 0704-0188	
Public reporting burden for the collection of information is estimated to average 1 hour per response, including the time for reviewing instructions, searching existing data sources, gathering and maintaining the data needed, and completing and reviewing the collection of information. Send comments regarding this burden estimate or any other aspect of this collection of information, including suggestions for reducing this burden, to Washington Headquarters Services, Directorate for Information Operations and Reports, 1215 Jefferson Davis Highway, Suite 1204, Arlington VA 22202-4302. Respondents should be aware that notwithstanding any other provision of law, no person shall be subject to a penalty for failing to comply with a collection of information if it does not display a currently valid OMB control number.					
1. REPORT DATE 30 JUL 2003		2. REPORT TYPE Final		3. DATES COVERED -	
4. TITLE AND SUBTITLE A Fast 4-D TEM System for UXO Characterization				5a. CONTRACT NUMBER	
				5b. GRANT NUMBER	
				5c. PROGRAM ELEMENT NUMBER	
6. AUTHOR(S) D.D. Snyder, Scott C. MacInnes, Jennifer L. Hare				5d. PROJECT NUMBER UX 0105	
				5e. TASK NUMBER	
				5f. WORK UNIT NUMBER	
7. PERFORMING ORGANIZATION NAME(S) AND ADDRESS(ES) Zonge Engineering & Research Organization, Inc. 3322 East Fort Lowell Road Tucson, AZ 85716				8. PERFORMING ORGANIZATION REPORT NUMBER	
9. SPONSORING/MONITORING AGENCY NAME(S) AND ADDRESS(ES) Environmental Security Technology Certification Program 901 N Stuart Street, Suite 303 Arlington, VA 22203				10. SPONSOR/MONITOR'S ACRONYM(S) ESTCP	
				11. SPONSOR/MONITOR'S REPORT NUMBER(S)	
12. DISTRIBUTION/AVAILABILITY STATEMENT Approved for public release, distribution unlimited					
13. SUPPLEMENTARY NOTES The original document contains color images.					
14. ABSTRACT					
15. SUBJECT TERMS					
16. SECURITY CLASSIFICATION OF:			17. LIMITATION OF ABSTRACT UU	18. NUMBER OF PAGES 100	19a. NAME OF RESPONSIBLE PERSON
a. REPORT unclassified	b. ABSTRACT unclassified	c. THIS PAGE unclassified			

TABLE OF CONTENTS

LIST OF FIGURES	iv
LIST OF TABLES	viii
1. INTRODUCTION.....	1
1.1 Background.....	1
1.2 Objectives of the Demonstration	3
1.3 Regulatory Drivers.....	3
1.4 Stakeholder/End-User Issues	4
2. TECHNOLOGY DESCRIPTION.....	5
2.1 Technology Development and Application	5
2.2 Hardware.....	7
2.2.1 Antenna Cart Subsystem.....	7
2.2.2 NT-32 ^{II} Transceiver Subsystem.....	9
2.2.3 Data Acquisition Software.....	11
2.2.4 Cart Attitude Subsystem	13
2.2.5 GPS Navigation Subsystem	14
2.3 DNT DATA PROCESSING.....	15
2.3.1 Overview.....	15
2.3.2 Merge Data.....	15
2.3.3 Quality Control	17
2.3.4 Background Response.....	19
2.3.5 Target Picking.....	20
2.3.6 Physics-Based Target Modeling	20
Point Anisotropic Dipole Model.....	20
Parameterization of Principal Polarization Transients.....	22
2.3.7 Implications for UXO Classification	23
Model Parameter Summary Plots	25
Blossom Point Ranking Metric.....	29
2.4 Previous Testing of the Technology	29
2.4.1 Blossom Point	31
2.4.2 Fort Ord.....	32
2.5 Factors Affecting Cost and Performance.....	32
2.5.1 Capital Equipment Costs.....	32
2.5.2 Crew Size	32
2.5.3 Survey Speed	32
2.6 Advantages and Limitations of DNT	33
2.6.1 Background Noise levels	34
2.6.2 Horizontal Components Improve Relative Locations.....	35
2.6.3 Physics-Based Parameterization	37

3. DEMONSTRATION DESIGN	41
3.1 Performance Objectives	41
3.2 Selecting Test Sites	41
3.3 Site History/Characteristics	42
3.4 Present Operations	42
3.5 Pre-Demonstration Testing and Analysis	43
3.6 Testing and Evaluation Plan	43
3.6.1 Demonstration Set-Up and Start-Up	43
3.6.2 Period of Operation	44
3.6.3 Area Characterized	44
3.6.4 Operating Parameters	46
3.6.5 Experimental Design	46
3.6.6 Sampling Plan	47
Data (Sample) Acquisition	47
Data Quality Parameters and Indicators	48
Experimental Controls	49
Quality Control Procedures	49
Quality Control Indicators	51
Sample Analysis	54
3.6.7 Demobilization	58
4. PERFORMANCE ASSESSMENT	59
4.1 Performance Criteria	59
4.2 Performance Confirmation Methods	59
4.3 Data Analysis, Interpretation, and Evaluation	60
4.3.1 The Calibration Lanes	61
Target Detectability	62
Target Parameterization	63
Aberdeen Parameterization Summary	71
Aberdeen Ranking Metric	72
4.3.2 The Blind Test Grid	75
ATC Scoring Report	75
Discrimination Stage Ranking Using Multivariate Statistics	76
4.3.3 The Open Field	78
5. COST ASSESSMENT	79
5.1 Baseline System Cost Comparison	80
6. CONCLUSIONS AND RECOMMENDATIONS	81
7. IMPLEMENTATION ISSUES	84
8. REFERENCES	85
9. POINTS OF CONTACT	89
SIGNATURE	90
APPENDIX	91

LIST OF FIGURES

- Figure 1.1:* An early deployment of NanoTEM for an environmental survey in Tucson, AZ. The system as shown uses a 20-m fixed-loop transmitter and a 1-m roving receiver loop (above the instruments).
- Figure 1.2:* Demonstration of 4D NanoTEM at the Idaho National Engineering Laboratory in 1996. The demonstration used a 20-m fixed loop transmitter and a 3-axis roving receiver shown in background.
- Figure 2.1:* Schematic illustration of a TEM transmitter current waveform (green curve), the EMF induced in the target (red), and the resulting secondary magnetic field measured at the receiver loop (blue).
- Figure 2.2:* Photograph of the sled-mounted DNT antenna system deployed in Gambell, Alaska (St. Lawrence Island) in 2000. The targets were discarded ammunition and other metal objects dumped in a 20-ft deep lake.
- Figure 2.3:* A large (3m x 3m) DNT antenna array mounted on caster wheels. The antenna system includes a 3-axis receiver antenna array. It is being used to detect failures in a large concrete sewer main in Tucson, Arizona (October, 2002)
- Figure 2.4:* Photograph of DNT system operating at Blossom Point (December, 2001).
- Figure 2.5:* Block diagram of the DNT system
- Figure 2.6:* Photograph showing two recent versions of cart-mounted DNT antenna arrays. The cart in the foreground is assembled from lightweight fiberglass tubing and weighs only 47 lbs. The cart in the background is manufactured from fiberglass channel beams. It weighs more than 80 lbs.
- Figure 2.7:* Photograph of GDP-32^{II} multi-function receiver as configured for DNT data acquisition. The side access panel has been removed to expose the NT-32 circuit boards that comprise the imbedded NanoTEM transmitter.
- Figure 2.8:* Photograph showing setup for time synchronization of the NT-32^{II} using a SynpaqIII (Synergy Systems, San Diego) with Motorola UTM+ GPS engine.
- Figure 2.9:* A log-log plot diagram illustrating the boundaries of the 31 Zonge Standard NanoTEM time gates. The figure shows the standard EM-61 time gate for reference. Also shown is a set of theoretical transient responses for a small conductive and permeable sphere. Magnetic permeability is the curve parameter.
- Figure 2.10:* Compass/Tiltmeter package shown mounted on the DNT antenna cart.
- Figure 2.11:* Block diagram showing major data elements and processing modules used in DNT data processing.
- Figure 2.12:* The frequency-domain spectra of a \cos^2 window for decimation by four (solid green line) and for a four-point rectangular window (dashed black line).
- Figure 2.13:* Transient data are smoothed along line with a low-pass filter before decimation by an integer factor, in this case decimation by four.
- Figure 2.14:* Calibration ball latency test profiles. In the top profiles, we have plotted the test data with respect to time (fiducial number). In the bottom profile, the data are plotted as a function of UTM Easting.

- Figure 2.15:* Profiles illustrating the change in the behavior of vertical field response (green) and along track horizontal response (blue) as a function of target attitude.
- Figure 2.16:* Illustration of background removal from raw TEM data (vertical field) at Aberdeen. The top set of profiles show dBu/dt . And the bottom pair show dBw/dt data. The top set of profiles for each pair represent the 31 gates of the DNT data. The bottom profiles for each pair are the 31 residual profiles after background removal.
- Figure 2.17:* Schematic of anisotropic point-dipole model.
- Figure 2.18:* Map of companded vertical dBw/dt field for an intermediate composite time gate over Blossom Point.
- Figure 2.19:* Polarizability transients for a 16 lb shotput show the symmetry expected for a spherical object, $\text{dPu}/\text{dt} = \text{dPv}/\text{dt} = \text{dPw}/\text{dt}$. Pasion model b values > 0.8 indicate a permeable object.
- Figure 2.20:* Polarizability transients for a permeable plate indicate the plate's disk-like symmetry with $\text{dPu}/\text{dt} < \text{dPv}/\text{dt} = \text{dPw}/\text{dt}$.
- Figure 2.21:* Polarizability transients for a Mk23 indicate a ferrous cylindrical object with rod-like symmetry. Pasion model b is greater than 0.8, indicating a permeable object and longitudinal polarizability dPu/dt is greater than two nearly equal transverse polarizability responses, $\text{dPv}/\text{dt} = \text{dPw}/\text{dt}$.
- Figure 2.22:* Model parameters from inversion of Blossom Point North-South DNT Cart data with target (x,y,z,h,p,r) fixed at known values.
- Figure 2.23:* Separation of targets at Blossom Point using shape-based discrimination parameters $d1$ and $d2$.
- Figure 2.24:* Early versions of the DNT antenna cart.
- Figure 2.25:* RMS noise levels at Aberdeen by DNT acquisition channel and vector component.
- Figure 2.26:* Vector plot (left) showing horizontal DNT field over cell D12, Calibration Lanes, Aberdeen. In the right hand panel, we overlay the vector plot on a color map of the vertical field.
- Figure 2.27:* Discrimination ROC curves for Blossom Point showing relative performance for single component and multi-component DNT data.
- Figure 2.28:* RMS noise levels at Blossom Point (N-S lines) by DNT acquisition channel and vector component.
- Figure 2.29:* DNT map of DNT vertical response (12-21 composite gate = $68 \mu\text{s}$) of Zonge Ajo test site.
- Figure 2.30:* Figure showing relative accuracy for parameter estimation with DNTDipole for various receiver antenna configurations.
- Figure 3.1:* Gantt chart illustrating schedule of activities.
- Figure 3.2:* Color intensity map of the *Calibration Lane* grid at the ATC Standardized Site. Target locations have been marked and annotated with an abbreviation for their identity.

- Figure 3.3:* Satellite photograph (1 m resolution) showing the outline of the Standardized Test Site. The figure identifies the surveyed grids by number, and other areas or features of interest by letter.
- Figure 3.4:* Primary field direction in the vertical plane through the center of a 1-m square transmitter coil. The O and X at Depth=0 indicate the position of the transmitter wire segments.
- Figure 3.5:* Photograph of DNT survey operation underway at the Fort Ord ODDS site. The photograph shows the lane markers at 2-m intervals. For reference, the width of the transmitter antenna is 1 m.
- Figure 3.6:* Figure showing line coverage over Calibration Lanes at Aberdeen. The circles have a radius of 1 m and they are centered on populated target cells. The figure illustrates how a lane density of $\frac{1}{2}$ -m will intersect a 2-m diameter target “foot print” with 4 to 5 lines.
- Figure 3.7:* Photograph showing passive NT Calibrator circuit connected to the NT-32^{II} transceiver.
- Figure 3.8:* Calibrator response as a function of demonstration day for NanoTEM gate 12 (~25 us after current turn-off). The figure shows a systematic difference between the 3-channels in the early time response.
- Figure 3.9:* An example calibration run standard response plotted against time. The red profile is an Intermediate time composite gate for the vertical channel ($uVsum3 = dBz/dt$, windows 12-21), and the green profiles are the 31 channels of the complete vertical field transient. The first peak is generated by passing one direction over the test sphere, the second peak from passing over target in the opposite direction, and the plateau is from parking the cart directly over the target for a 30 second static occupation.
- Figure 3.10.* An example calibration run standard response plot for the vertical component, dBz/dt , composite windows 12-21 ($uVsum3$).
- Figure 3.11.* An example of unstable system response in DNT data from a calibration run made without sufficient system warm-up time. $UVsum3$ is the vertical component, dBz/dt , composite windows 12-21.
- Figure 3.12.* Standard response histograms for beginning session (top) and ending session (bottom) calibration runs from the Aberdeen DNT survey. Note that while the variances are similar, there is a small, about 2%, bias in the mean standard response for ending sessions compared to beginning sessions.
- Figure 3.13.* Static (green) and dynamic (red) GPS position estimates for the calibration target. The 'true' position (black circle) was taken as the mean of 120 static GPS occupations and has a standard error of about 0.5cm. The dynamic position estimates are based on the calibration target peak anomaly location from the merged DNT data and have a standard deviation of 10 cm. Note also that there is approximately 19cm bias in the dynamic estimates.
- Figure 3.14:* A receiver operation curve (ROC) for DNT data acquired over the Calibration Lanes at ATC. The knee of the curve, shown at about 7dB signifies that the optimum threshold of detection is at $0.12 \mu V/A\text{-m}^2$ where the RMS background noise level has been estimated to be at $0.05 \mu V/A\text{-m}^2$.

- Figure 3.15:* Function used to affect bipolar companding. When scaled as indicated in the formula, the function approximates the signal-to-noise ratio (SNR) expressed in dB for $\text{SNR} > 1$.
- Figure 3.16:* DNT profiles at Early ($10 \mu\text{s}$) and Intermediate ($68 \mu\text{s}$) time composite gates illustrate improved SNR at early times.
- Figure 4.1:* Figure showing the cell numbering convention in the Calibration Lanes at ATC.
- Figure 4.2:* Figure summarizing the maximum DNT detection depth for targets in the Calibration Lanes at ATC.
- Figure 4.3:* Polarizability plots for clutter-masked 60mm targets at the Calibration Lanes of the Standardized Test Site at ATC.
- Figure 4.4:* Polarizability plots for clutter-masked 60mm targets at the Calibration Lanes of the Standardized Test Site at ATC.
- Figure 4.5:* Polarization plots for the steel disks located in Cells B-11, F-11, and H-11 at the west end of the Calibration Lanes, ATC Standardized UXO Demonstration Test Site
- Figure 4.6:* Polarization plots for the T62 AT Mines located in Cells F-15 and H-15 at the west end of the Calibration Lanes, ATC Standardized UXO Demonstration Test Site
- Figure 4.7:* Histogram showing range of estimates of target depth and polarization amplitude (P_0) for a population of 49 8-lb shotputs located in the Calibration Lanes at Aberdeen.
- Figure 4.8:* Model parameters from inversion of ATC Calibration Lane DNT Cart data with target (x,y,z,h,p,r) fixed at known values.
- Figure 4.9:* Target classification at ATC using Shape- and Size&Shape-based ranking metrics.
- Figure 4.10:* Response-stage ROC curves for the Aberdeen Standardized test site data. The curve for the Blind Test Grid (a) was generated by ATC. The Calibration Lane curve (b) was generated by Zonge.
- Figure 4.11:* Aberdeen Blind Test Grid target discrimination by shape (color symbols) and discrimination by shape+size (posted numbers).

LIST OF TABLES

<i>Table 2.1:</i>	Standard NanoTEM Windows
<i>Table 2.2:</i>	Loading eigenvectors for shape-based discrimination parameters.
<i>Table 3.1:</i>	Quantitative Performance Objectives for the DNT Demonstration at Aberdeen.
<i>Table 3.2:</i>	Definitions of Interpretive Rank – Aberdeen.
<i>Table 3.3:</i>	UXO Library Target Types – Aberdeen.
<i>Table 4.1:</i>	Performance Criteria for DNT System
<i>Table 4.2:</i>	Expected Performance and Performance Confirmation Methods
<i>Table 4.3:</i>	Target detectability based on DNT survey results over the Calibration Lanes at Aberdeen.
<i>Table 4.4:</i>	Table showing theoretical and observed time constants (τ) and polarizability magnitude (P_0) for wire loop targets in the Calibration Lanes at ATC.
<i>Table 4.5:</i>	Descriptions, and abbreviated model parameters for wire loop targets in Lane 2 of the Calibration Lanes at Aberdeen.
<i>Table 4.6:</i>	Loading eigenvectors for shape and size based discrimination parameters.
<i>Table 4.7:</i>	Summary of performance scores for the Blind Test Grid (after Table 6 in [43])
<i>Table 5.1:</i>	ATC Demonstration Expenses
<i>Table 5.2:</i>	Estimated job costs for a hypothetical DNT survey of a 6 ha (15 acre) site.
<i>Table 5.3:</i>	Estimated job costs for a hypothetical EM-61 MkII (bi-directional) survey of a 6 ha (15 acre) site.

A FAST 4-D TEM SYSTEM FOR UXO CHARACTERIZATION

1. INTRODUCTION

1.1 BACKGROUND

The DoD is responsible for the restoration of land that it has used in the past for training and other military operations. More than 9,000 formerly used defense sites (FUDS) have been identified. Many of these sites will require environmental restoration that, more often than not, includes the location and removal of unexploded ordnance (UXO). As a result of four rounds of base realignment and closure (BRAC), approximately 400 installations have been closed and 206 of those installations have required or will require remediation including UXO removal before the property is ready for transfer to public use. More than \$25 billion has been spent to date on environmental restoration and spending continues at rate of approximately \$2 billion annually [1-4]. Millions of acres are involved, by some estimates as many as 30-40 million acres.

UXO and other buried metallic objects can be located with magnetic detectors that sense local distortions in the geomagnetic field produced by magnetically permeable objects that become polarized in the earth's natural magnetic field. UXO can also be located using electromagnetic induction (EMI). In the EMI method, the buried metallic object produces a measureable secondary magnetic field when it is stimulated with a time-varying "primary" magnetic field produced by a transmitter antenna, usually a multi-turn loop carrying a repetitive current waveform. EMI response is affected not only by both the magnetic permeability of the target but also by its electrical conductivity. Magnetics and EMI are both effective at locating UXO. Magnetic measurements have the advantage of a better depth of investigation. On the other hand, even simple EMI methods can be used to estimate a target's size, symmetry properties, and aspect ratio [5, 6]. More sophisticated EMI instruments that are able to measure the variation of the secondary electromagnetic fields produced by eddy currents and magnetic polarization induced in the buried targets, in principle at least, are able to further parameterize the target body and thus provide additional information for target classification. New sensors and/or interpretation methods that help to reliably discriminate between UXO and other buried targets can substantially reduce the cost of UXO site remediation. Moreover, the ability to discriminate or to classify targets as UXO or Clutter and to further parameterize the targets with refined



Figure 1.1: An early deployment of NanoTEM for an environmental survey in Tucson, AZ. The system as shown uses a 20-m fixed-loop transmitter and a 1-m roving receiver loop (above the instruments).

estimates of position (particularly depth), target attitude, and target size will assure an orderly remediation of a given area.

In 1992, Zonge Engineering and Research Organization developed a broadband time-domain electromagnetic induction system, called NanoTEMTM, designed for use primarily in shallow engineering and environmental applications requiring an electromagnetic method with good lateral resolution and a relatively shallow depth of investigation (*Figure 1.1*). Since its introduction, NanoTEM has been used successfully worldwide for shallow groundwater exploration, mining exploration, and a variety of environmental applications. Over the 10-year period since its development, the instrumentation and acquisition software have been continually improved. Two major improvements to the NanoTEM system are worth noting:

1. **Multi-Channel Data Acquisition** – In 1996, Zonge demonstrated a 3-channel version of its NanoTEM system in connection with a DOE-sponsored project, the very early time-domain electromagnetic (VETEM) project at the Cold Test Pit at the Idaho National Engineering Laboratory's Radioactive Waste Management Complex (RWMC). All data for that demonstration were acquired as static measurements with 3 orthogonally oriented receiver coils (*Figure 1.2*).
2. **NT-32 Integrated NanoTEM Transmitter Assembly** – In 1998, Zonge developed a circuit board transmitter, the NT-32, that can be installed inside the GDP-32^{II} receiver. For the first time, the NanoTEM system was integrated into a single ruggedized man-portable instrument package.

These developments have facilitated the deployment of the NanoTEM system for applications calling for dynamic (continuously moving) NanoTEM surveys. The resulting EMI survey system “*Dynamic NanoTEM*” (DNT) has significant differences from other newly developed broadband EMI instruments such as the GEM-3 (Geophex), and the EM-63 (Geonics). We view the following capabilities of the DNT system as important because they differentiate it from competing systems and, in our opinion, provide “added value” in the quest to field EMI instruments that can both locate UXO and discriminate or otherwise classify targets as UXO or, alternatively, as Clutter:

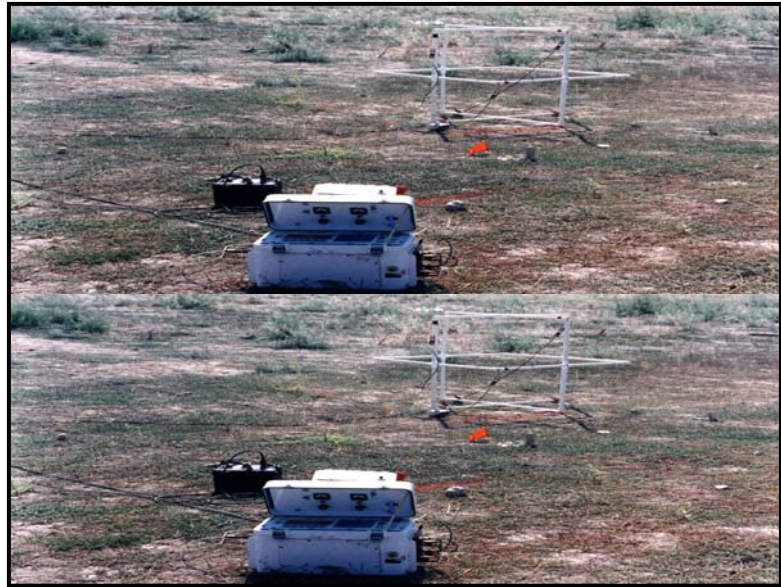


Figure 1.2: Demonstration of 4D NanoTEM at the Idaho National Engineering Laboratory in 1996. The demonstration used a 20-m fixed loop transmitter and a 3-axis roving receiver shown in background.

1. **Early Time TEM Measurements** – The DNT system measures the EM transients over a time bandwidth that is an order of magnitude earlier than its principal competitor, the EM-63.

2. **Multi-Component/Multi-Gate (4D) TEM Measurements** – Unlike both the GEM-3 and EM-63, the DNT system acquires multi-gate (31 time gates) transient measurements simultaneously for each of 3 vector components of the secondary transient magnetic fields caused by induced eddy currents and magnetic polarization in nearby targets.

1.2 OBJECTIVES OF THE DEMONSTRATION

During this project, we have conducted two demonstrations. In December, 2001 we conducted a short preliminary demonstration at NRL's Baseline Ordnance Classification Test Site at Blossom Point, MD [7]. Then, in August of 2002 we conducted a more complete demonstration of the DNT technology at the newly completed Standardized UXO Technology Demonstration Site at the Aberdeen Test Center (ATC) [8].

At Blossom Point, we had three main objectives. Firstly, the Blossom Point demonstration gave us an opportunity to demonstrate that our system was, in fact, operationally ready. Secondly, the data set we acquired provided an opportunity to compare the sensitivity of the DNT system with two other TEM systems, the EM-61 and the EM-63. A final objective of the demonstration was to show that there is "added-value" in deploying a fast multi-component EMI system such as DNT. Without question, the demonstration achieved the first two objectives. We mobilized to Blossom Point, and acquired the required data and more with only minor problems. The comparison between the DNT data set and a data set acquired by NRL with its man-portable MTADS showed that the DNT system has a sensitivity that is comparable to that of the man-portable MTADS [9]. We argue that the ability to acquire TEM data at early times significantly improves the ability to detect small, conductive, but non-permeable targets. Moreover, the horizontal TEM components provide important information about target position. They are particularly important when used in connection with physics-based analyses for target classification [10].

The demonstration that we conducted at ATC was a longer and more complete demonstration of the DNT technology. In this demonstration, there were two primary objectives. Firstly, to demonstrate our ability to efficiently survey a large area under realistic field conditions. A second objective was to demonstrate our ability to compile the data acquired at the ATC and to submit a target list for scoring in both target detection and target classification. Both objectives were achieved. The entire ATC standardized site (minus the mogul and the wooded challenge areas) was surveyed with ½-m lane spacing in 15 calendar days. We submitted our target lists, as required, within 30 days of the date that we left the survey site. We do not yet have the scores from ATC for that target list.

1.3 REGULATORY DRIVERS

There are no regulatory issues relating to the deployment of DNT technology. Clearly what drives the quest for technology that can classify as well as detect is the need to reduce the high cost of visually inspecting each detected target in order to determine whether it is UXO or Clutter. The DNT system expands on technology that is already being routinely deployed for UXO location. Zonge Engineering hopes that, by conducting these and other demonstrations, the Army Corps of Engineers and other regulators will recognize and accept the DNT system as being technically equivalent or better in all respects to competing technologies such as the EM-61.

1.4 STAKEHOLDER/END-USER ISSUES

There are no stakeholder or end-user issues to be resolved through the demonstration of this technology.

2. TECHNOLOGY DESCRIPTION

2.1 TECHNOLOGY DEVELOPMENT AND APPLICATION

The DNT system is an implementation of the transient method of electromagnetic induction (TEM). The principles of the TEM method together with a brief history of its development are presented in Nabighian [11]. The method was originally developed and perfected in the late 1950's by Newmont Exploration, Ltd for large-scale mining exploration. TEM was commercialized in the 1970's and 1980's by Australian (CSIRO), Canadian (Crone Geophysics, Geonics, and Lamontagne Geophysics), and Russian companies. Zonge Engineering adapted its microprocessor-based multi-function GDP-12 receiver to measure TEM in 1980. To our knowledge, Zonge is the only U.S. company that manufactures an instrument for TEM measurements.

As originally conceived, the TEM method is based on transmitting a DC current into a large ungrounded loop. At some point in time, the loop current is interrupted as fast as possible thereby causing a rapid change in the magnetic field generated by the transmitter. The rapidly changing magnetic field induces eddy-currents to flow in nearby conductors producing small secondary magnetic fields that are generally measured by observing induced voltages in receiver loops. The secondary magnetic fields attenuate with time, hence the application of terms such as *“transient”* and *“time-domain”* to the method. Figure 2.1 illustrates the current waveform for TEM

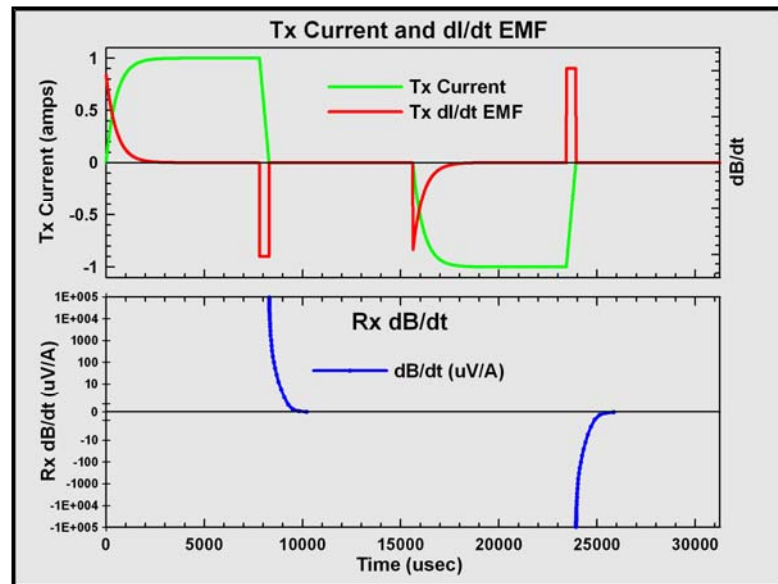


Figure 2.1: Schematic illustration of a TEM transmitter current waveform (green curve), the EMF induced in the target (red), and the resulting secondary magnetic field measured at the receiver loop (blue).

systems such as the Zonge systems that employ a bipolar waveform. The advantage of the TEM technique is that the secondary magnetic field is measured during the off-time of the transmitter, thus allowing more precise measurements of these small fields.

In its traditional application, TEM is used to search for very large conductors (ore bodies) or to acquire soundings (conductivity versus depth) of the host-rock/soil for geological purposes. For these purposes, the geometric scale of the antenna arrays can be quite large, sometimes exceeding a kilometer as a characteristic dimension. And at these geometric scales, the EM transients from the host medium alone will last for 10 ms or more. However, when TEM is applied to shallow engineering and environmental problems where the depth of interest is at most a few 10's of meters, and lateral variations over distances of a similar order are important, the size of the antenna arrays must be scaled to fit the problem. Unfortunately, the reduction of the

antenna array size introduces a very significant change in the time-scale of the transient fields induced by the smaller transmitter antenna. According to the laws of electromagnetic scaling [12], the time scale of the electromagnetic induction must be reduced by a factor equal to the square of the reduction factor applied to the transmitter loop size. This means that a reduction in the antenna array size to accommodate the need for high lateral resolution and a shallow depth of exploration is accompanied by a large change in the time-scale required to measure the resulting transients.

In 1992, Zonge Engineering introduced its NanoTEM system, a fast TEM system that matches a TEM transmitter with a very fast¹ current shut-off time and a high-speed digital data acquisition system [13]. The fast transmitter shut-off time of the Zonge NT transmitters increases the bandwidth of the transient electromagnetic signals. To measure the transient signals generated by the NanoTEM transmitter, Zonge has designed a high-speed data acquisition circuit board with an A/D that operates at a maximum sample rate of 800K samples/sec. These boards are installed in Zonge's multi-function electrical/EM receivers, initially in the GDP-16 and subsequently in the GDP-32 and GDP-32^{II}. Operating under the control of NanoTEM acquisition software, the GDP receivers sample the TEM transients over more than three-decades of time, ranging from



Figure 2.2: Photograph of the sled-mounted DNT antenna system deployed in Gambell, Alaska (St. Lawrence Island) in 2000. The targets were discarded ammunition and other metal objects dumped in a 20-ft deep lake.



Figure 2.3: A large (3m x 3m) DNT antenna array mounted on caster wheels. The antenna system includes a 3-axis receiver antenna array. It is being used to detect failures in a large concrete sewer main in Tucson, Arizona (October, 2002)

¹ Conventional TEM transmitters are able to shut the transmitter current off in times as short as 50 μ s. The Zonge NanoTEM transmitters can achieve sub-microsecond turnoff time when driving small single-turn loops. Current shut-off time depends on the natural resonance frequency of the transmitter loop, a function of both the loop inductance and its capacitance. As a general rule, fewer loop turns or smaller loops result in a faster shut-off time.

microseconds after completion of the current turn-off out to several milliseconds.

In the 10-year period since its introduction, NanoTEM has been applied throughout the world on shallow mining and groundwater exploration problems, engineering and environmental site investigations [14], and most recently for UXO location and classification. Development of acquisition software that permits the continuous acquisition of NanoTEM data began in 1999. In 2000, Zonge conducted its first production survey using DNT [15]. Conducted at Gambell (St. Lawrence Island), Alaska, that first survey employed an antenna array with a 15-ft square transmitter and a centrally located 5-ft square receiver antenna (*Figure 2.2*) to detect the presence of concentrations of small arms munitions and other metallic objects that were dumped into the bottom of a shallow (20 ft) lake. At about the same time, we began development of smaller antenna carts and improved acquisition software to meet requirements for more routine surveys. Those developments have lead us to this ESTCP demonstration. Zonge is continuing to demonstrate that the NanoTEM system can be applied to a variety of environmental and engineering problems. Our most recent application for the DNT system has been its use to assess the integrity of long stretches of municipal sewer lines for the City of Tucson, Arizona. In this application, a large antenna array (*Figure 2.3*) profiles city streets beneath which are decaying sewer lines constructed of non-metallic concrete pipe. Early time transients measurements permit the system to sense areas where the conductivity of the soil is higher due to increased moisture in the vicinity of a leak, thereby mapping areas where the sewer pipe is leaking [16].

2.2 Hardware

Figure 2.4 is a photograph of the DNT system as it has been demonstrated under this ESTCP project. *Figure 2.5* is a block diagram of the system. We list the major components of the DNT system below:

1. Antenna Cart Subsystem
2. GDP-32^{II} Transceiver Subsystem
3. Data Acquisition Software
4. Cart Attitude Subsystem
5. Navigation Subsystem

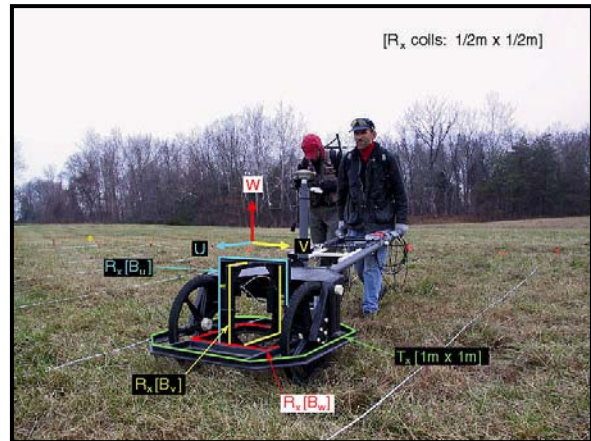


Figure 2.4: Photograph of DNT system operating at Blossom Point (December, 2001).

2.2.1 Antenna Cart Subsystem

The photograph in *Figure 2.4* shows the antenna cart. Each of the 4 loop antennas has been annotated. Similar to its competitors, the EM-61 and EM-63, the horizontal transmitter loop has nominal dimensions of 1m by 1m. There are 3 orthogonally oriented receiver loops located in the center of the transmitter loop. The loop that senses the vertical component (i.e., the w component) is in the plane of the transmitter (similar to the EM-63). Two loops oriented in the vertical planes sense, respectively, the u component (component parallel to direction of cart motion), and the v component (component transverse to the direction of cart motion). The sense of the three orthogonal components of the cart-fixed coordinate system (i.e., u, v, w) is such that it forms a right-handed system with positive w in the upward direction, positive u in the forward

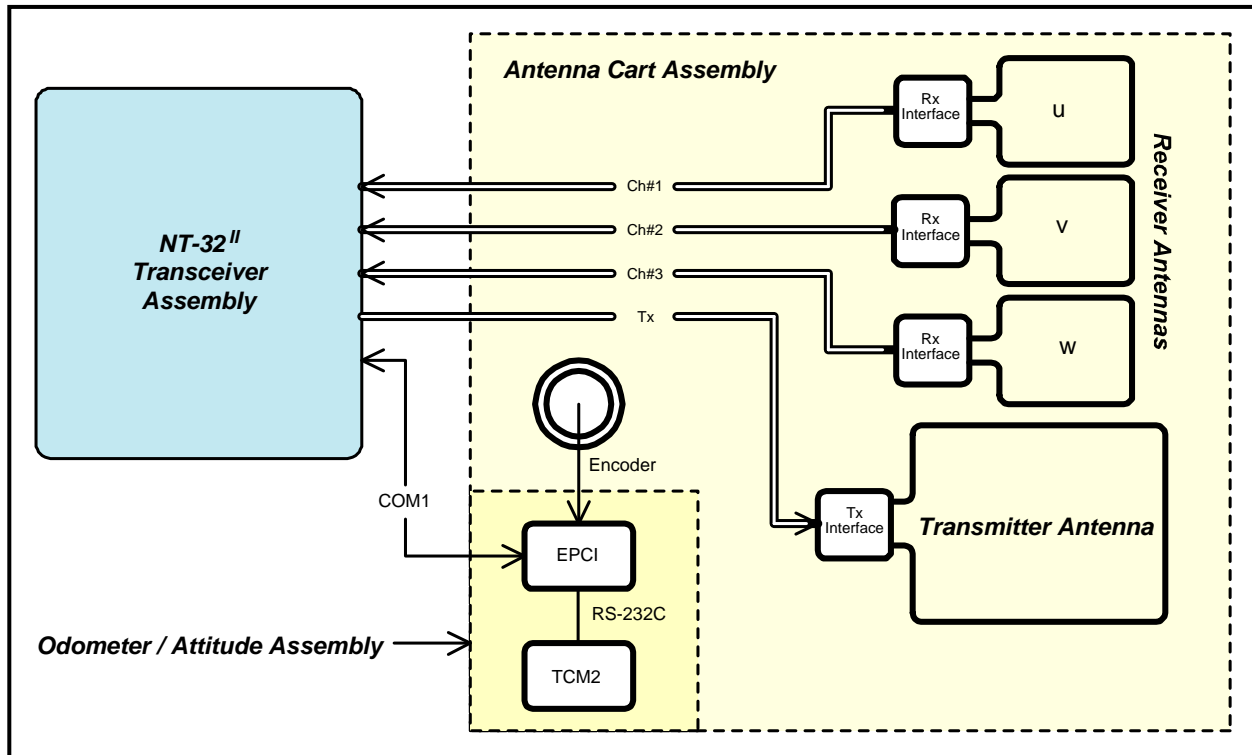


Figure 2.5: Block diagram of the DNT system

direction of cart motion when it is pushed, and positive v , by construction, directed to the left hand side of the cart. The establishment of these coordinate conventions is essential if we are to properly use the horizontal transient measurements for interpretation.

The design of the both the transmitter and receiver coils represents a series of compromises. As was demonstrated at both Blossom Point and Aberdeen, the transmitter loop contains 8 turns with an inductance of approximately $220 \mu\text{H}$. In this configuration, it has a moment of approximately $20\text{-}25 \text{ A}\cdot\text{m}^2$ depending on the transmitted current (generally around 3A). Thus the DNT transmitter moment is roughly $1/10^{\text{th}}$ of the estimated moment of the EM-61.² Electromagnetic induction, however, is driven by the time rate of change of the transmitted magnetic field (the *primary field*) so that by turning off the current ten times faster than systems such as the EM-61 and EM-63, there is little loss in signal amplitude – at least in the earlier times. This statement is confirmed by results from Blossom Point that indicate there is no significant difference between the sensitivity of the EM-61 as embodied in the man-portable MTADS system and the DNT system in the configuration that has been deployed for this demonstration [17]. Measurements of the transmitter shut-off time into the 8-turn transmitter loop show that the current is extinguished within $5\text{-}6 \mu\text{s}$.

The receiver coils each have 12 turns. Thus the effective area (turns \times area) of the receivers is nominally about 3 m^2 . The self-resonant frequency of the 12-turn receivers is on the order of $600\text{-}800 \text{ kHz}$, well above the energy bandwidth stimulated by the transmitter signal ($\sim 200 \text{ kHz}$).

² Based on measurements of the loop inductance of the standard EM-61, we estimate that it has approximately 30 turns. Published EM-61 specifications suggest that the transmitter current ranges from $6\text{-}8\text{A}$.

The antenna assembly has been designed so that its configuration can be easily changed in the field. We have the option to transmit into a 4-turn transmitter and to use a 6-turn receiver. Using a smaller number of turns more than doubles the bandwidth of the system thereby providing measurements at much earlier times. Early time response is particularly important when the system must detect small non-ferrous targets. The penalty for decreasing the number of turns, however, is a decrease in the depth of investigation for larger ferrous targets caused by the smaller

transmitter moment as well as degradation in the quality of the characteristic late time response from ferrous objects. Based on our experience thus far, we feel that the antenna configuration we have used for our demonstrations is about right. The configuration represents a compromise between the desire to boost the amplitude of the primary field to assure that large deeply buried ferrous objects (characterized by slow decay) can still be detected while at the same time preserving the ability to detect important targets whose the transients can decay down to threshold levels in a few hundred microseconds or less.

As we have indicated previously, the NanoTEM system is very sensitive to small amounts of metal. And therefore, considerable care must be taken in its design to eliminate all metal content. Our objective has been the design of a lightweight cart (< 50 lbs) that is rugged enough to withstand the mechanical abuse that necessarily occurs during normal UXO survey operations. The cart shown in *Figure 2.4* was manufactured primarily out of vacuum formed ABS plastic. The axles were machined out of G10 composite material. Non-metallic glass ball bearings were used in the wheels. All fasteners are nylon. Our experience with the demonstration cart has pointed out a number of deficiencies, all of which are mechanical. Hopefully, the mechanical problems have been designed out in the next generation DNT antenna cart, shown in *Figure 2.6*. This cart is manufactured out of strong, lightweight fiberglass tubing. The new cart weighs in at a svelte 48 lbs and promises to withstand the chronic abuse to which it will be subjected during routine UXO detection and characterization, and other types of site surveys.



Figure 2.6: Photograph showing two recent versions of cart-mounted DNT antenna arrays. The cart in the foreground is assembled from lightweight fiberglass tubing and weighs only 47 lbs. The cart in the background is manufactured from fiberglass channel beams. It weighs more than 80 lbs.

2.2.2 NT-32^{II} Transceiver Subsystem

DNT measurements are acquired using an adaptation of the 4th generation of the Zonge multi-function receivers, the GDP-32^{II}. The instrument is a standard small-case GDP-32^{II}/T. Specifications for that instrument are included in the *Appendix*. The instrument is configured with three standard NanoTEM channels together with an imbedded NanoTEM transmitter, the NT-32. Within Zonge, we have been referring to a GDP-32^{II} receiver thus configured as an NT-32^{II} and that designation will be continued throughout the remainder of this discussion.

It is beyond the scope of this report to discuss the NT-32^{II} in any detail. However, there are several standard features unique to this instrument that deserve some discussion. Firstly, the instrument is battery-powered and fully ruggedized. Its basic package design has withstood the test of time. Hundreds have been manufactured. Our customers come from around the world. Our own field crews have used them widely for many different applications. There are three features of the NT-32^{II} instrument, however, that are essential for its application to UXO detection and classification:

1. The NT-32^{II} is a multi-channel instrument (*Figure 2.7*). As configured it can simultaneously serve 3 independent acquisition channels, acquiring 16-bit digital samples for each transient channels at the rate of 800 kSamples/sec.
2. The imbedded NT-32 NanoTEM transmitter is fully computer controlled. Using the data acquisition software (discussed below), we can select both the current and the loop damping resistance for the transmitter antenna. More importantly, however, the transmitter is able to measure the actual transmitted current. This value is imbedded with the acquired data stream and permits us to normalize the transient data by the actual transmitter moment. This ability eliminates an important source of drift caused by discharge of the transmitter battery as a function of time.



Figure 2.7: Photograph of GDP-32^{II} multi-function receiver as configured for DNT data acquisition. The side access panel has been removed to expose the NT-32 circuit boards that comprise the imbedded NanoTEM transmitter.



Figure 2.8: Photograph showing setup for time synchronization of the NT-32^{II} using a SynpaqIII (Synergy Systems, San Diego) with Motorola UTM+ GPS engine.

3. Nelson [18], has recently emphasized the importance of good timing to the recovery of accurate geographic positions. An ultra-stable crystal oscillator of frequency 4.97036 MHz drives the NT-32^{II} timing circuits. Drift in the oscillator is less than 10^{-9} /24hr after warm up. The timing circuits control the transmitted waveform and drive the A/D. The timing system also includes a real time clock circuit with a timing resolution of 1/32 sec (31.3 ms).³ We electronically set this clock to UTC using time extracted from GPS signals using the setup pictured in *Figure 2.8*. With this equipment, we set the real time clock with an accuracy of a few milliseconds (including software latency). During the demonstrations, the DNT acquisition software time-stamped each measurement with a resolution of 31.3ms and an accuracy of better than 100ms.⁴

2.2.3 Data Acquisition Software

There are currently several versions of data acquisition software that can be used to acquire DNT data. We describe here the version, called ***DynanoTEM***, that we used in the demonstrations conducted under this ESTCP project. The NT-32 transmitter drives the transmitter loop with alternating current pulses at a base frequency of 32 Hz and a 50 percent duty cycle (i.e., current is on for 50% of the time). Data acquisition system is initiated by the same logic signal (named DUTY CYCLE) that shuts off the current pulse. Digital data are loaded into a 4000 word 16-bit buffer memory that is then transferred to the main memory of the NT-32^{II} processor. DynanoTEM uses 2048 of these data values minus a user-selectable number of samples that represents the sum of the transmitter turn-off time (often referred to as the “ramp” time) plus other analog and digital delays. For the present NanoTEM analog circuits, these delays include small delays in the digital circuits that actually initiate the current shutoff ($< 1\mu\text{s}$), analog delays in the gain amplifiers

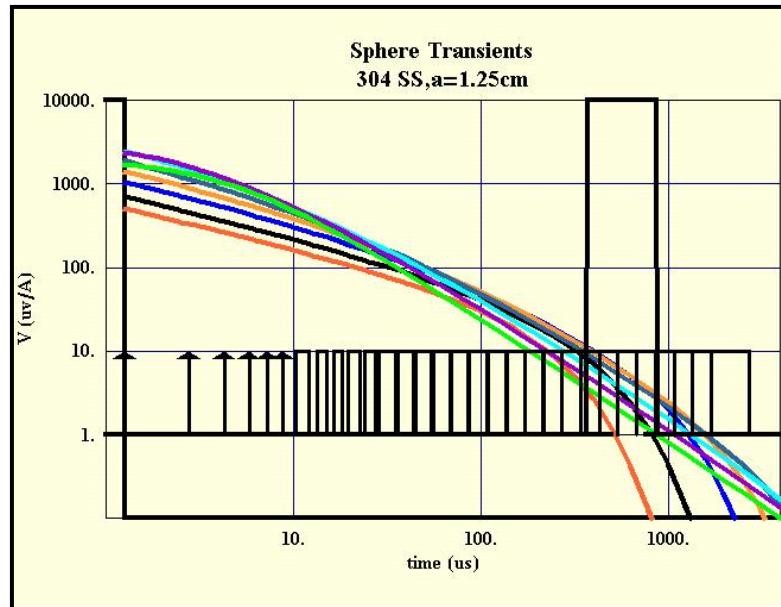


Figure 2.9: A log-log plot diagram illustrating the boundaries of the 31 Zonge Standard NanoTEM time gates. The figure shows the standard EM-61 time gate for reference. Also shown is a set of theoretical transient responses for a small conductive and permeable sphere. Magnetic permeability is the curve parameter.

³ The sub-second resolution of the real time clock circuit has been recently upgraded to 1/256 sec (3.9 ms).

⁴ Although the real time clock circuit has been standard in the Zonge receiver for more than 5 years, it was not until we started routinely testing its performance against UTC using the Motorola GPS circuit that we discovered a systematic drift ($\sim 62 \mu\text{s/hr}$) in the clock. Because of this drift, we reset the clock at approximately 1hr intervals. Subsequent to the Aberdeen demonstration, we found a problem with our digital hardware that has since been corrected. With this correction, the clock has less than 1 ms of drift over an 8-hour field day, and a resolution and accuracy of approximately 3.9 ms when read at any time.

($\sim 2 \mu\text{s}$), and the analog delay from the anti-alias filter ($\sim 1.5 \mu\text{s}$) for a total of $4.5 \mu\text{s}$. As we mentioned previously, the current turnoff time for the 8-turn loops employed for the demonstrations reported here were measured to be $6 \mu\text{s}$ for a total delay of $10.5 \mu\text{s}$. For data presented here, the total delay in the DynanoTEM system was set to 9 sample periods ($9 \times 1.2 = 11.8 \mu\text{s}$).

Each 32 Hz cycle generates a pair of transients. Transient pairs are rectified⁵ and the resulting time series is either windowed into 31 time windows (Profile Mode operation) or stored as a 2048-point rectified transient (Burst Mode operation) into a buffer. In profile mode operation, the window values are converted to voltages, corrected for amplifier gain, and stored as 4-byte floating-point numbers. Burst mode transients are stored as raw A/D binary integers and true voltages are recovered during post-acquisition data processing.⁶ Also stored in the buffer is the time-stamp for each cycle of data. The data buffer accumulates cycles for a user-selectable number of cycles, normally 32 (i.e., 1 sec), at which time the buffer is written to the NT-32^{II}'s hard drive. We have configured the software so that the resulting binary data file contains records with 32 sequentially rectified transients each of which contain 31 time gates. When multiple channels have been enabled (3 maximum) as they were for these demonstrations, a record is written for each active channel. As we have indicated, when operating in its Profile Mode DynanoTEM reduces the 2048 point rectified transients to the average value in 31 separate time windows. In other versions of

Table 2.1: Standard NanoTEM Windows

Window	32 Hz/ 1.2 us Sample Interval			
	Pts / Window	Window Center (usec)	Window Width	
			Beg	End
1	1	0.0	0.0	0.0
2	1	1.2	1.2	1.2
3	1	2.4	2.4	2.4
4	1	3.6	3.6	3.6
5	1	4.8	4.8	4.8
6	1	6.0	6.0	6.0
7	2	7.8	7.2	8.4
8	2	10.2	9.6	10.8
9	2	12.6	12.1	13.3
10	3	15.6	14.5	16.9
11	3	19.2	18.1	20.5
12	5	24.0	21.7	26.5
13	6	30.6	27.7	33.7
14	7	38.4	34.9	44.2
15	9	48.0	43.4	53.0
16	11	59.9	45.2	66.3
17	15	75.4	67.5	84.4
18	18	95.8	85.6	107.2
19	23	121.0	108.5	135.0
20	29	152.1	136.2	169.9
21	36	191.0	171.1	213.3
22	47	240.6	214.5	269.9
23	58	303.5	271.1	339.8
24	72	381.4	341.0	426.6
25	92	479.5	427.8	537.4
26	116	604.0	538.6	677.2
27	145	760.2	678.4	851.9
28	184	957.1	853.1	1074.0
29	231	1205.0	1075.0	1352.0
30	289	1517.0	1353.0	1700.0
31	369	1910.0	1701.0	2145.0

⁵ Digital rectification simply means that polarity of the negative transient is inverted and added with the positive transient. Rectification removes any DC bias from the resulting transient.

⁶ We discuss 2048 window Burst Mode acquisition here for completeness. All analyses presented in this report have been performed using data acquired by DynanoTEM when operating in its Profile Mode with 31 time windows.

NanoTEM software, the width and center points for the windows can be easily changed by modifying a window table. In the DynanoTEM program, however, these windows are hardwired to the standard Zonge NanoTEM windows based on a sample interval of $1.2 \mu\text{s}$. *Figure 2.9* shows the positions of the Zonge NanoTEM time gates relative to that of the standard EM-61 time gate. The times for the beginning, end, and center for each gate is tabulated in *Table 2.1*.

2.2.4 Cart Attitude Subsystem

For the ESTCP demonstrations, we instrumented the cart with an inexpensive compass tilt meter so that we could measure the attitude (i.e., heading, pitch, and roll) of the antenna cart. The compass / tilt meter assembly is the model TCM2 manufactured by Precision Navigation, Inc. (Santa Rosa, CA). The module contains a 3-axis magnetometer plus a 2-axis electrolytic level.

Under microprocessor control, the unit can provide measurements of magnetic heading, and platform pitch and roll angles. As indicated in the overall DNT system block diagram, the module is controlled by means of an RS-232C serial interface. We packaged the



Figure 2.10: Compass/Tiltmeter package shown mounted on the DNT antenna cart.

compass module in a small weather housing and mounted it so that it is parallel with the plane of the transmitter coil (*Figure 2.10*). The pitch and roll angles with respect to the plane of the transmitter coil are aligned using an electronic level with a tilt-angle readout and mechanically adjusting the mounting platform until the two angles correspond. The module heading is aligned by carefully pointing the cart along a baseline with a known heading and then reading the heading output from the module. The module is mechanically pivoted until it reads the correct heading to within ± 1 degree. It is reasonably easy to align the compass module to within ± 1 degree for all three attitude angles.

The TCM2 has a flexible set of measurement parameters that must be set prior to its use. The internal sampling rate of the module can be set to run as high as 40 samples per second. However, we were unable to get the module to report faster than approximately 4 samples/sec. For use with the DNT system, we set the acquisition parameters of the TCM2 for a sampling rate of 32 samples/sec (internal sample rate), enabled its internal digital smoothing filter with a 64-sample time constant (i.e., 2 sec), and 8-sample decimation. Thereafter, the compass was allowed to free-run, transmitting attitude samples at an approximate rate of 4 samples/sec. The serial data frames transmitted by the TCM2 were captured and stored independently through the serial port of an HP200LX Palmtop computer under the control of a DOS-based program (COMPASS) that appends a time-stamp from the DOS clock to each TCM2 record. The DOS clock on the HP200LX was manually set to UTC each day using the UTC time displayed on the

console of our GPS data logger. We apply a time latency correction to the compass data based on the correlation between calculated GPS headings and compass headings that occur at the end of survey lines. The compass time latency correction, as well as other latency corrections, are discussed in *Section 2.3*.

Our effort to acquire and use cart attitude data is admittedly elementary. Clearly, the digital damping settings of the TCM2 significantly attenuate high frequency noise in the attitude measurements. We believe that the 2-second time-constant applied internally was justified for this application because the maximum serial report rate that we were able to achieve from the TCM2 was 4 samples/sec. The Nyquist frequency for this sampled data stream is therefore 2 Hz. According to Shannon's Sampling Theorem, the input time series must be band limited (filtered) to remove frequencies above the Nyquist frequency in order to prevent aliasing or folding of these frequencies into the spectrum that is resolved by the decimated output time series [19]. The digital damping filter applied internally in the TCM2 mimics a single-pole analog filter function with a time-constant of 2 sec [20]. Back-of-the-envelope analysis based on the asymptotic behavior (i.e., Bode analysis) of the circuit analog for the digital filter suggests that the attitude data at the Nyquist frequency (2 Hz) have been attenuated by 28 dB. The rate of attenuation is 20 dB/decade starting at the position of the simple pole which is at $f = 0.08$ Hz. The attitude data are attenuated by approximately 3 dB at the aforementioned pole position [21]. Although the tilt-meter and compass data are anti-alias filtered and down sampled to 4 samples/second, the data stream is sufficiently detailed to catch the small cart sway due to the walking gait of the operator pushing the cart.

Our data processing program incorporates cart attitude angles (when available) into the estimation of the position of the measurement point of the antenna array.⁷ As the photographs of the cart suggest, the GPS antenna has a local vertical offset (w -coordinate) of approximately 1-m. This offset, in particular, can introduce significant errors into the position estimates when there is significant pitch or roll on the antenna platform. The pitch and roll attitude angles will introduce lateral displacements on the order of 2 cm/deg when the antenna is offset 1 m from the reference level. Therefore, when the pitch and/or roll angles of the platform exceed a few degrees, these corrections become significant.

2.2.5 GPS Navigation Subsystem

We use a Leica SR530 Real Time Kinematic (RTK) GPS system for geo-referencing of the DNT system. The Leica system consists of two dual-frequency geodetic quality receivers that are in radio communication with each other. A roving GPS antenna is mounted on the NanoTEM antenna cart. The cart operator carries the controller and monitors it for position quality (PDOP). Before we selected a mounting position, we conducted tests with the GPS antenna located at various heights above the plane of the transmitter to assure that the antenna does not measurably affect the TEM measurements.

A reference GPS antenna (base station) is located at a known or established control point in the survey area. The distance to the base station must be kept to a minimum (ideally less than a few

⁷ The cart measurement point is taken to be at the center of the transmitter and w -component receiver coils. The GPS antenna is offset from this point by a known distance. Given the local coordinates of the offset from the GPS antenna to the cart reference point, the geographic coordinates of the GPS antenna, and the cart attitude angles, we can estimate the geographic coordinates of the cart measurement point.

km) to insure good radio communication and the highest accuracy GPS solutions. The baselines can be calculated in real-time with a precision of $3 - 10 \text{ mm} \pm 1 \text{ ppm}$ using carrier phase differential GPS signals and an integer ambiguity resolution method [22, 23]. Horizontal components are generally about twice as accurate as the vertical.

2.3 DNT DATA PROCESSING

2.3.1 Overview

DNT data processing software is built around Geosoft's Oasis Montaj with the addition of specialized functions to handle TEM transients stored in array-valued channels. Processing generally follows the sequence shown in *Figure 2.11*. Each block of TEM data is merged with cart location and orientation data and saved in a Montaj database. Oasis Montaj can then be used for further data processing and plotting of results. Both profile plots and plan-map images are used for quality control. Specialized utility programs may be driven from within Montaj for data filtering, target picking and modeling.

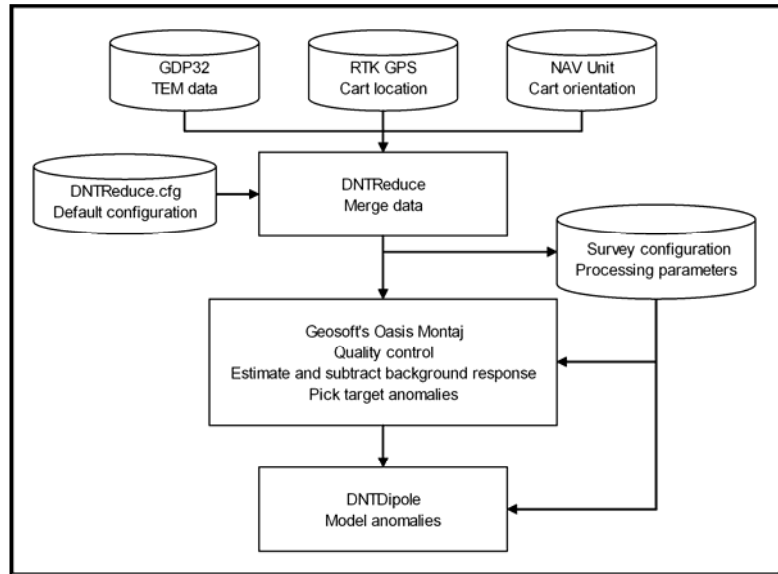


Figure 2.11: Block diagram showing major data elements and processing modules used in DNT data processing.

Metadata specifying hardware configuration and data processing parameters are saved in text files accessible by all DNT software. Configuration files are in an Oasis Montaj parameter-block format that can be reviewed and edited with a text editor or with interactive DNT software utilities. DNT programs read default parameter values from *CFG* files and write updated values to provide an archival record of survey configuration and data processing parameters.

2.3.2 Merge Data

DNT hardware collects three separate data streams, each recorded by a different device. Three-component TEM data are acquired by the GDP-32^{II} at a sample rate of 32 Hz, cart locations are recorded by a RTK GPS sampling at 5 Hz, and a navigation unit records cart orientations at 4 Hz. After files are downloaded from survey hardware to a PC, the three data streams are merged into a single data set with the utility program *DNTReduce*, which uses time-of-day to interpolate location and orientation data for each TEM transient. Differences in time synchronization (device latency) can be corrected by adding time offsets during interpolation and merging. *DNTReduce* is usually driven from within Oasis Montaj, but it can also be used as a stand-alone program that writes merged data to a *CSV* file.

Once data are merged, **DNTReduce** provides an option for reducing noise levels and file size with tapered stacking and decimation. The DNT system records 32 transients per second, equivalent to a sample interval of 3 cm along line at a typical walking speed of 1 m/sec. Tapered stacking and decimation by a factor of four reduces noise levels by a factor of two or better, but increases the along-line sample interval roughly from 3 to 12 cm. A 12 cm sample interval is sufficient to adequately resolve anomaly shapes for near surface UXO, so decimation by four is a good compromise between noise reduction and sample density for walking-speed cart surveys. Static follow-up measurements generate long bursts of data collected without movement. For static data, a large stacking and decimation factor can be used to condense a data burst into a single transient for each receiver-loop component.

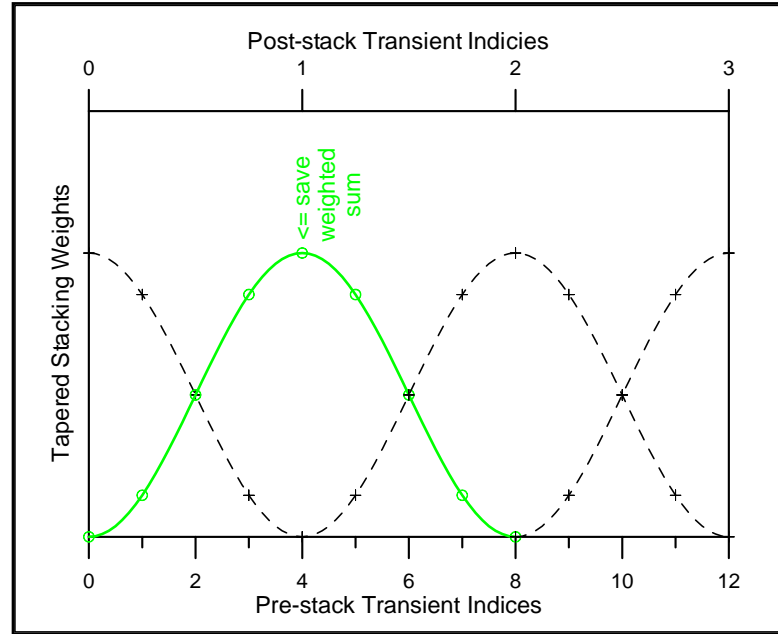


Figure 2.12: Transient data are smoothed along line with a low-pass filter before decimation by an integer factor, in this case decimation by four.

If data are to be decimated, values for each component and transient delay time are first averaged using \cos^2 weights (Figure 2.12). The averaging window is sized to fit the decimation interval with 50 percent overlap, and \cos^2 weighting gives each data value the same weight no matter where it appears in the input data stream.

An alternative view of stacking is to view it as a low-pass filter. In the context of a filter, it is useful to examine the frequency response of the stacking window. Figure 2.13 shows the frequency-domain response of stacking windows for decimation by a factor of four. The response of a \cos^2 window is shown as a solid green line and, for comparison, the response of a four-point rectangular stack is plotted as a dashed black line.

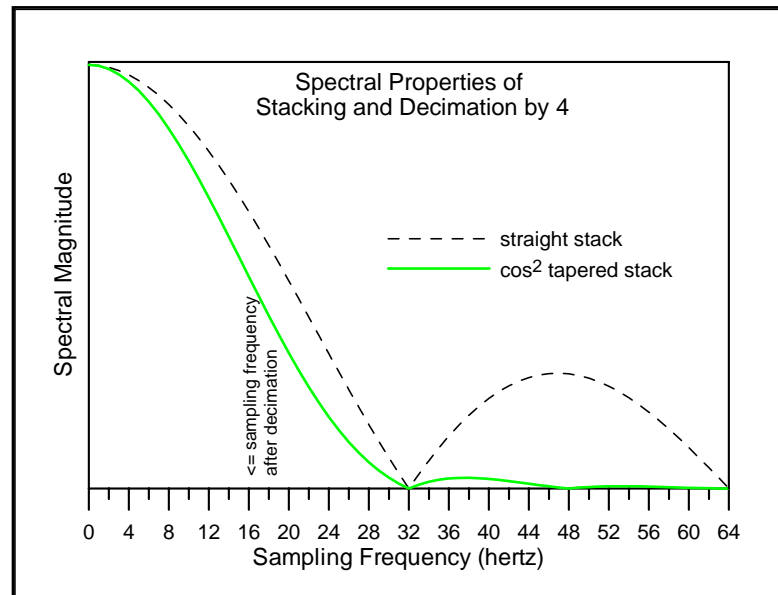


Figure 2.13: The frequency-domain spectra of a \cos^2 window for decimation by four (solid green line) and for a four-point rectangular window (dashed black line).

Gaussian noise by about a factor of two. A \cos^2 window does a somewhat better job of suppressing uncorrelated noise before decimation, reducing uncorrelated noise by a factor of about 2.12. The advantage of using tapered stacking becomes more significant in the presence of high-frequency synchronous noise, where the more rapid high frequency fall-off of the tapered-window filter is advantageous.

2.3.3 Quality Control

Latency and receiver calibration quality control tests are performed at the beginning and end of each data acquisition block. A three-inch diameter steel calibration ball is placed on the ground at a test-spot location chosen for convenient proximity to the survey area and low geologic and cultural noise levels. Two walking-speed traverses are then made in opposite directions over the calibrate ball to check time synchronization and GPS accuracy. To check receiver response, the system is then brought to a halt over the calibration ball and data are recorded for 30 seconds. These quality control data are differentiated from production data by incrementing the line number. *Figure 2.14* shows a typical “Calibration Ball Latency Test”. The top profile represents dBw/dt (12-21 Composite time gate) as a function of time (fiducial number). The two peaks shown in the profile are generated by two passes over the calibration target in opposite directions. The last part of the profile is produced by backing up the antenna cart until it is centered over the calibration target where we record for about 30 seconds while the cart is motionless. With proper acquisition and GPS time synchronization, when we replot the TEM response as a function of distance along line, the two anomalies should overlay as shown with the bottom profile of *Figure 2.14*.

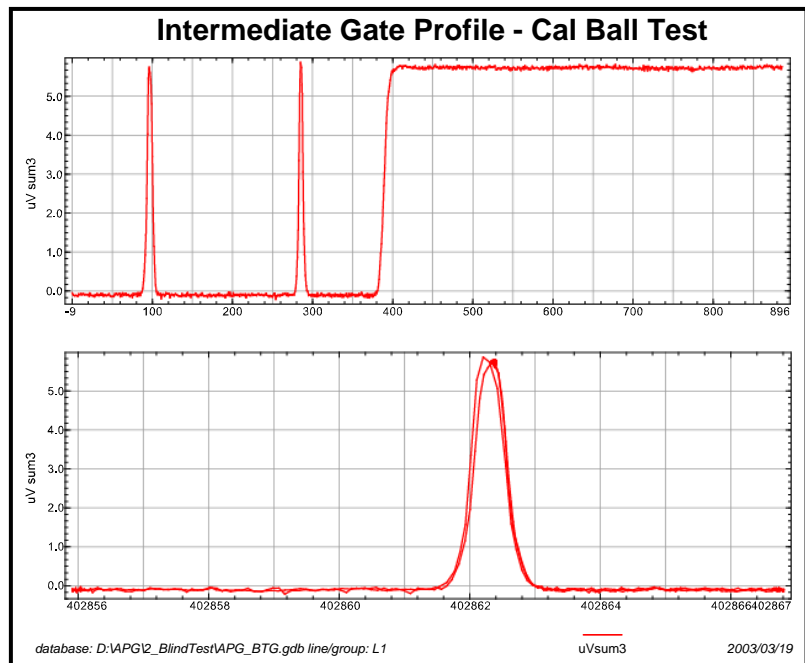


Figure 2.14: Calibration ball latency test profiles. In the top profiles, we have plotted the test data with respect to time (fiducial number). In the bottom profile, the data are plotted as a function of UTM Easting.

After data for each acquisition block are merged and imported into Oasis Montaj, quality control and production data are segregated by splitting the data into lines. Synchronization or GPS location error can be checked by plotting a profile of latency test data and looking for offsets between anomaly peaks. A utility program, *DNTLatency*, facilitates the test by plotting data profiles and automatically adjusting time offsets to minimize anomaly peak separation. Time synchronization errors are corrected by re-merging data streams with updated time-offset values. The receiver’s response amplitude was checked by building a table of calibration test values and looking for deviations of 5% or greater.

We review survey area coverage by making station location plan maps with Oasis Montaj and looking for excessive line separation. The DNT system's high sampling density along line generates clear map-view traces of line locations when small • symbols are plotted at every measurement location.

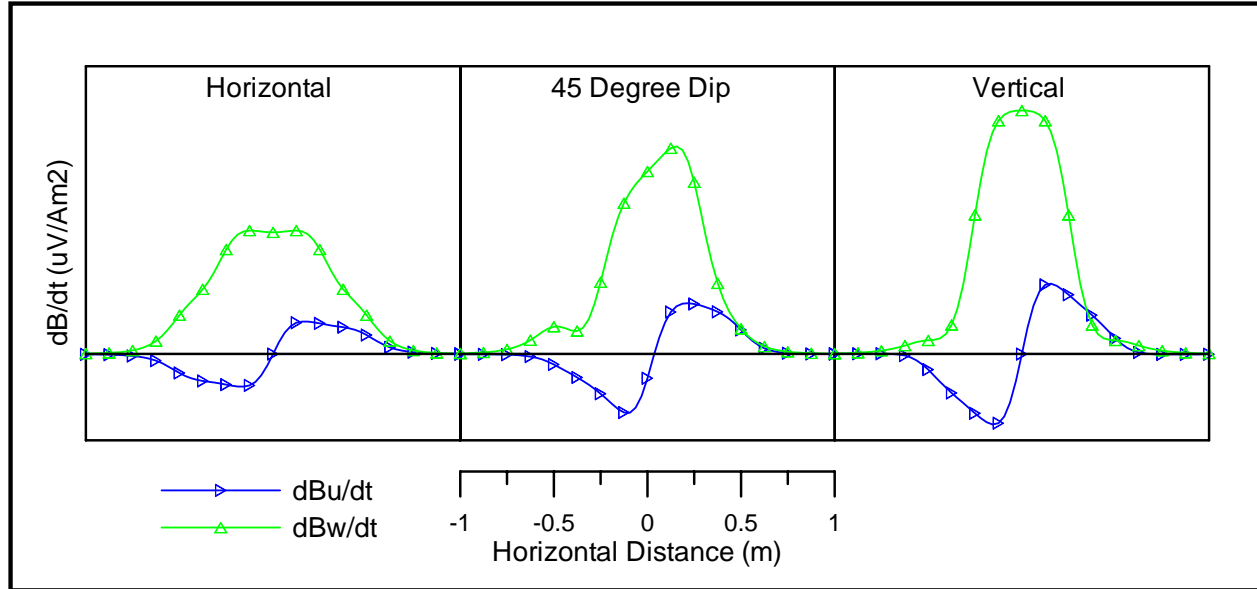


Figure 2.15: Profiles illustrating the change in the behavior of vertical field response (green) and along track horizontal response (blue) as a function of target attitude.

Oasis Montaj's profile plotting capabilities provide a natural way to review data plausibility. Single point outliers can be rejected as noise since anomalies over UXO have characteristic shapes sampled with a number of measurement points (*Figure 2.15*). Anomaly widths are proportional to receiver loop clearance plus UXO depth. UXO generate positive peaks in the vertical TEM component, dBw/dt. Distinct crossover patterns are generated in the along-line, horizontal component, dBu/dt, with the positive side-lobe in the direction of cart movement. dBw/dt and dBu/dt anomaly sign serves as a check on data polarity.

Further checks on data quality can be made by reviewing plan-map images. The **DNTRotate.gx** is a utility for rotating cart-oriented (u, v, w) TEM components to geographic (x, y, z). To get a scalar channel value suitable for plan-map image display, **DNTCompositeWindow.gx** is useful for summing transient data over a time interval to get a scalar value. Plan map images of horizontal component dBx/dt and dBy/dt are a check on cart location, orientation and u, v TEM component polarity. dBx/dt and dBy/dt UXO anomalies have cross-over pattern with positive peak on the positive coordinate side of the UXO, i.e. dBx/dt peaks should be positive on the grid east side of UXO and dBy/dt peaks should be positive on the grid north side of UXO.

2.3.4 Background Response

Utility **DNTBkgFilter.gx** may be used to estimate and subtract background values from array-valued transient data. “Background” is defined as all response components with slow spatial variation, in contrast to the narrow anomalies generated by UXO.

Estimation of background values can be improved by excluding clearly anomalous data from the estimation procedure. **DNTBkgFilter.gx** accomplishes that by including an optional background flag channel as input and by skipping all data flagged as anomalous. Highly anomalous data segments are flagged by making a preliminary list of target anomaly picks and then clearing background flags in a circular patch around each pick. **DNTBkgFilter** then proceeds with background estimation without using data flagged as anomalous.

Background values are estimated for each receiver loop component, line and transient delay time by a non-linear, low-pass profile filter. Data are first interpolated onto an equal-spaced sample interval along line with a median filter having a constant, user-specifiable width. Any gaps due

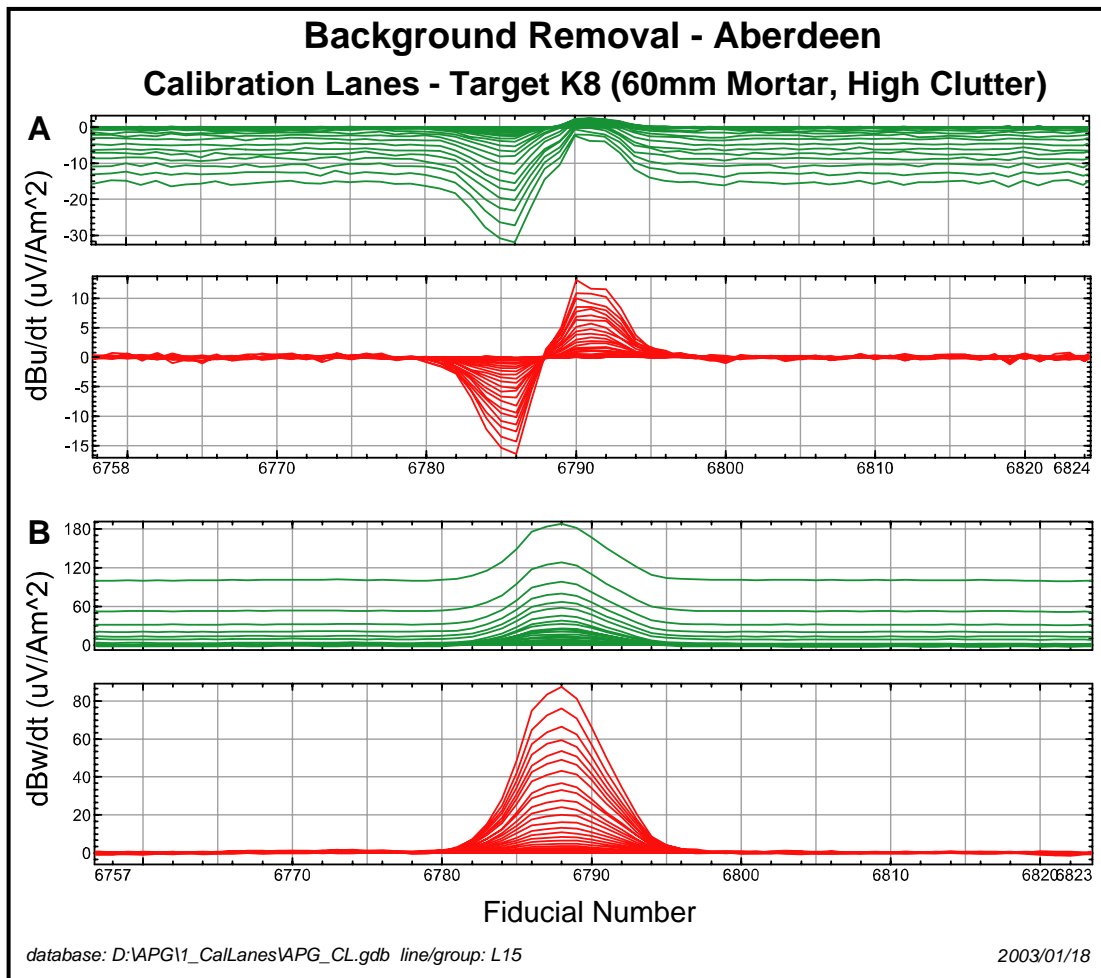


Figure 2.16: Illustration of background removal from raw TEM data (vertical field) at Aberdeen. The top pair of profiles show dBu/dt , and the bottom pair show dBw/dt data. The top set of profiles for each pair represent the 31 gates of the DNT data. The bottom profiles for each pair are the 31 residual profiles after background removal.

to long segments of anomalous data are filled in with smooth interpolation. Next, a Gaussian moving average is passed along the profile of equal-spaced samples to smooth the background response estimate. The equal-spaced estimates of background response are interpolated back to actual measurement locations. Both background and measured-minus-background residual values are saved in Oasis Montaj array channels. We illustrate the results of this background removal (“leveling”) process in *Figure 2.16(A,B)*. The figures show 31 profiles (one for each DNT time gate) for the raw transients (green traces) and the resulting residual traces (red traces).

2.3.5 Target Picking

UXO generate positive-peak anomalies in the vertical TEM component. Hence, scalar values from a composite-window of dBw/dt data provide a natural response parameter to use for picking target anomalies. Targets can be picked by identifying peaks in the response-parameter from either profiles or plan-map data. Picking target anomalies from profile data is useful when data are collected in long meanders. Picking targets from an image grid is appropriate when data are collected along closely spaced parallel lines. When comparing histograms and receiver operating characteristic (ROC) curves generated from targets picked with the two methods, it is important to recognize that the process of interpolation of line-oriented profile data to a regular lattice of grid points is equivalent to a low-pass filter. The grid-spacing and the gridding algorithm act as filter parameters and their choice significantly affects the amount of smoothing in the output data grid.

If data are available from an area with test objects at known locations, an optimal target-picking threshold can be selected by consideration of a ROC curve.

2.3.6 Physics-Based Target Modeling

Patches of TEM data near target anomalies are parameterized with the widely used anisotropic dipole model [24]. Three orthogonal magnetic dipoles are used to represent target polarizability along three axes. Spatial variation of receiver loop dB/dt across the data patch is projected onto three, generally tilted target axes, compressing data from many measurement positions and multiple loop orientations into three polarizability values for each transient delay time. Time-dependent target properties are parameterized by fitting a transient-shape model to the polarizability transient for each of the three target axes.

Targets can be characterized by these physics-based model parameters [5, 6, 25]. Transient shape is influenced by target size, shape, conductivity, and magnetic permeability. Polarizability magnitude is proportional to target volume. Ratios of target-axis polarizability are indicative of target symmetry and aspect ratio.

Point Anisotropic Dipole Model

An anisotropic dipole model is suitable for predicting the response of compact, conductive objects in a resistive background. Referring to *Figure 2.17*, inductive coupling between transmitter loop and target is represented by $\bar{H}_{Tx}(\vec{r})$, the free-space magnetic field at the target generated by a unit current in the transmitter loop. As the transmitter current pulse is shut off it illuminates the target with a dB/dt impulse that induces a dipole moment with a derivative with

respect to time of $\bar{M}'(t, \bar{r}') = \bar{P}'(t) \cdot \bar{H}_{Tx}(\bar{r}') \cdot \delta(t)$.⁸ The target's dipole moment, $\bar{M}'(t, \bar{r}')$, typically has a different orientation than the transmitter's magnetic field due to the target's elongation and tilt. Inductive coupling between the polarized target and each receiver loop is represented by $\bar{H}_{Rx}(\bar{r})$. $\bar{H}_{Tx}(\bar{r}')$ and $\bar{H}_{Rx}(\bar{r})$ are non-linear functions dependent upon transmitter and receiver loop size, orientation and location relative to the target.

$$\frac{dB(\bar{r}, t, \bar{r}')}{dt} = \mu_0 \cdot \bar{H}_{Rx}(\bar{r}) \cdot \left(\bar{P}'(t) \cdot \bar{H}_{Tx}(\bar{r}') * \frac{dI(t)}{dt} \right)$$

where, $\frac{dI(t)}{dt} = I\delta(t)$ when the current waveform is a step change in current(2.1)

and * signifies convolution

The target's orientation and time-dependent behavior are described by the tensor polarizability, $\bar{P}(t)$. For TEM modeling, convenient units for $\bar{P}(t)$ are $\text{cm}^3/\mu\text{sec} = \text{m}^3/\text{sec}$. $\bar{P}(t)$, the target polarizability, is a symmetric tensor that can be diagonalized by a rotation from geographic (x, y, z) to target axes (u, v, w) coordinates. An unrotated polarizability tensor can be parameterized by six parameters ($p_{xx}, p_{yx} = p_{xy}, p_{yy}, p_{zx} = p_{xz}, p_{zy} = p_{yz}, p_{zz}$). When rotated, polarizability is a function of $(\theta, \phi, \varphi, p_u, p_v, p_w)$ where θ, ϕ , and φ are Euler rotation angles and p_u, p_v , and p_w are polarizability values along target axes. An anisotropic dipole model is suitable for predicting the response of compact, conductive objects in a resistive background.

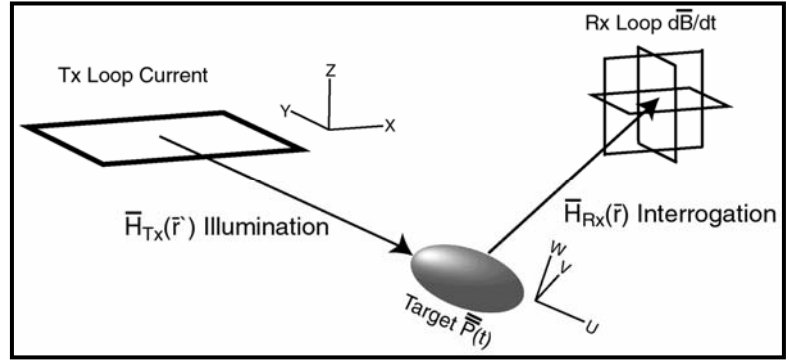


Figure 2.17: Schematic of anisotropic point-dipole model.

$$\bar{P}(t) = \begin{bmatrix} p_{xx}(t) & p_{xy}(t) & p_{xz}(t) \\ p_{yx}(t) & p_{yy}(t) & p_{yz}(t) \\ p_{zx}(t) & p_{zy}(t) & p_{zz}(t) \end{bmatrix} = \bar{R}(\theta, \phi, \varphi)^t \cdot \begin{bmatrix} p_u(t) & 0 & 0 \\ 0 & p_v(t) & 0 \\ 0 & 0 & p_w(t) \end{bmatrix} \cdot \bar{R}(\theta, \phi, \varphi) \quad \text{..... (2.2)}$$

TEM dB/dt transient data can be inverted to recover target properties by rearranging the dipole model to express dB/dt as a function of target (x, y, z) and polarizability. Since the target's orientation and time-dependant properties are contained in the polarizability tensor, a preliminary

⁸ For brevity, we are using the notation to signify implicit differentiation with respect to time (e.g. $\bar{P}'(t) = \frac{d\bar{P}(t)}{dt}$)

inversion to recover target position and orientation can be separated from inversion to recover a description of target polarizability time variance.

For preliminary inversion to recover target position and orientation, each TEM transient can be collapsed to a single scalar value by using a weighted sum,

$$dobs_j = \sum_i \frac{dB(t_i, r_j)}{dt} \cdot wt_i \cdot wr_j$$

$$\text{where } wt_i = 1 / \sqrt{\left(\epsilon r_j^2 + \frac{dB(t_i, r_j)}{dt} \right)} \quad \dots\dots\dots (2.3)$$

and $wr_j = 1/\epsilon r_j = 1/\text{transient noise levels}$

Data for each transient delay time are weighted by wt_i , a measure of signal strength, so that so that early-time values with amplitudes near 10^5 uV/Am² do not completely dominate late time data with amplitudes below 1 uV/Am². wr_j weighting accounts for noise-level differences between transients.

Parameterization of Principal Polarization Transients

Once a satisfactory target location (x,y,z) is estimated, a singular value decomposition of $\overline{\overline{P(t)}}$ for a composite time window value yields the coordinate rotation necessary to diagonalize the polarizability tensor. With a target location and orientation in hand, the dipole model can be used to project receiver dB/dt onto target axes polarizability for each transient delay time. The projection generates observed polarizability data ($p_u(t), p_v(t), p_w(t)$), which compactly describe the target's time dependent behavior.

Polarizability transients for each target axis can be parameterized in more than one way. We used numeric integration of $p(t_i)$ (in cm³/μsec) to get a p_0 (in cm³) for a measure of overall polarizability magnitude. Following a suggestion by Smith and Lee [26], we also used numerical integration of $t \cdot p(t_i)$ from 0 to $25 \cdot 10^3$ μsec to get a polarizability first-moment pI (in msec * cm³) for a weighted measure of overall polarizability transient magnitude emphasizing the late-time response.

To parameterize information about polarizability transient shape, we used Pasion and Oldenburg's [25] model

$$p(t) = k \cdot e^{-c \cdot 10^{-3} \cdot t} (a + t)^{-b} \quad \dots\dots\dots (2.4)$$

where, k = polarizability magnitude (cm³/μs ^{$b+1$})

a = early-time extent (μs)

b = mid-time power-law decay exponent (dimensionless)

c = late-time exponential decay rate constant (1/ms)

The Pasion model matches the early-time flattening, mid-time power-law decay and late-time exponential behavior characteristic of most polarizability transients.

2.3.7 Implications for UXO Classification

The modeling software that we describe here extends the work described in Barrow et. al. [5] so that the dipole model considers the 4 dimensions (i.e., time and 3 vector components) of the data that we acquire. The two horizontal vector components provide additional independent data at each sample point and thereby eliminate the need to conduct surveys at either unrealistically close survey line spacings or, alternatively, to survey an area twice in orthogonal directions. We note that Nelson states that effective analysis of MTADS EMMS data require two surveys in orthogonal directions[27]. The ability to look at how the anisotropic polarizability changes in time has important implications for target classification.

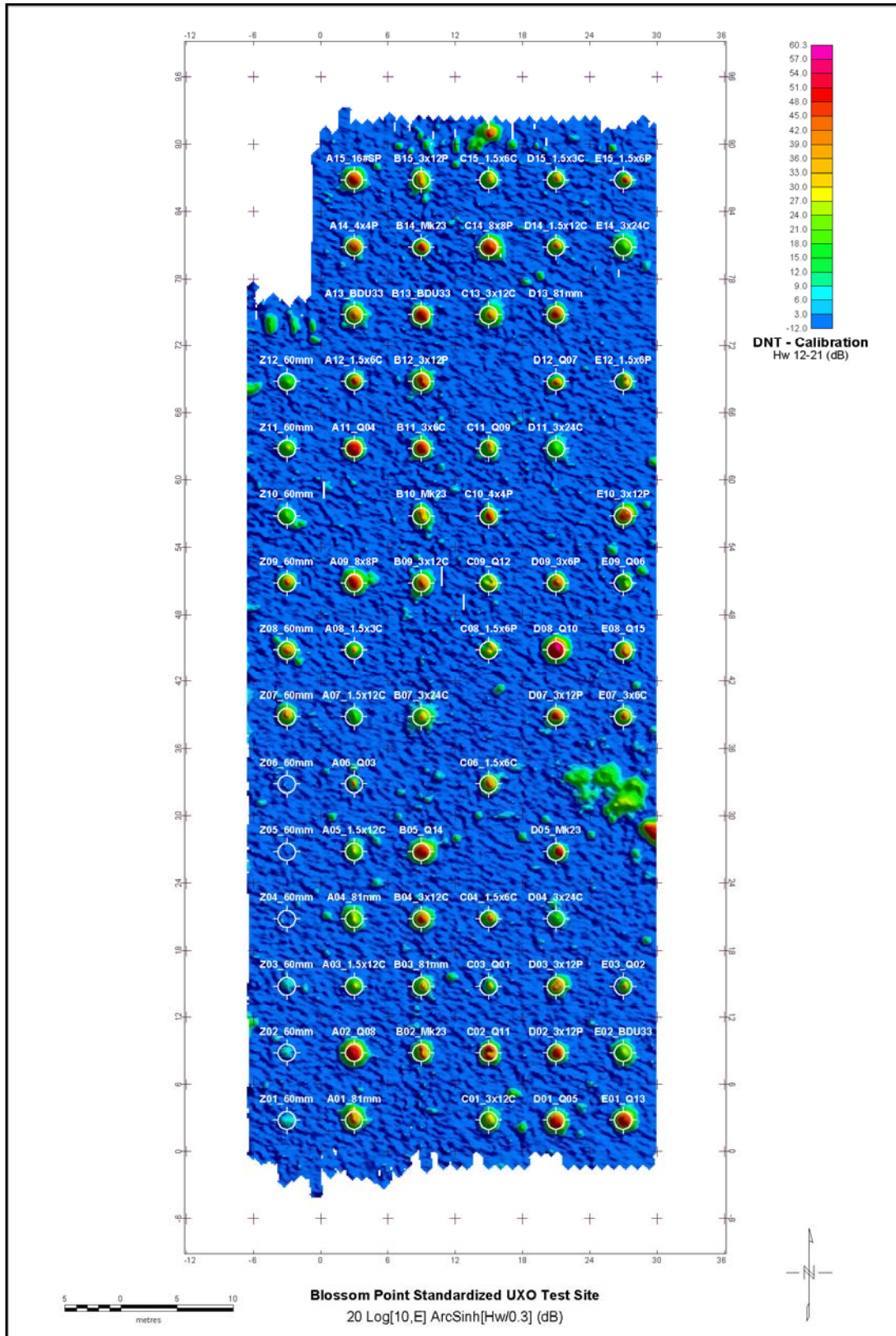


Figure 2.18: Map of companded vertical dBw/dt field for an intermediate composite time gate over Blossom Point.

Model Parameter Summary Plots

In subsequent figures, we use data acquired from our Blossom Point demonstration to illustrate the efficacy of the target parameterization software that we have developed. *Figure 2.18* is a map of the vertical field component of the DNT survey. These data were acquired using lines oriented in the N-S direction with ½-m offsets. We have posted on the map both the target cell location and the target identity. Note that values imaged in this map have been compressed onto a near logarithmic scale in order to better show the dynamic range encompassed by the target set. Anomalies on the map cover a range of about 60 dB above the noise level at Blossom Point.

Figure 2.19 is a target polarization plot generated from the DNT data set for which *Figure 2.18* represents only a single vector component (dBw/dt) and a single composite time gate (gates 12-21 or, from *Table 2.1*, 22-213 μ s). The target, “A15_16#SP” is a 16 lb shotput located in cell A-15 (upper left hand side of *Figure 2.18*). The parameterization, which was constrained to allow the solution for spheroidal model polarization, shows nearly equal polarizability transients over the complete range of time delays measured by the DNT system ($dP_u/dt \approx dP_v/dt = dP_w/dt$). In a spheroidal model, when the longitudinal polarizability is equal to the transverse polarizability, the target is a sphere.

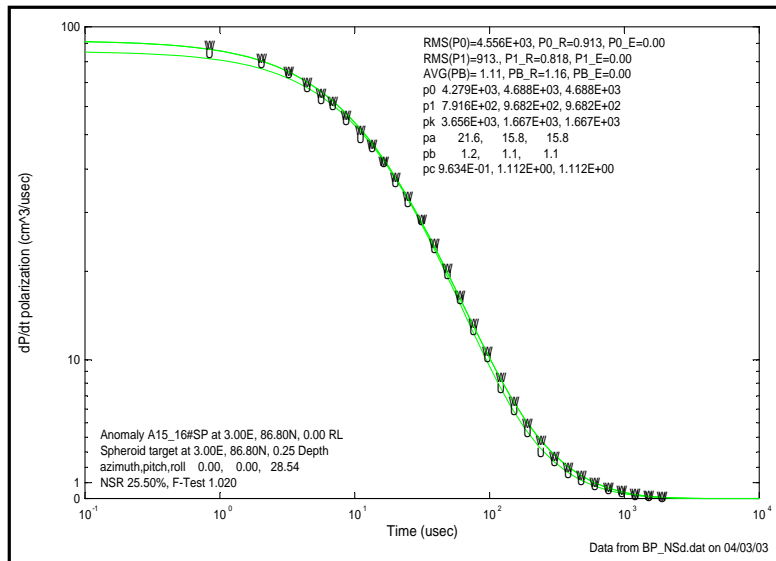


Figure 2.19: Polarizability transients for a 16 lb shotput show the symmetry expected for a spherical object, $dP_u/dt = dP_v/dt = dP_w/dt$. Pasion model b values > 0.8 indicate a permeable object.

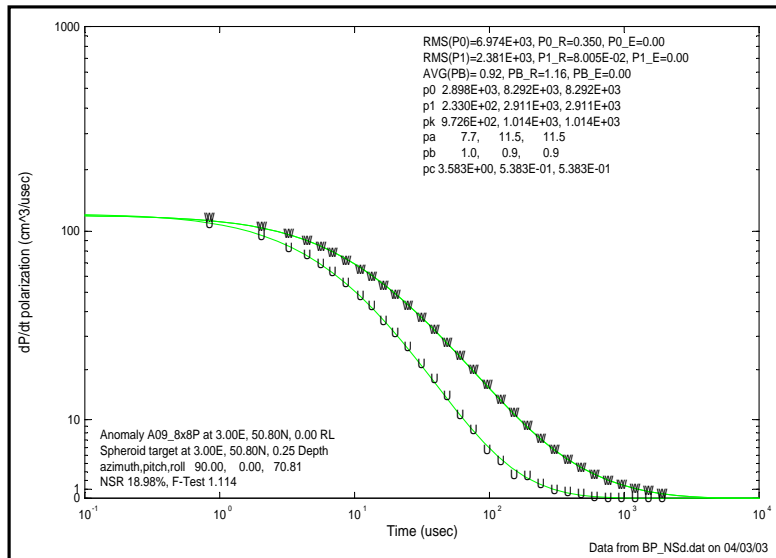


Figure 2.20: Polarizability transients for a permeable plate indicate the plate’s disk-like symmetry with $dP_u/dt < dP_v/dt = dP_w/dt$.

The Pasion **b** parameters (both values > 0.8) are an indication of high permeability. And finally, the average polarizability magnitude (RMS(P0)=4556 cm³) is an indicator of overall size or volume of the object. In the case of a sphere, we know that [28]

$$P0 = 6\pi a^3 \frac{k}{k+2}; \text{ where } a = \text{sphere's radius and } k = \text{relative mag permeability (2.5)}$$

Thus the analysis of the DNT data over target A-15 suggests a magnetically permeable sphere having a radius of approximately 7 cm or 2.8 in, not a bad estimate for the dimension of this particular target.

Figure 2.20 is a target polarization plot generated from the analysis of target “A08_8x8P”, an 8” x 8” x 1/4” steel plate located in cell A-8. The spheroidal model indicates good symmetry with transverse polarizability that is greater than longitudinal polarizability (dPu/dt<(dPv/dt=dPw/dt)). This behavior suggests disk-like symmetry. The Pasion **b** parameters are again > 0.8, suggesting a permeable object.

And lastly, Figure 2.21 is the polarization plot from the analysis of target “B02_Mk23”, a Mk23 practice bomb located in cell B-2. This parameterization shows the largest polarization transient (dPu/dt) together with two smaller and nearly equal minor (dPv/dt=dPw/dt)).

The foregoing polarizability plots suggest how this software can be used for target classification. They also illustrate that DNT data acquired along a single set of lines spaced at 1/2-m intervals is sufficient to correctly estimate shape and other properties of buried targets. We are working towards a better understanding of the implications of the various target parameters that we are now routinely computing by examining whether they separate target groups when plotted for an ensemble of different targets. The data acquired at Blossom Point currently represents our best opportunity for study and helps to illustrate our method of parameterization. In Figure 2.22, we show a set of 8 scatter plots for the set of 73 targets identified in Figure 2.18. To help show the separation of various target classes in the plots, we have divided the targets into four groups:

1. Rod-Like Targets
2. Disk-Like Targets
3. Elongated Plates
4. Clutter

The 8 plots correspond to 8 sets of model parameters from polarizability transient amplitude and shape. The top row of plot panels depicts model parameters related to target size, shape, symmetry and depth. The bottom row of plot panels shows all of the

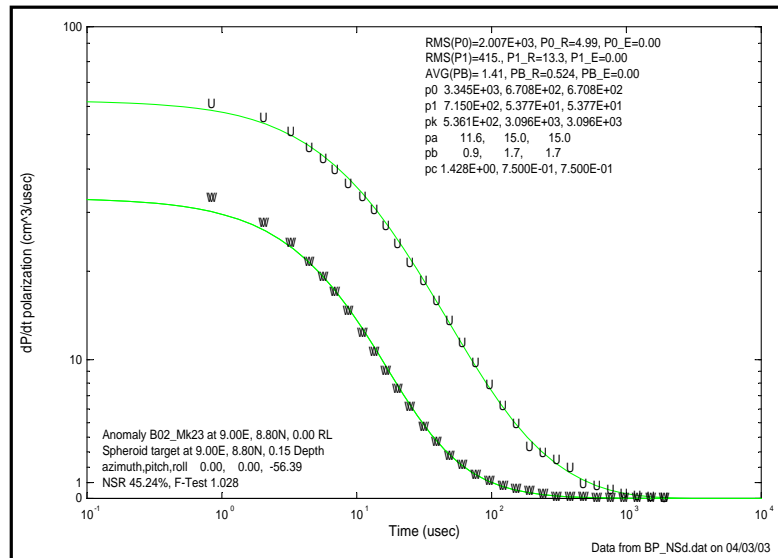


Figure 2.21: Polarizability transients for a Mk23 indicate a ferrous cylindrical object with rod-like symmetry. Pasion model **b** is greater than 0.8, indicating a permeable object and longitudinal polarizability dPu/dt is greater than two nearly equal transverse polarizability responses, dPv/dt = dPw/dt.

Pasion model parameters for longitudinal and transverse polarizability, which are equivalent to a compact parameterization of polarizability transient shape. Individual combinations of model parameters are related to target attributes useful for categorization.

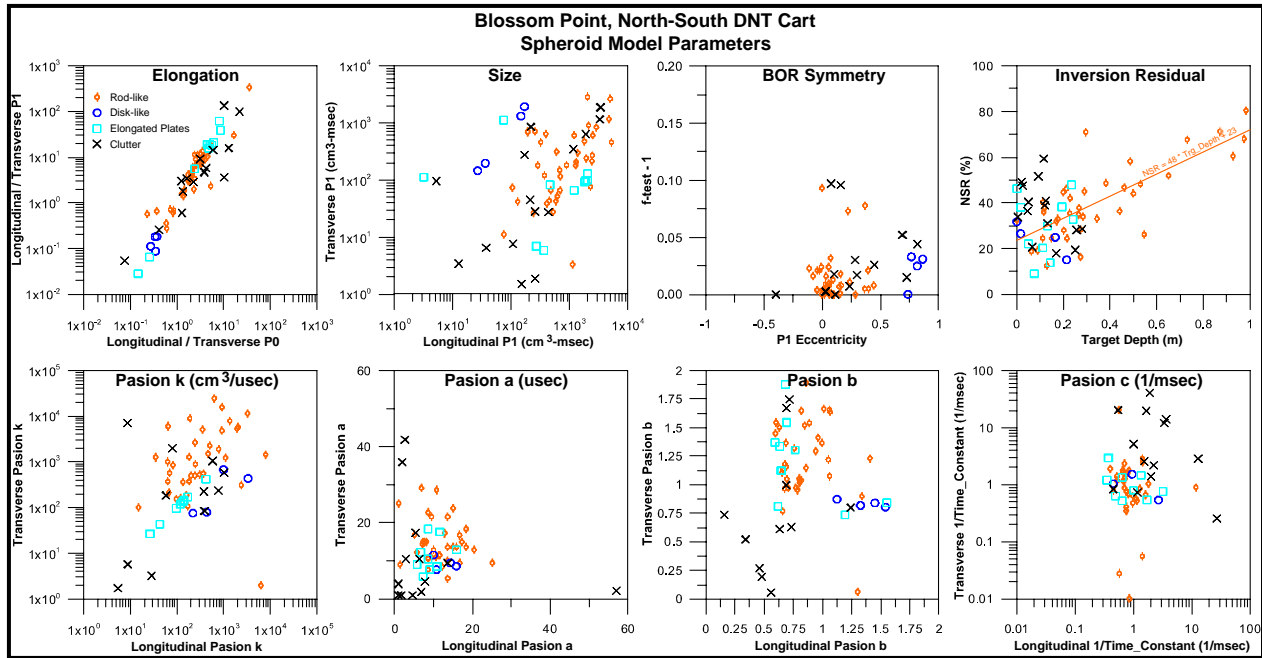


Figure 2.22: Model parameters from inversion of Blossom Point North-South DNT Cart data with target (x,y,z,h,p,r) fixed at known values.

Longitudinal/transverse polarizability, $P0$, and polarizability first moment, $P1$ are shown in the upper-left plot panel labeled **Elongation**. Polarizability ratios are good indicators of target shape, rod-like ferrous targets will have longitudinal/transverse polarizabilities greater than 1, while disk-like objects will have polarizability ratios less than 1. The clustering of orange symbols around a $P0_L/P0_T$ ratio of 4 and a $P1_L/P1_T$ ratio of 10 supports this expectation. The blue circles in Figure 2.22 indicate the response of disk-like ferrous objects, in this case square steel plates. As expected, the response of disk-like targets generates polarizability ratios less than 1. The relationship of polarizability ratio to shape is reversed for non-permeable objects, with rods having ratios less than 1 and non-permeable disks having polarizability ratios greater than 1. Although both $P0$ and $P1$ ratios are robust indicators of target elongation, UXO polarization anisotropy generally increases at late time, so the heavier late-time weighting used to calculate $P1$ emphasizes shape anisotropy relative to $P0$ ratios. Most UXO are permeable and somewhat elongated, so polarizability ratios slightly greater than 1 are a good parameter for selecting for UXO-like shape.

The upper-row panel labeled **Size** in Figure 2.22, shows longitudinal versus transverse $P1$, which is related to target size and conductivity. If the expected UXO types fall into a limited size range, then $P0$ and $P1$ are a good basis for categorization based on target size. Polarizability transients generated by small shrapnel fragments decay more quickly than transients due to intact UXO, so their corresponding $P0$ and $P1$ values are also smaller, even when generated by a large patch of small fragments. Categorization by size is less useful when a large size range of UXO is expected, forcing more reliance on shape and symmetry parameters.

Figure 2.22 includes a panel labeled **BOR Symmetry** (Body Of Revolution) showing two parameters measuring the target's cylindrical symmetry. The f-test values are ratios of spheroidal/ellipsoidal inversion residual chi-squared. If the target has cylindrical symmetry and SNR in observed-data are sufficiently high (15 dB or better), then the spheroidal model will fit observed data as well as the ellipsoidal model and the spheroidal/ ellipsoidal f-test will be near 1. F-test – 1 is a sensitive test of the target's apparent cylindrical symmetry. Another measure of target symmetry is eccentricity, a parameterization described by Barrow, and others [5] and plotted along the x-axis of Figure 2.22's BOR Symmetry panel.

$$P0E = \frac{P0_2 - P0_3}{P0_1} \text{ and } P1E = \frac{P1_2 - P1_3}{P1_1} \quad \dots\dots\dots (2.6)$$

where P0_1, P0_2, P0_3 and P1_1, P1_2, P1_3 are ordered from high to low magnitude.

Rod-like ferrous objects should have a near zero eccentricity, while ferrous plates have positive non-zero values. Barrow and Nelson used an eccentricity threshold of 0.3 to discriminate between rod-like ordnance and plate-like clutter.

NSR is a normalized measure of inversion residual size. It is equivalent to a normalized RMS inversion residual and can vary from 0 to 100 percent.

$$NSR = 100 \cdot \frac{\sqrt{(\text{obs} - \text{calculated_data})^2 / \text{data_error}^2}}{\sqrt{\text{observed_data}^2 / \text{data_error}^2}} \quad \dots\dots\dots (2.7)$$

High NSR values can be used as a flag to drop targets anomalies that have an irregular response pattern that cannot be matched by the response from a dipole polarizability model, either because the target shape is completely unlike a single compact object or there is no conductive target present. NSR is plotted versus target depth in Figure 2.22, showing a correlation between target depth and increasing NSR. If background-noise data are inverted, **DNTDipole** estimates a large target depth with a NSR inversion residual near 100%. The large target depth produces a flat calculated data pattern matching the flat anomaly pattern of null-signal, background noise. Large target depth estimates indicate no UXO target, particularly when searching for mines.

Pasion model parameters are shown in the bottom row of Figure 2.22. The two Pasion parameters that we have found most useful are both related to polarizability transient slope. Pasion *b* is a power-law decay constant. Pasion [29] finds that ferrous objects should have *b* values greater than 0.8, providing a method for distinguishing between ferrous and non-ferrous targets in the absence of useable total-field magnetic data. We have observed that UXO generally have longitudinal Pasion *b* values near 0.8 and less well determined transverse *b* values varying around 1. Excursions away from those expected Pasion *b* values often flag clutter or objects with unusual shape. In a similar way, Pasion model parameter *c* is an exponential rate-constant (i.e., inverse time-constant) controlling late-time polarizability transient slope. UXO tend to have Pasion *c* values of 1 or less, while small objects with quick decay have larger exponential decay values. Many UXO do not get into true late-time behavior until 10 msec or later, but TEM measurements out to 2 msec can put an upper bound on Pasion model *c* and help distinguish between small objects with short polarizability transient and larger UXO with a more persistent response.

If the number of possible UXO types is limited, *DNTDipole* has an option to invert models from a library of UXO prototypes. It reports the UXO model type that produces the best match to observed data. If there are too many possible UXO types, the library search approach is less effective and discrimination must be based on more general properties like target permeability and shape symmetry.

Blossom Point Ranking Metric

Individually, polarizability model parameters provide useful information for target discrimination. Their utility can be increased by combining them into a scalar **ranking metric** based on multiple discriminant analysis of model parameter estimates from calibration data [30]. We have derived both shape-based and shape and size based rankings to classify modeling results. We discuss classification by shape below. We have deferred our discussion of classification by shape and size until we discuss the Aberdeen test.

Classification by Shape. Since most UXO are ferrous and have an elongated shape with cylindrical symmetry, classification by shape provides a useful tool for target discrimination. We used model parameter estimates from inversion of Blossom Point and Aberdeen calibration grid data to construct a shape-based ranking metric.

Using multiple discriminate analysis, within and between groups, we have estimated model parameter weights to achieve maximum separation of target responses into four groups, rod-like, sphere-like, disk-like and wire loop. Table 2.2 lists the parameter weights that we used to calculate a three-parameter discriminate function. The first discrimination parameter, *d1*, accounts for 78% of the shape discrimination power in our calibration data, the first two variables account for 94% and using all three variables accounts for nearly all shape discrimination power. It is interesting to note that *d1* relies most heavily on $\log_{10}(P0_R)$ and spheroid/ellipsoid f-test values, indicating that they are the two most robust indicators of model shape.

Table 2.2: Loading eigenvectors for shape-based discrimination parameters.

Shape-Based Discrimination Parameters			
Model Parameter	<i>d1</i>	<i>d2</i>	<i>d3</i>
sphere/ellipsoid f-test	-0.0372	0.7245	-0.5974
spheroid/ellipsoid f-test	-0.6297	-0.6295	-0.6801
loop/ellipsoid f-test	0.0009	-0.0904	-0.0167
$\log_{10}(P0_R)$	0.7162	-0.0377	0.4163
P0_E	0.0143	0.0604	0.0028
$\log_{10}(P1_R)$	-0.2886	-0.0683	0.0524
P1_E	-0.0004	-0.0185	-0.0112
PB_1	-0.0600	-0.2226	-0.0584
PB_2	-0.0420	-0.1041	-0.0199
PC_1	0.0178	-0.0157	-0.0180
PC_2	0.0004	0.0013	0.0004

Figure 2.23 shows the separation of Blossom Point target data into groups based on shape discrimination variables *d1* and *d2*. The scatter plot (left) exhibits good separation between rod-like objects and clutter. It appears that many of the plates get lumped in with the rod-like targets rather than being discriminated as being disk-like. Figure 2.23 (right) is the resulting discrimination ROC curve for the Blossom Point data set, based on shape.

2.4 PREVIOUS TESTING OF THE TECHNOLOGY

The adaptation of the Zonge NanoTEM technology for use in the dynamic survey mode commenced in late 1999. Starting after its introduction in 1992, the NanoTEM system was

applied not only for shallow mining and groundwater exploration, but also to problems involving shallow environmental site investigations. Environmental applications of NanoTEM using static measurements have been reported on many occasions during the years between its introduction and its adaptation for use as a dynamic survey method for UXO location and identification [14, 31]. Zonge's experience with using NanoTEM in these applications highlighted the need for dynamic measurements mainly because of the need to improve productivity. Development of the NT-32 imbedded NanoTEM transmitter began in 1998. We started experimenting with dynamic measurements using a rudimentary antenna cart in 1999 (*Figure 2.24*). Those early experiments lead to the deployment of a sled-mounted DNT system to Gambell in early 2000 [15]. The Gambell survey represents our first deployment of a NanoTEM system to dynamically acquire NanoTEM data. In that survey, we successfully acquired transients at 1 sec intervals with the 15-ft antenna array shown in *Figure 2.2*. In 2001, Zonge performed a survey for the City of Tucson using the Model 1999 cart (*Figure 2.24*) [32].

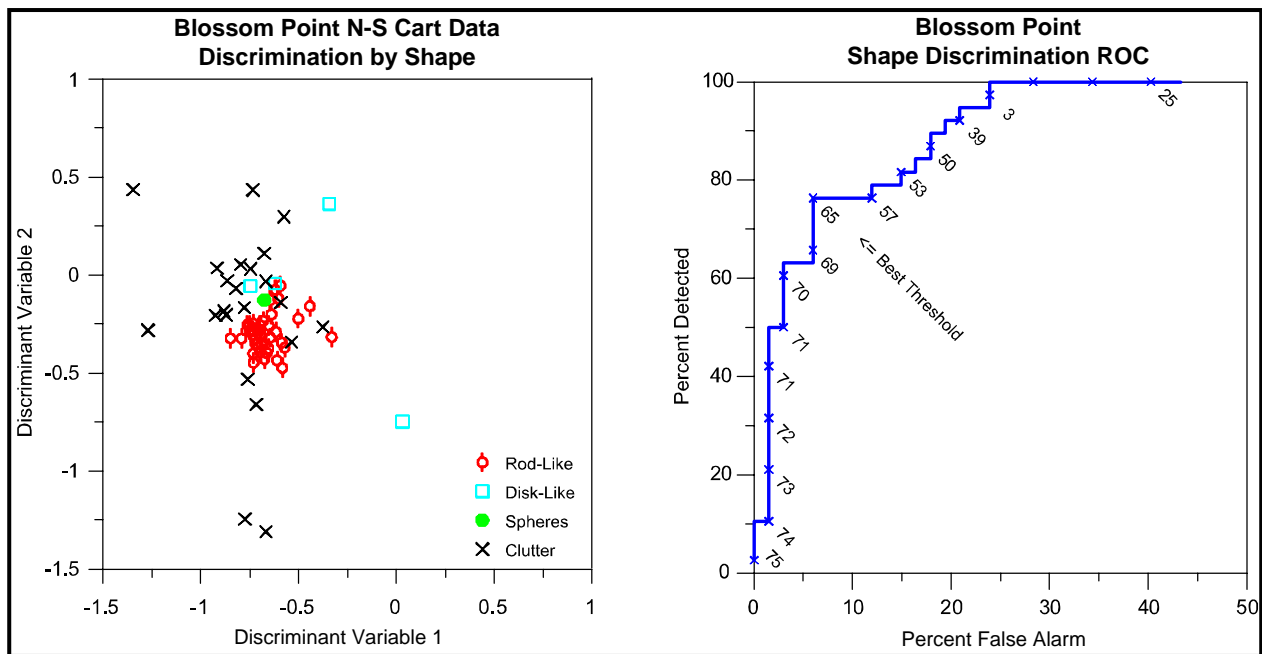


Figure 2.23: Separation of targets at Blossom Point using shape-based discrimination parameters $d1$ and $d2$.

Work on this ESTCP contract began in May 2001. Between that time and August 2002 when we conducted the demonstration at Aberdeen, we have conducted demonstrations at the NRL Baseline Ordnance Characterization Test Site located at Blossom Point [7], and at the Former Fort Ord ODDS site [33]. The latter demonstration was funded under a separate contract administered by the U.S. Army Corps of Engineers. Results from the Blossom Point demonstration have been reported [9, 17]. The results of the two aforementioned demonstrations are briefly summarized below.

2.4.1 Blossom Point

Conducted in December 2001, the objective of the Blossom Point demonstration was to demonstrate our degree of operational readiness and to provide an opportunity to compare the DNT system with existing systems. Furthermore, our project plan provided for a “Go – No Go” decision by ESTCP management that was to be based on the satisfactory completion of a demonstration at Blossom Point. The Blossom Point results were formally communicated to ESTCP management in the form of an Interim Report [17]. Included with that report was a documented



Figure 2.24: Early versions of the DNT antenna cart.

data set of DNT data acquired during the demonstration. Among other things, the demonstration at Blossom Point gave us the opportunity to directly compare the sensitivity of the DNT system with that of two Geonics systems, the EM-61 and the EM-63. This comparison indicated that DNT was marginally less sensitive on average than the EM-61 (~3dB) while it is significantly more sensitive than the EM-63 (~10dB). We completed the demonstration with only minor problems and therefore we did indeed demonstrate that we were operationally ready to proceed with a full demonstration at Aberdeen. With regard to the “added value” in the DNT system, three things stand out in our mind:

1. The DNT is significantly more sensitive (~20dB) than the aforementioned systems when comparing the responses to small conductive non-permeable targets (e.g., targets comprised of aluminum or copper).
2. Although the horizontal components have a significantly higher noise level than the vertical component (6-15dB), they are surprisingly coherent at early times. These components, particularly the v horizontal component (i.e., transverse to cart motion), are sensitive indicators of target position relative to the line when viewing profile responses that do not pass directly over the target. Thus, the additional independent data arising from the horizontal components significantly improves model-based interpretation because they help to accurately locate the target.
3. Similarly, the ability of the DNT system to simultaneously record 3 linearly independent vector components at each field point adds significantly our ability to interpret anomalies based on over-determined parametric models. With 3 times the data as its competitor the EM-63, the DNT system allows an area to be surveyed at reasonable lane spacings with assurance that there will be adequate spatial sampling of the anomaly footprint. These additional vector components eliminate the need for two orthogonal surveys as required with MTADS for performing their “3- β ” analysis [27].

High sampling rate and three-component data improve noise suppression. Future work may be able to use ideas from Spies [34] to improve reduction of background noise.

2.4.2 Fort Ord

In July, 2002 we demonstrated the DNT system at the Former Fort Ord near Monterrey, CA. The work was supported by the U.S. Army Corps of Engineers, Engineering Research and Development Center (ERDC) under contract no. DACA42-02-P-0131.

2.5 FACTORS AFFECTING COST AND PERFORMANCE

There are three factors that affect the cost and performance of the DNT system:

1. Capital Equipment Costs
2. Crew Size
3. Survey Speed

2.5.1 Capital Equipment Costs

The cost for a DNT system, exclusive of the GPS survey equipment, runs approximately \$50K. Thus the basic equipment cost is approximately 2.5 times that of a Geonics EM-61 MkII. However, if we were to reconfigure the antenna array so that it resembles an MTADS system containing 3 EM-61's or, perhaps, a system of 2 EM-61 carts lashed together and operating as a synchronized system, the capital cost of the DNT system hardly changes while the cost of the EM-61 system multiplies directly as the number of antenna units. Thus, even for simple detection problems, a DNT system can have a capital cost that is similar to that of a synchronized system of two or more EM-61s.

2.5.2 Crew Size

In the configuration that we demonstrated, a minimum crew of 2 people is required to operate the equipment (1 person to carry the receiver, and 1 person to carry the GPS equipment and push the antenna cart). However, all demonstrations discussed in this report were conducted with a 3-man crew. Our backpack-mounted DNT transceiver is heavier than the EM-61 equipment. Therefore, a 3-person crew becomes necessary when working long days in rough terrain.

2.5.3 Survey Speed

The DNT system is a broadband system. In its Profile acquisition mode, it samples 31 time windows along the secondary transient signal on each of 3 independent receiver channels. The Aberdeen demonstration, in particular, has shown that there is little if any penalty to pay for the additional information provided by DNT, either in daily production or in sensitivity for detection. Our demonstration has shown that good quality DNT data may be acquired at normal walking speeds of 0.6 to 1m/sec. As with all EMI systems, however, improvements in signal-to-noise ratio (SNR) can be achieved by surveying at lower speeds and then resorting to post-acquisition low-pass filters to increase the SNR. In our data processing, we improve the SNR by filtering and/or stacking. As we indicated in *Section 2.3.2*, we normally apply a 7-point \cos^2 tapered stack and then decimate our data by a factor of 4. Assuming that our survey speed never exceeds 1 m/sec, these operations result in a sample interval of 12 cm or less. A good rule of thumb for proper sampling of a dipole anomaly is to make sure that the sampling is no larger

than half the depth to the anomaly (in this case, the target depth plus the height of the Tx antenna = 17cm for the DNT cart used at Aberdeen). Clearly, therefore, we cannot apply more decimation without undersampling shallow target anomalies, unless we reduce survey speed and hence the maximum sample interval.

A less elegant, but efficient way to improve SNR is to increase the signal strength. We can increase the signal by increasing the transmitter moment, either by adding turns to the antenna and/or increasing the transmitter current. Unfortunately, either way of increasing transmitter moment carries a penalty with it. By adding turns to the transmitter, we add self-inductance to the antenna and thereby significantly increase the transmitter turn-off time. A rule of thumb is that a doubling of the number of turns increases the turn-off time by a factor of 4. But early time induction is driven by the time rate of change of the transmitter current. Even though we gain in transmitter moment (i.e., a factor of 2) we lose early time induction (i.e., a factor of 4).

Unfortunately, the basic laws of physics limit us when we try to increase the current in order to increase the moment without changing the number of turns in the transmitter. In this case, we are limited by the back-EMF generated in the transmitter coil (which after all is simply an inductor) when we try to shut-off the current. Only marginal increases in transmitter current are feasible using our present high-voltage switching devices without exceeding their peak switching voltage specification and thereby causing failures. However, in the near future significant increases in the transmitter moment of portable metal detection technology such as DNT may be achieved through the development of a pulse-transmitter based on resonance principles⁹.

In summary, increasing the number of transmitter loop turns sacrifices early-time response, but increases late-time signal to noise. A system designed to detect and characterize larger UXO should have more transmitter moment than the current DNT system.

2.6 ADVANTAGES AND LIMITATIONS OF DNT

The NanoTEM system was designed to generate and measure secondary transient fields over the time bandwidth ranging from $1 \leq t \leq 2000 \mu\text{s}$. Through the use of fast current switching technology, NanoTEM has demonstrated that it has a sensitivity that is comparable to that of the EM-61 metal detector for a broad range of UXO targets. It has significantly more sensitivity to small conductive and non-permeable objects. It does this with a transmitter moment that is only about a tenth that of the EM-61¹⁰. However, DNT as it is presently configured is not capable of measuring transients at time delays beyond about 4 ms. For very large targets (e.g., 155 mm, 6-in, and 8-in artillery projectiles), the principal time constants are more than 10ms. The so-called “late-stage” of the transient decay is an important parameter for discrimination [43]. If the measurement of transients beyond the 4 ms limitation of the present DNT system is essential, as it appears to be for large targets, then the present DNT system will require further modification so that it can measure transients over a longer time period. At the same time, the transmitter will require modifications to dramatically increase its moment (increase both current and transmitter

⁹ Zonge is currently funded by SERDP to develop a high power transmitter based on resonance principles. We expect that the resulting transmitter will generate moments on the order of $10^3 \text{ A}\cdot\text{m}^2$.

¹⁰ Others have estimated the moment of the EM-61 to be 200-250 $\text{A}\cdot\text{m}^2$. Based on self-inductance measurements on the EM-61 Tx coil, we estimate that the EM-61 transmitter has 30 turns and hence a moment of $180 \text{ A}\cdot\text{m}^2$ when transmitting 6 A. The transmitter moment of our 8-turn DNT Tx transmitting 3 A is $24 \text{ A}\cdot\text{m}^2$.

turns) and to slow down the transmitter turn-off times by an order of magnitude. In short, it will be necessary to shift the time-bandwidth of the DNT system by a decade to the right.

The main advantage of the NanoTEM system is its multi-channel capability. For this demonstration, we have configured a 3-channel antenna system in which we measure the transient fields along the three principal axes of the antenna cart (i.e., an XYZ receiver antenna array). As we have suggested in the previous section, one can imagine other configurations involving 3 receiver antennas that would have performance advantages in the detection stage of UXO surveys over the antenna system we describe in this report. For example, a DNT system can be configured that is similar to the MTADS system. Such a system would provide improved production when deployed for UXO detection.

We maintain that the main advantage of using the 3-axis DNT system described here is that we are able to perform shape-based target discrimination using data from a single set of closely spaced survey lines (e.g., $\frac{1}{2}$ -m) using the dipole model parameterization described earlier in this section. In the discussion that follows, we show how the horizontal components help interpret anomalies in both qualitative and quantitative ways.

2.6.1 Background Noise levels

It is useful to study the background noise levels of the three measured vector components (u,v,w) of the DNT system. We have compiled the RMS background noise levels for each of the three components using a data line taken from the Calibration Lanes data set at the Aberdeen test area. We plot the results in *Figure 2.25*. The points represent the RMS noise level for each of the 31 time windows of the NanoTEM data acquisition system. The colors Red, Green, and Blue correspond, respectively, to the 3 receiver axes (u,v,w). The solid curve represents the expected attenuation of noise as a function of window delay time when the noise field is truly random “white” noise. This theoretical noise reduction results from the fact that the window or gate width in the NanoTEM system increases logarithmically as delay time (*Table 2.1*) and in the presence of truly “white” noise, the noise level in the window decreases inversely as the square root of the window width.¹¹

There are three things to note about the noise: 1) in the late early time region ($10 \leq t \leq 40 \mu\text{s}$ or gates 7-12), the noise levels in the horizontal components are lower than the vertical component (blue) by a factor of 2 or more (6dB); 2) in the intermediate times ($10 \leq t \leq 200 \mu\text{s}$; gates 7-18), the

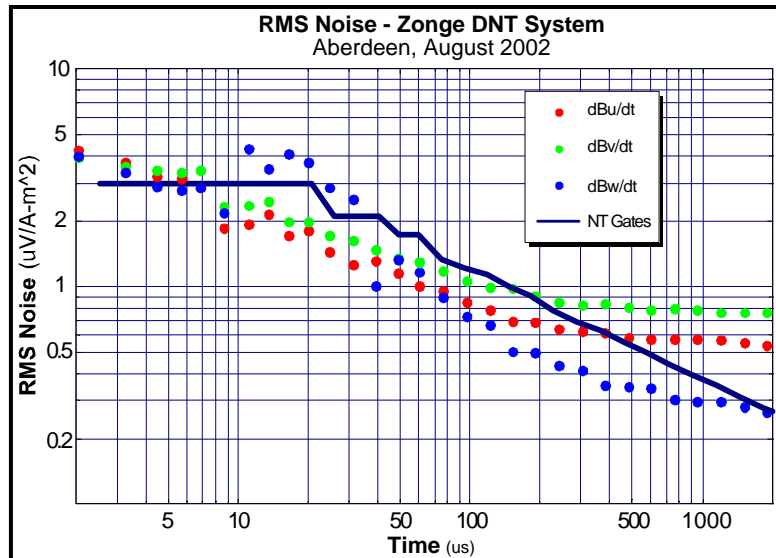


Figure 2.25: RMS noise levels at Aberdeen by DNT acquisition channel and vector component.

¹¹ Since the NanoTEM system is a digital system, the noise level decreases as the number (N) of sample points that are summed in each window.

noise on all three channels falls off roughly as $1/t^{1/2}$, consistent with the attenuation predicted by gate width considerations and a white noise model (*solid curve*); 3) at late times ($t \geq 100\mu\text{s}$), the noise level of the horizontal components is 2-3 times (6-10 dB) that of the vertical component.

Early time noise in the DNT system is dominated by instrument noise. The high noise levels in the vertical component near $20\mu\text{s}$ is caused by small residual transmitter currents. The vertical loop is maximally coupled with the transmitter while the two horizontal components are, in principle at least, null coupled. At late times, instrument noise is at a minimum, and the noise levels reflect the ambient electromagnetic noise field. The vertical noise field is always lower because it couples well into the earth and is attenuated. Since the lines at Aberdeen were run in an east-west direction, and the cross axis (v) component is higher than the in-line (u) component, we can say that the noise field is oriented about 35° off of N-S.¹²

2.6.2 Horizontal Components Improve Relative Locations

In more conventional applications of the DNT system, we have noted that zero-crossings of the horizontal components are an indicator of target position, just as the anomaly peak of the vertical component is a position indicator. In more conventional applications of the DNT system, we have noted that zero-crossings of the horizontal components are an indicator of target position, just as the anomaly peak of the vertical component is a position indicator. A plot with vectors representing the horizontal components helps to graphically illustrate how the horizontal components help to locate the target's X-Y position. *Figure 2.26* shows a 2m x 2m area that is centered on target cell D12 in the Calibration lanes at Aberdeen. This cell contains a 105mm HEAT projectile buried at a depth of 40cm. In the figure, we have plotted all data points falling

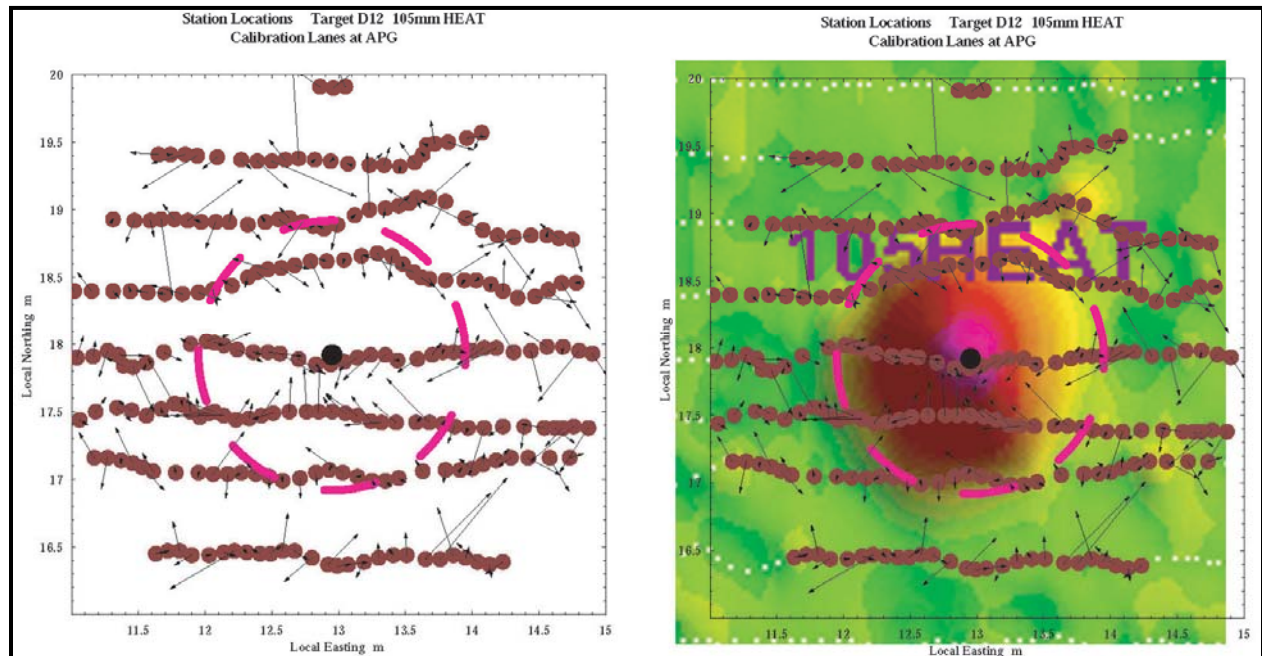


Figure 2.26: Vector plot (left) showing horizontal DNT field over cell D12, Calibration Lanes, Aberdeen. In the right hand panel, we overlay the vector plot on a color map of the vertical field.

¹² Since we do not have a sign for the noise, we can only estimate the magnitude of the angle. Note that along E-W lines, the v-axis of the cart is pointed either north or south depending on cart heading.

within a 2-m radius of the anomaly center, a total of 230 points.¹³ Also shown on the figure are the position of the target pick (black point), and a 1-m radius circle (dashed magenta line) that represents the area within which the data points are generally anomalous (i.e., the target “foot print”). The vectors represent the direction of the horizontal field and the logarithm of its magnitude. For 3-D targets, the vectors point toward the target center. Thus, on the third line from the bottom of the plot, we see a very coherent set of vectors that seem to converge to a point slightly SW of the target point. Similarly, the vectors along the centerline suggest that the line passes a small distance to the north of the target center (as evidenced by the small southward component on the vectors). The range for these horizontal vectors is not large. There is no coherent pattern on the lines that cross 1 m (nominal) north and south of the centerline.

Figure 2.26 qualitatively illustrates an important point that we noted in our Blossom Point report and further amplified in recently presented technical papers [44-46]. For compact 3-D targets, the u-component (horizontal component in direction of cart travel) is bipolar with the negative peak occurring as the antenna approaches the target, a crossover occurring directly over the target and a positive peak occurring as the antenna moves beyond the target.¹⁴ The data are over-sampled along the profile and therefore the position of the anomaly peak along the profile is easier to pick than a zero-crossing. Consequently, the u-component adds little to our knowledge of the horizontal position of the target. However, the EM response is under-sampled in the direction transverse to the profiles. Thus the Y position of the target is less certain. We can see from the figure that the transverse horizontal field provides useful information about which side of the center profile the target lies. Clearly, the addition of a 2nd set of profiles perpendicular to the first, as recommended by Nelson and others [27] solves the problem handily. But it does so by doubling the incremental cost of field production (i.e., twice as many profiles). The transverse horizontal component provides crucial information about the cross-track target position in the absence of that set of orthogonal profiles.

We are compelled to make a final point about the “real” data sets we have been using to illustrate many points in this report. At Blossom Point and in the Standardized Test Site at Aberdeen, we have surveyed over targets that have been buried on a precise metric grid. The choice of a ½-m grid spacing guarantees that there will be a profile that passes directly over each of the target. A centerline profile assures us that we will make a good estimate of the along-track position of the target by picking the peak of the vertical field anomaly. However, the anomaly position is fixed by the zero-crossing of the appropriate horizontal component. But the zero-crossing is easily disturbed by noise. In the real world, the probability that the cart passes directly over the target will be low. It is equally likely that the cart will be offset any distance from 0 to 25cm from the target. Thus a far more realistic scenario to model is the case where none of the data profiles pass directly over the target. In such a case, there will be two profiles with offsets that are less than ½-m from the target center. Later in this section, we show that our 3-component modeling does significantly better with data where all profiles are offset from the target.

¹³ The anomaly peak was located in Oasis Montaj using a grid-based peak detector. The anomaly center is not necessarily the X-Y location of the target.

¹⁴ Carlson and Zonge [2-3] have noted that the bipolar behavior of the horizontal components is inverted when traversing a linear feature such as a buried power line or pipe.

2.6.3 Physics-Based Parameterization

Our model studies using synthetic data conclude that the addition of horizontal components significantly improves the quality of model-based inversions, if horizontal noise levels are not too high [47-49]. That conclusion has recently been reaffirmed by Grimm [50] using a static data set acquired at Blossom Point with an EM61-3D. Using generalized regression neural networks (GRNN) and probabilistic neural networks (PNN), Grimm compared the relative classification performance of the EM61-3D when he parameterized subsets of his Blossom Point data with a dipole model similar to ours and input the resulting parameters into the GRNN and PNN classifiers. Grimm concludes that:

In general, false-positive rates were decreased by 40% or more when using the full multi-channel, multi-component data over multiple-component, single-channel or single-component, multiple-channel decimated data sets.

To help determine whether or not the horizontal components improve performance for classification, we have re-analyzed our Blossom Point data for 4 cases:

1. N-S data, $\frac{1}{2}$ m line spacing) – 3-Components (XYZ)
2. N-S data, $\frac{1}{2}$ m line spacing – Single component (Z)
3. N-S data + E-W data (E-W @ 1 m line spacing) – 3-Components (XYZ)
4. N-S data + E-W data (E-W @ 1 m line spacing) – Single Component (Z)

Following the lead of Grimm [50], we performed shape-based

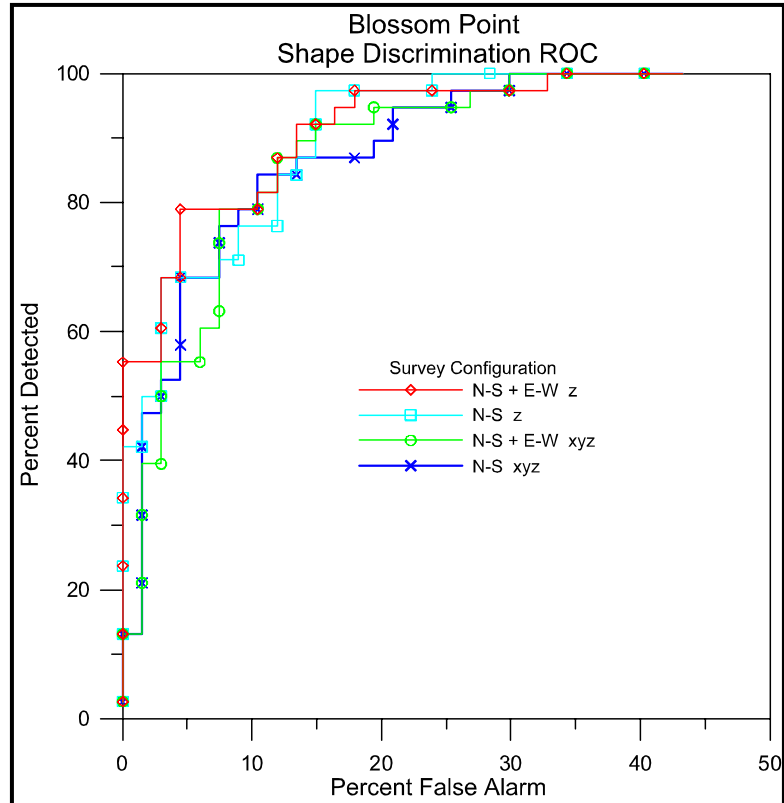


Figure 2.27: Discrimination ROC curves for Blossom Point showing relative performance for single component and multi-component DNT data.

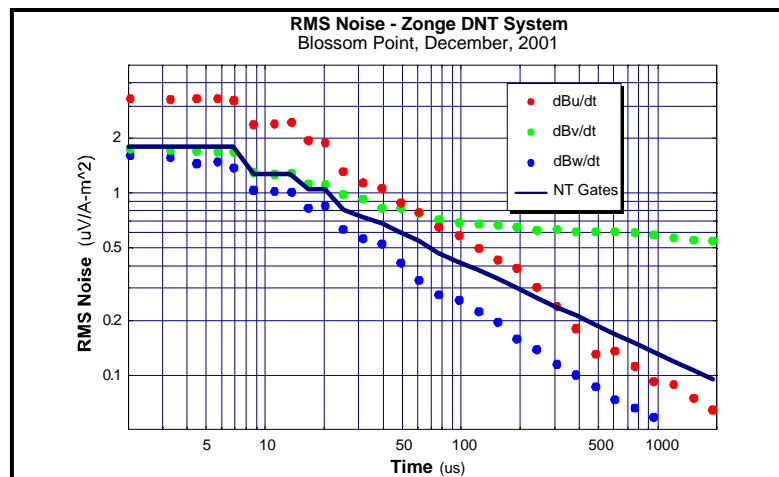


Figure 2.28: RMS noise levels at Blossom Point (N-S lines) by DNT acquisition channel and vector component.

discrimination on the model results generated by these four data sets. We show resulting discrimination ROC curves in *Figure 2.27*. These results suggest that we actually do marginally better at Blossom Point by using only the vertical component (red and turquoise curves). This contradicts our intuition, our conclusions and those of others based on synthetic modeling, and those of Grimm [50] that are based on static multi-component multi-channel TEM measurements.

Our numerical experiments indicate that the correct parameterization of a given anomaly is significantly affected by noise level. As we observed at ATC, and at Blossom Point (*Figure 2.28*), noise levels are higher in the horizontal components. *Figure 2.28* shows that relative to the X and Z components, the noise level is significantly higher at late times on the Y component.¹⁵ As we have indicated previously, the horizontal component that is transverse to the lines is more important than the inline component since the transverse direction represents the direction in which the anomaly is under-sampled. Grimm used statically acquired data for his analysis and, presumably, the relative noise level for all three components at each of the time gates has been reduced by at least 15 dB by synchronous stacking.

Ajo Tests – Zonge maintains a small geophysical test site west of Tucson in cooperation with the Dept. of Mines and Metallurgy at the University of Arizona. At this test site (Ajo test site), we have buried a number of UXO specimens and other targets of interest. To further demonstrate the value of horizontal components (or lack thereof), we conducted DNT surveys at the Ajo test area with two different receiver array geometries:

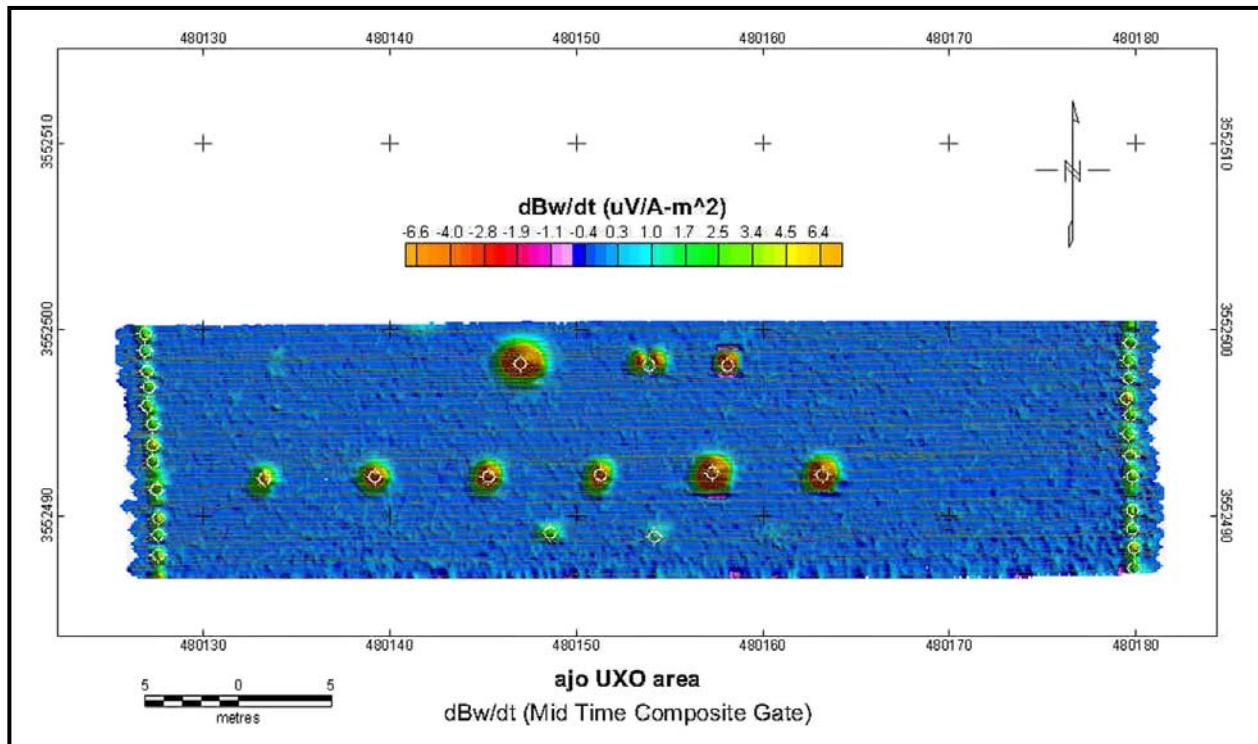


Figure 2.29: DNT map of DNT vertical response (12-21 composite gate = 68 μ s) of Zonge Ajo test site.

¹⁵ Figure 2.28 summarizes noise for the N-S lines. That means that the horizontal noise field corresponding to the antenna cart Y component corresponds to the E-W direction.

1. **XYZ 3-component geometry** – Three mutually orthogonal antennas similar to those pictured in *Figure 2.4*. (The actual cart employed in our experiments is pictured in the foreground of *Figure 2.6*.)
2. **YZZ 3-component geometry** – Using the same cart, we measure the Z field at two heights above the ground. The only horizontal component measured is the Y component (i.e., transverse to cart motion).

For each of these antenna array geometries, we acquired two sets of E-W lines at $\frac{1}{2}$ -m intervals. The second set of lines was offset from the first by $\frac{1}{4}$ -m. We show a color intensity map of the Z component for an intermediate composite time gate in *Figure 2.29*. The top row has 3 targets including a 1-m long pipe (horizontal) and 2 shorted loops. The second row contains 6 targets consisting of inert UXO items. The third row contains 3 57mm projectiles at different depths. The anomalies at the row ends are caused by aluminum nails we placed to mark the positions for lane marker tapes.

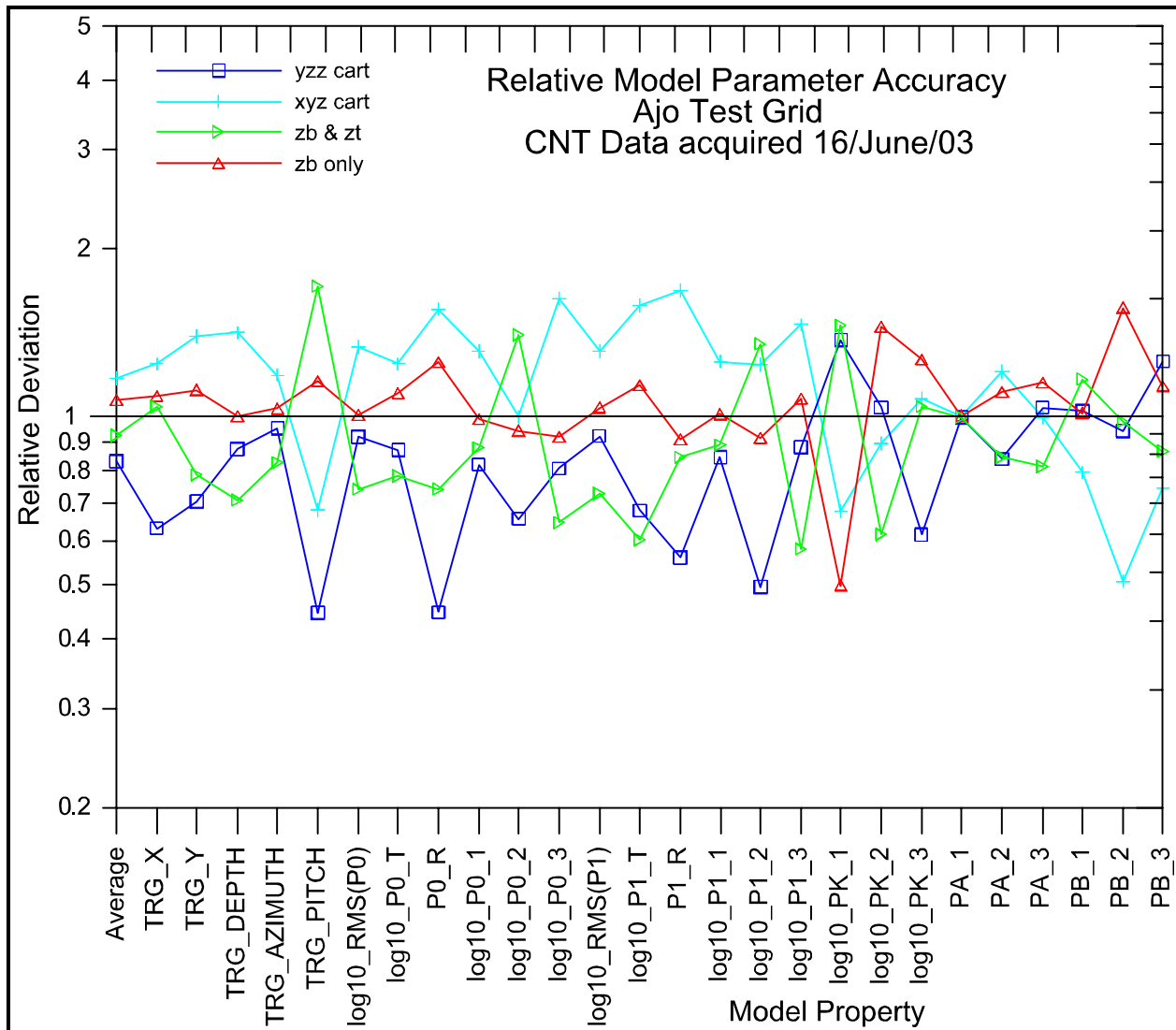


Figure 2.30: Figure showing relative accuracy for parameter estimation with DNTDipole for various receiver antenna configurations.

We estimated model parameters for 9 targets (top and middle rows in *Figure 2.29*) with **DNTDipole** using data acquired at our Ajo test site. In addition to the XYZ and YZZ antenna configurations enumerated above, we used two vertical component configurations. One used only bottom loop data, Zb, and another used both bottom and top loop data, Zb and Zt. In *Figure 2.30* we compare the relative parameter estimation error for each of the 26 model parameters estimated by **DNTDipole**. "True" model parameter values were first estimated by averaging modeling results from all four survey configurations. Then, deviation of each survey configuration's model parameter estimates from the group mean was used as a measure of parameter estimate accuracy. To get a consistent plot scale, individual deviations for each model parameter were normalized by the parameter's average deviation for all four data sets. Thus the relative deviations plotted in *Figure 2.30* vary around 1. Values lower than one for a particular survey configuration indicate better than average accuracy relative to the other survey configurations tested. Modeling of this Ajo data set indicates that a YZZ receiver antenna configuration is somewhat better than an XYZ configuration. Both are better than a two component ZZ configuration with bottom and top vertical component loops. Least accurate is a single component survey using one vertical component receiver loop.

Based on analyses of both the Blossom Point and Ajo data sets, we must conclude that there is no demonstrable improvement either in parametric estimation or in classification using a 3-component (XYZ) receiver antenna array in dynamic surveys. In fact, noisy horizontal components seem to slightly degrade parameter estimates. The degradation in parameter estimation and hence in classification performance that we observe when modeling dynamic data is probably caused by uniformly higher horizontal-component noise levels. We are aware that this conclusion contradicts synthetic model studies (even our own when using uniform noise for all three components) as well as an impressive experimental study by Grimm [50]. We conclude that the most likely explanation for the difference between our conclusion and that of Grimm is that static measurements have greatly reduced position errors and significantly lower noise levels overall. An important result of our Ajo study is that it reaffirms an earlier conclusion that the YZZ antenna array configuration is the best 3-component configuration for dipole model parameterization.

3. DEMONSTRATION DESIGN

3.1 PERFORMANCE OBJECTIVES

Our demonstration at ATC was conducted at the newly constructed Standardized UXO Technology Demonstration Site [8]. This site has been constructed specifically for providing a site where UXO detection and classification technology can be exhaustively tested under realistic conditions. Our performance objectives are listed in *Table 3.1*. Our basic qualitative objective has been, and continues to be, to demonstrate that the NanoTEM system compares favorably with competing technology such as the Geonics EM-61 for UXO detection. Secondly, we hope to demonstrate that this fast multi-component multi-gate TEM system can provide useful parametric information to aid in target characterization and classification. To achieve this goal, we believe that it is necessary to demonstrate not only our ability to acquire DNT data in an efficient cost-effective manner, but also our ability to efficiently process, display, and interpret these data. *Table 3.1* contains quantitative performance objectives that serve to measure how well we met these objectives.

Table 3.1: Quantitative Performance Objectives for the DNT Demonstration at Aberdeen.

Performance Objective	Performance Metric	Actual Performance
1. Survey productivity	$\frac{3}{4}$ acre/day	1 acre/day
2. Detection Efficiency (POD)	> 90% POD	80% (Blind Test Grid)
3. Discrimination	?	45%
4. Classification	?	13.9%

A method for reliable classification of target anomalies is the ultimate goal and, indeed the primary justification for introducing new or improved technology such as DNT. Therefore, during the life of this project we have pushed to develop interpretation tools such as our dipole-modeling program *DNTDipole* to support the ability of the DNT system to acquire multi-component transient data. While we believe we have been very successful in demonstrating all of our tools for data processing and interpretation, we freely admit that an important element in achieving our goals in Classification is experience in interpretation using these tools. At Aberdeen, *DNTDipole* was being developed and modified even as we were trying to meet a 30-day deadline to submit our target lists for scoring. Therefore, to the extent that we did not meet our goals in classification, we argue that the responsibility should not be placed on a failure in the basic technology. We submit that as our experience with using these tools grows, so too will our performance in classifying targets.

3.2 SELECTING TEST SITES

To meet the overall objectives of our project, we require areas that have been seeded with a variety of UXO and Clutter objects and for which the ground truth (i.e., the target identity, position, and attitude) have been carefully recorded. Both the NRL Blossom Point Site and the site at Aberdeen meet this criterion. The Blossom Point site is a relatively small rectangular-shaped area comprised of a grid of 6m x 6m test cells for which ground truth is available to the demonstrator. Most of the targets generate anomalies with good SNR so that target detection is

not an issue. The site has been well graded and maintained in an effort to provide an opportunity to quickly and efficiently acquire data over the site. By contrast, the Aberdeen site has an area of nearly 20 acres, some of which present extreme “challenges” for surveying. By and large however, the bulk of the site (more than 15 acres) is accessible to man-portable cart-mounted survey platforms such as the DNT system supported with RTK GPS positioning. A demonstration at the Aberdeen site, therefore, provides an opportunity to test and evaluate the performance of UXO technology under realistic conditions in four phases of its operation: 1) in its operational or data acquisition phase; 2) in its detection phase; 3) in its characterization, and 4) in its classification phase.

From our viewpoint, it is unfortunate that most of the ground-truth at Aberdeen remains unavailable to the demonstrator. With the exception of a small area (Calibration Lanes), the ground-truth is being held confidential by the Aberdeen Test Center (ATC). The demonstrator, therefore, can evaluate his UXO technology only in the sense of the score resulting from the submission of a list of targets detected, their locations, and their classification (i.e., UXO/Clutter). In that context, it is our opinion that the design of the Calibration Lanes is significantly flawed. The purpose of a “Calibration Grid” is presumably to provide the demonstrator with the opportunity to survey over test objects identical with those that will be encountered in the other areas wherein the ground truth remains unavailable. The Calibration Lanes do indeed contain a good variety of objects placed at different attitudes and depths. But many of these objects have been placed at depths where they are undetectable with the DNT system. Even at their shallowest depths, many of the targets have a low SNR – too low for reliable modeling. The Calibration Lanes should provide the demonstrator with a good look (i.e., a high SNR anomaly) for each target at least at its minimum depth.

3.3 SITE HISTORY/CHARACTERISTICS

The standardized demonstration site at Aberdeen was constructed in 2001 and 2002 with the U.S. Army Corps of Engineers (USACE) taking the lead. A similar facility is currently being constructed at the Yuma Proving Grounds (YPG) located near Yuma, AZ [36]. Both the ESTCP and SERDP programs have supported the project. The ATC site was formerly used for a multitude of purposes related to the testing of ordnance. After the site was designated for use as a standardized demonstration site it underwent a thorough decontamination that involved phases of detection with magnetometers and EMI followed by retrieval and deactivation or destruction of the resulting objects whenever necessary. The mostly clean site was then seeded with dummy UXO specimens and with clutter objects. The site is maintained by the Aberdeen Test Center and is available for use under ground rules established by the program and published on the program’s web site (<http://aec.army.mil/usaec/technology/uxo03.html>) [37].

3.4 PRESENT OPERATIONS

As we indicated above, the site is being maintained by ATC with support from various groups from within the army as well as the ESTCP/SERDP programs. It is adjacent to an active firing range. Proximity of the test site to a firing range and the fact that areas outside the bounded test area remain un-cleared of UXO represent significant safety hazards. These safety concerns together with security rules for civilian access to the ATC grounds make it mandatory that personnel involved in demonstrations at the test site be escorted and that the escort be in radio contact with the firing range supervisor.

The site was thoroughly remediated of UXO before it was seeded with inert objects. There are a number of test wells scattered about the site that are monitored for soil moisture and, perhaps, other environmental indicators. With the exception of these monitoring activities, there are no other activities at the site.

3.5 PRE-DEMONSTRATION TESTING AND ANALYSIS

We did not conduct any pre-demonstration testing or analysis prior to the demonstration. As noted above, there is an ongoing program to monitor soil moisture and other indicators. At the time of our demonstration, the survey area was relatively dry. We originally scheduled our demonstration in May. However, site construction was delayed because of rain and partial flooding, causing corresponding delays in our schedule. Zonge was, in fact, the first contractor to conduct a full demonstration at the Aberdeen site. Although we had several rainy days during the demonstration, little or no time was lost due to weather. During wet seasons, however, access to parts of the demonstration site is no doubt considerably more difficult than we experienced and this would adversely affect survey productivity.

3.6 TESTING AND EVALUATION PLAN

3.6.1 Demonstration Set-Up and Start-Up

The Gantt chart in *Figure 3.1* shows the time line for activities involved with mobilization, fieldwork, and demobilization. We assembled equipment and field-tested it on August 12-13. We shipped 765 lbs (4 boxes) of gear on Wednesday, August 14 for arrival at the Aberdeen Test Center on Friday, August 16. The crew traveled on Saturday, August 17. On Sunday, August 18, we familiarized ourselves with the area around Aberdeen, purchased field supplies and reviewed our demonstration plan. We arrived at the ATC Visitor Control Building (Bldg 379) at 7:00 am where we signed in, received badges, and received a safety briefing. After picking up our gear at the ATC freight warehouse, we proceeded directly to the field site, arriving at approximately 8:00 am.

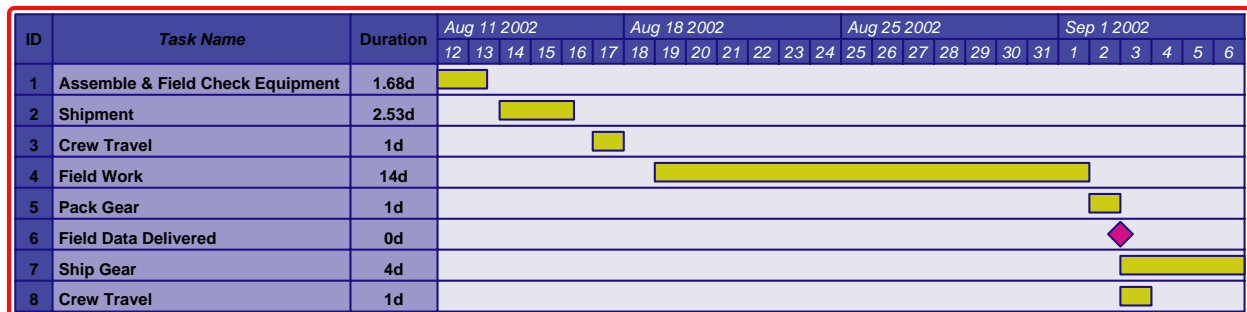


Figure 3.1: Gantt chart illustrating schedule of activities.

It took about 2 hours to assemble the antenna cart and to perform functional tests of our receiver. We setup our battery chargers in the support trailer located immediately east of the test site. The only utility required for the operation of the DNT system is 110-220 VAC 50/60 Hz used to charge batteries. Although not absolutely necessary, it is convenient to have access to power and a place to store gear near the field site. This eliminates the need to transport all gear back and forth between the field site and the hotel. At Aberdeen, the only piece of gear we transported

back to the hotel after work was the NT-32^{II} transceiver. We had a problem with getting our GPS system operational and we lost a few hours while we troubleshot that problem. However, we were operational by early afternoon of our first day on site. We surveyed the Calibration Lane area on the afternoon of the first day and we were able to show a preliminary color map to George Robitaille and other visitors the next day, August 20 (*Figure 3.2*).

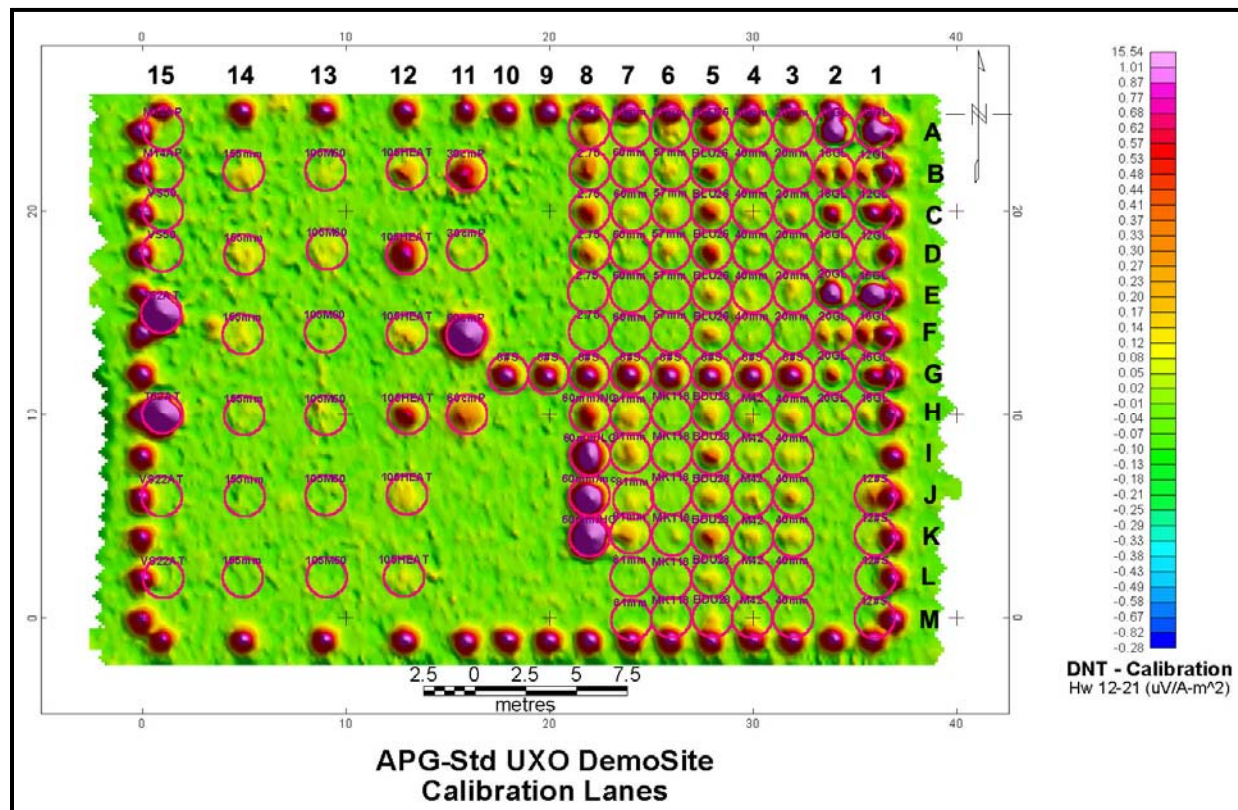


Figure 3.2: Color intensity map of the *Calibration Lane* grid at the ATC Standardized Site. Target locations have been marked and annotated with an abbreviation for their identity.

3.6.2 Period of Operation

Field operations were conducted continuously from August 19 through September 2, 2002 (*Figure 3.1*). Problems with our GPS system resulted in an interruption of data acquisition on Friday afternoon, August 23. We replaced the faulty GPS unit on the following day so that we were running again on Saturday afternoon, August 24. Aside from the GPS breakdown mentioned above, we had only minor mechanical breakdowns that were easily repaired in the field. Additionally, there were a few problems with the data that forced us to repeat five sections (~8% of the total) of our survey.

3.6.3 Area Characterized

Figure 3.3 is a satellite photo (Microsoft Terraserver, <http://www.terraserver.microsoft.com>) of the Standardized Test Site. A larger version of *Figure 3.3* has been included in the *Appendix* as file *ATC_STS.pdf*. The site has been divided into 14 areas, 12 of which are designated by numbers while the other 2 areas are designated by the letters A and B. Areas are numbered in

the order of our survey, and assigned names as listed in the legend. These areas are covered with hachures parallel to the survey line direction. Neither the Mogul Scenario (A), nor the Wooded Scenario (B) were surveyed.

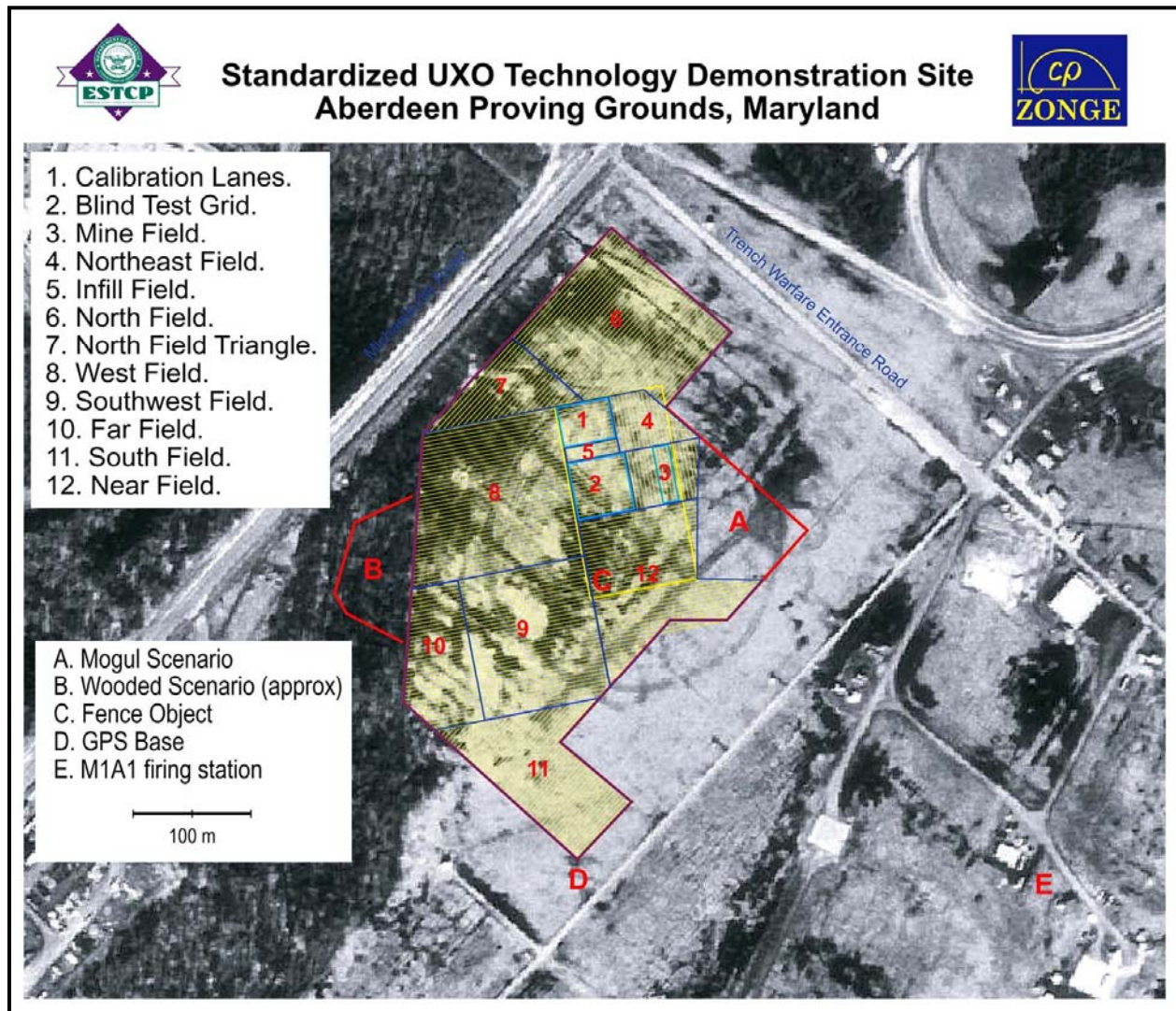


Figure 3.3: Satellite photograph (1 m resolution) showing the outline of the Standardized Test Site. The figure identifies the surveyed grids by number, and other areas or features of interest by letter.

The photo shows that the test site is a large, irregularly shaped area. Using the coordinates of various boundary markers together with the photo, we calculate the total area surveyed to be approximately 6.1 ha (15.1 acres).

The test site is clearly too large and irregular to be surveyed as a single block. The only survey information provided to demonstrators are coordinates for the site boundary posts (4" PVC Pipes set in the ground) that mark the corners of the site's boundary lines. Although highly desirable from our perspective, a system of interior grid points is not provided as part of the demonstrator's information package. The demonstrator is required to subdivide the area and

survey it using the information provided. For reporting targets and for discussion, the survey site (not including the Mogul and Wooded Scenarios) is divided into three areas:

1. **Calibration Lanes** (Area 1)
2. **Blind Test Grid** (Area 2)
3. **Open Field Area** (Areas 3-12) – The Open Field area was defined to us by ATC personnel as “all area within the site boundary excluding the Calibration Lanes (1), the Blind Test Grid (2), the Mogul Scenario (A), and the Wooded Scenario (B).

Target lists for the Blind Test Grid and the Open Field Area are scored separately.

Rather than spend a day subdividing the test site into a regular grid (e.g., 50-m grid points) with our GPS, we chose to use segments of the site boundary and their extensions as baselines from which to subdivide the site into rectangular-shaped areas suitable for our survey. Extensions of the north, west, and south boundaries of the Calibration Lanes and the Blind Test Grid provided useful interior baselines for that subdivision. This procedure leads to a “*natural*” subdivision of the survey area that minimizes the number of triangular-shaped areas and maximizes the opportunity to survey long profiles. In effect, we optimized the survey by minimizing the area that required short lines and many turn-arounds.

3.6.4 Operating Parameters

This demonstration was conducted with a crew of three people. The crew consisted of the project principle investigator, a crew chief, and a field technician. Two people are required to operate the cart while it is surveying. The third person was used to move lane markers and usually had enough spare time to do a small amount of data processing for in-the-field QC. The work involved in operating the cart is physically demanding, so job responsibilities were rotated. Although he had definite responsibilities, the 3rd man rested during his shift. We generally operated the cart for approximately 1-hr periods that started and ended with a calibration check. For each survey run, we record 3 data streams (*Figure 2.11*), TEM data, GPS data, and NAV (i.e., cart attitude) data. The size of a typical data file is, respectively, 30Mb, 5Mb, and 2Mb. On a good day, we were able to acquire six 1-hr survey sessions.

3.6.5 Experimental Design

Our main objective for this demonstration was to conduct a survey over the entire Open Field Area with sufficiently dense coverage to permit us to submit a target list that included classification of the targets that we identified. We were told to budget for a survey of 12 Acres. That area estimate was clearly on the low side. Our demonstration plan called for surveying the Open Field Area with profiles on ½-m offsets. We conducted the survey at a normal walking pace of about 0.6 m/sec. Three-component TEM transient data (31 time gates per transient) were acquired at the rate nominal of 32 samples per second. Over most of the survey, cart attitude data including cart heading, pitch angle, and roll angle were acquired at the rate of approximately 4 samples/sec. GPS position data were recorded at a rate of 5 samples/sec. This survey was treated in all respects like a production survey with the intent of meeting our demonstration objectives in an efficient and economical way. We had no time to conduct experiments or to vary any of the operating parameters. All data were processed using software and procedures discussed fully in *Section 2.3 (DNT Data Processing)*.

3.6.6 Sampling Plan

Data (Sample) Acquisition

Our demonstration plan called for DNT data to be acquired by means of a series of parallel profiles at nominal $\frac{1}{2}$ -m offsets. Due to the 1-m width of the transmitter antenna, we can be certain that the antenna not only passes close enough to each target for its detection, but also that the target will be adequately illuminated by both horizontal and vertical fields. Target stimulation by magnetic fields oriented along the three principal target axes is a prerequisite for the model-based target parameterization. Such stimulation requires that we get a “look” at the target when it is more-or-less directly beneath the antenna array (vertical illumination) together with as many measurements as possible with the target laying closer to the edges of the transmitter antenna (horizontal illumination). The direction of the primary field as a function of position beneath a 1-m square transmitter antenna is illustrated in *Figure 3.4*.

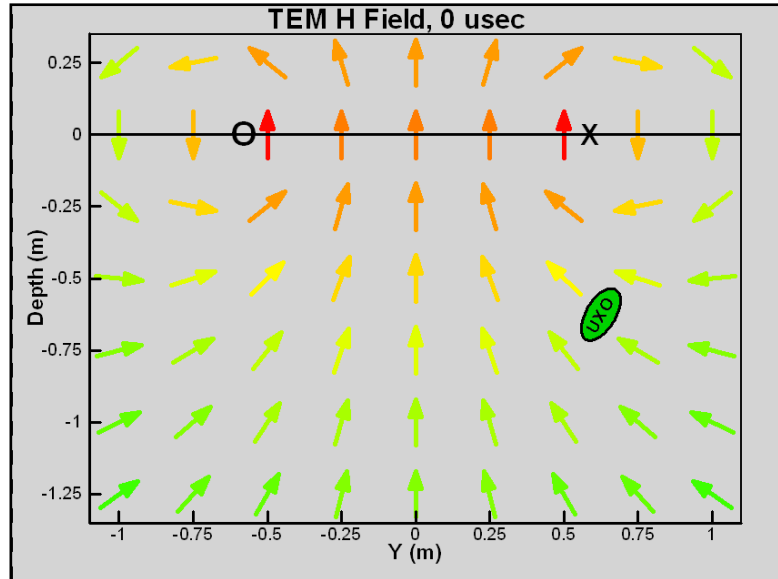


Figure 3.4: Primary field direction in the vertical plane through the center of a 1-m square transmitter coil. The O and X at Depth=0 indicate the position of the transmitter wire segments.

We maintained profile intervals during the course of surveying each of the sub-areas by physically marking the desired profile using either 100m or 60m survey ropes. A survey rope is similar to a long tape measure. Manufactured by Kesson, the survey ropes are made with nylon impregnated fiberglass. The metric ropes are graduated in units of 10 cm with a different marking at each meter. They are strong, easily dragged over rugged ground, and can withstand pulling and shaking when stretched to mark a straight line.

We marked the lanes with survey ropes at two-meter intervals as



Figure 3.5: Photograph of DNT survey operation underway at the Fort Ord ODDS site. The photograph shows the lane markers at 2-m intervals. For reference, the width of the transmitter antenna is 1 m.

illustrated in *Figure 3.5*. Using the ropes as guides along with the edges and center-line of our 1-meter wide DNT cart, we were able to survey a reasonably uniform set of profiles while only physically marking every 4th profile. *Figure 3.6* shows the station locations for our survey of the Aberdeen Calibration Lanes. The Calibration Lanes are located in a well-graded area so that these data admittedly represent the best-case scenario at Aberdeen in terms of uniform line coverage. Note also, that 4 to 5 profiles intersect the 1-m radius circles that have been centered over the location of each target. At ATC, DNT measurements at survey points falling outside of that 1-m circle exhibit little or no anomalous response. Therefore in our modeling, we gathered data points falling within a 1-m-radius of the target under investigation for our target analysis.¹⁶ Station locations over the entire area that we surveyed are shown in the *Appendix: OpenFieldTargets.pdf*.

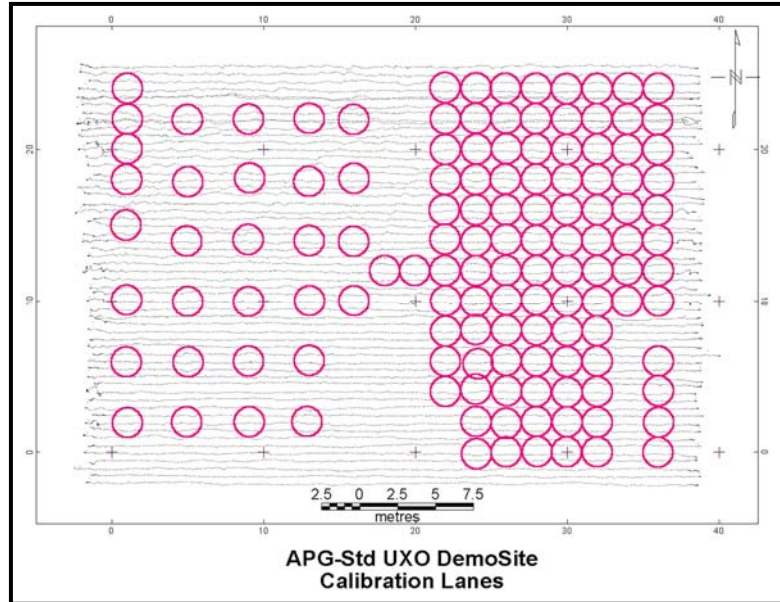


Figure 3.6: Figure showing line coverage over Calibration Lanes at Aberdeen. The circles have a radius of 1 m and they are centered on populated target cells. The figure illustrates how a lane density of ½-m will intersect a 2-m diameter target “foot print” with 4 to 5 lines.

The raw data files were processed daily using the initial processing steps outlined in *Section 2.3*. During that data compilation, we checked the data for timing latency and calibration using the periodic calibration ball profiles. For each of the sub-areas that we surveyed (e.g., the Calibration Lanes, *Figure 3.6*), we generated a color map together with the station coverage. The maps gave us a visual check of the lane coverage. When lanes were inadvertently skipped or when there was any other identifiable problem with the data, we fixed the problem and repeated the coverage. Although all of our problems were minor, we did have problems that forced us to repeat several small segments of the survey.

Data Quality Parameters and Indicators

DNT data quality is assessed both in real-time during field operations as well as from careful analysis of data using the *DNTreduce* program. Data precision, accuracy, completeness, plausibility, and repeatability are easily evaluated from a typical DNT dataset, as described in *Section 2.3.3*. Various experimental controls have been built in to our survey procedures that provide direct estimates of these quality parameters.

¹⁶ The radius of the data patches that we gather for target modeling is specified by the user. In the Calibration Lanes at ATC, many targets were buried on 2-m centers. For those targets, using a larger patch radius would produce data patches contaminated by as many as 3 adjacent targets. Very large and deep targets may have a larger footprint and in that case gathering data points from within a larger radius would be warranted.

Experimental Controls

Numerous experimental controls are built into our survey procedures. We checked the DNT system daily to verify proper operation at both the instrument level (i.e., NT-32^{II} transceiver) and at the system level. We performed start-up quality control (QC) every morning prior to survey operations that included GPS and NT-32^{II} battery, memory, and cable-shake tests, as well as a calibrator box response check for the NT-32^{II}. In addition, QC procedures referred to as “calibration runs” were performed before and after each data collection session (approximately 1-hour intervals) throughout the day. The calibration runs include instrument standardization, latency, and positional tests. We have found that implementing QC procedures in this fashion maximizes overall survey production efficiency for two reasons. First, we can identify potential instrument problems in the field and we can take corrective measures. Second, data processing is facilitated by having manageable-sized data sets which are bound by control data (calibration runs) at the start and end of every session.

Quality Control Procedures

Calibrator Box. During system start-up, prior to any production surveying for the day, we used a Calibrator Box containing a passive circuit composed of inductors, capacitors, and resistors (LRC) to verify that the receiver

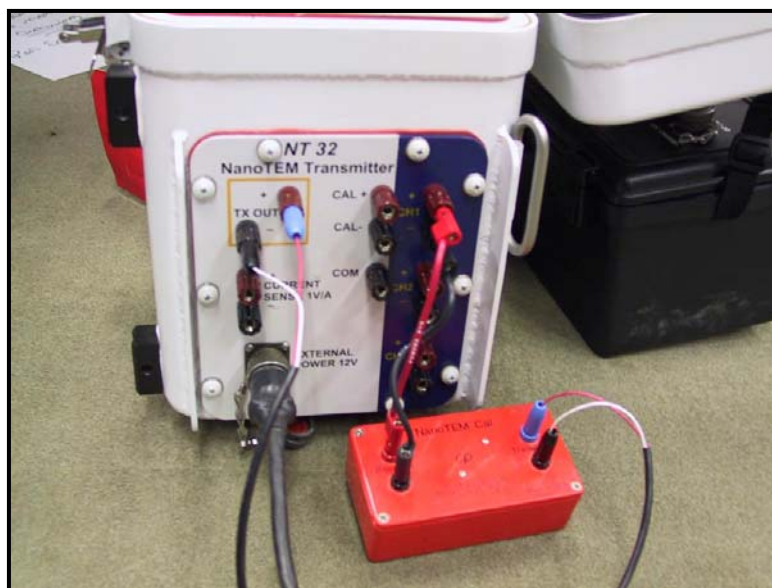


Figure 3.7: Photograph showing passive NT Calibrator circuit connected to the NT-32^{II} transceiver.

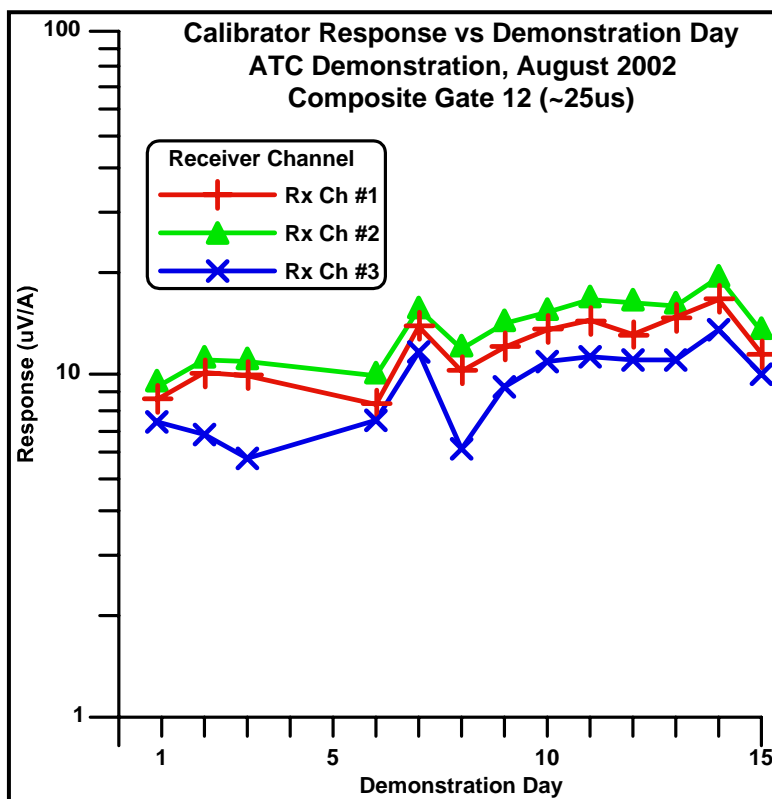


Figure 3.8: Calibrator response as a function of demonstration day for NanoTEM gate 12 (~25 us after current turn-off). The figure shows a systematic difference between the 3-channels in the early time response.

was operating satisfactorily. The Calibrator Box is driven by the transmitter and each receiver channel is connected to its output as illustrated in *Figure 3.7*. The calibrator was designed to generate a reproducible transient shape in early times and not to demonstrate instrument stability. We have, however, examined the Calibrator response for each of the survey days at Aberdeen. *Figure 3.8* is a plot of the calibrator response for NanoTEM gate 12 (i.e., $\sim 25 \mu\text{s}$) for each of the 3 NanoTEM analog channels as a function of survey day. The data show a variation in calibration response of approximately 8% over the period of the demonstration. The figure also illustrates that there is a measureable and systematic difference in the response for each of the channels. Laboratory experiments suggest that the systematic difference, observed only at early times, is a function of the proximity of the analog circuit board to the onboard transmitter. We believe that there are two causes for the apparent temporal variation of calibrator response:

1. The calibrator is a simple passive electrical circuit constructed from resistors and capacitors. In order to achieve a good early time response, the capacitors are necessarily very small (i.e., on the order of a few picoFarads). Day-to-day differences in the wiring hook-up as shown in *Figure 3.7* can account for some if not all of the variation shown in the figure.
2. The standardization tests that we routinely ran before and after each data recording session (see below) demonstrated to us that the NT-32 transmitter requires a warm-up period before its current waveform turn-off characteristics stabilize. The calibrator box was the first thing we did every day, so we believe that some of the variations seen in *Figure 3.8* are attributable to the fact that the transmitter was not allowed sufficient time to warm up. Typically, the calibrator recording lasted only 30-60 seconds. We have modified our field procedures so that calibrator measurement is several minutes long.

Calibration Run Procedure. At the beginning and end of each 1-hour recording period, we acquired DNT data over a 3-inch steel sphere. We staked out a short 15-20 m line and placed the test sphere at the center. Ideally, the test line should be oriented north-south or east-west. The test sphere target should be placed in a convenient location that may be easily accessed over the course of the entire survey. Our calibration run procedure requires that we dynamically survey (at normal survey pace) the test sphere line in one direction, turn around and survey the line in the opposite direction, then back up the cart until it rests directly over the target. At that point,

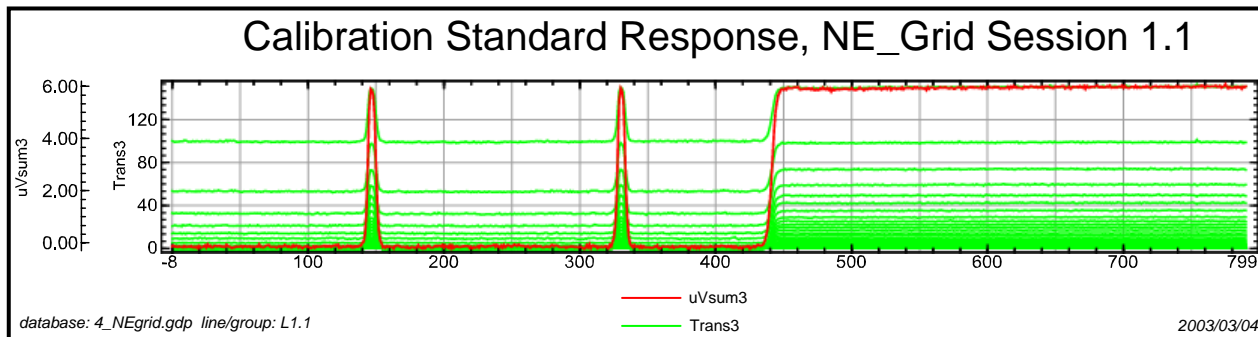


Figure 3.9. An example calibration run standard response plotted against time. The red profile is an Intermediate time composite gate for the vertical channel ($uVsum3 = \text{dBz}/dt$, windows 12-21), and the green profiles are the 31 channels of the complete vertical field transient. The first peak is generated by passing one direction over the test sphere, the second peak from passing over target in the opposite direction, and the plateau is from parking the cart directly over the target for a 30 second static occupation.

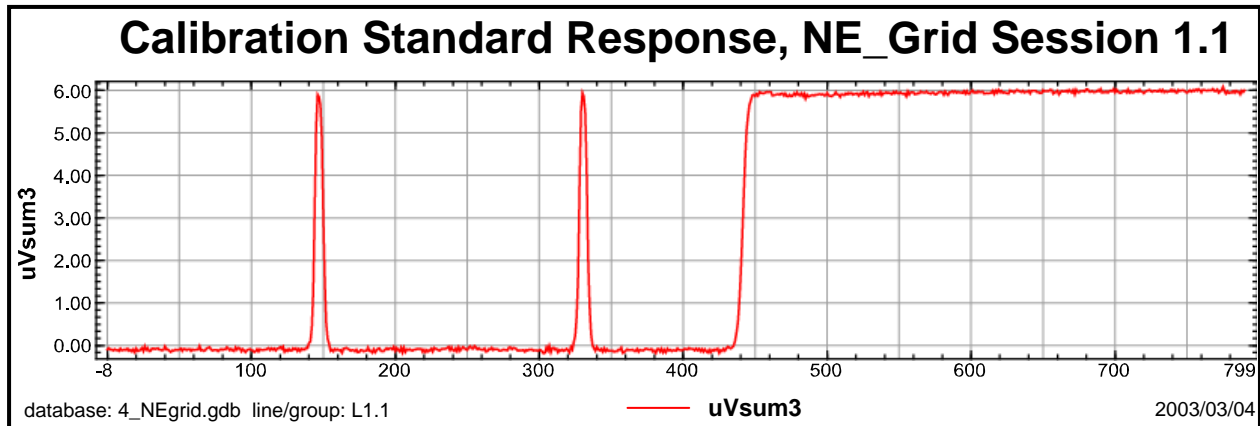


Figure 3.10. An example calibration run standard response plot for the vertical component, dBz/dt , composite windows 12-21 (uVsum3).

we stop and make a stationary recording for about 30 seconds. A typical calibration run line is shown in *Figure 3.9* and illustrates the characteristic “peak, peak, plateau” signal when viewed as a time series. In this figure, we have plotted both the Intermediate time composite gate for the vertical channel (uVsum3, red profile), and the 31 channels of the complete vertical field transient (green profiles). The two peaks represent the cart passing over the steel ball in opposite directions. The level shift at the end of the profile represents the point where the cart is halted directly over the steel ball. We also acquire a fixed point GPS station by averaging GPS solutions over the static 30 second stop period. During the calibration runs, the DNT operator makes visual checks of both EM and GPS data repeatability. The data acquired during the calibration runs are the basis for the standardization, latency, and positional tests discussed below.

Quality Control Indicators

Standardization Tests. A standardization test insures that the DNT data acquired over a known target with a known 'standard' response is repeatable within acceptable error limits. This is

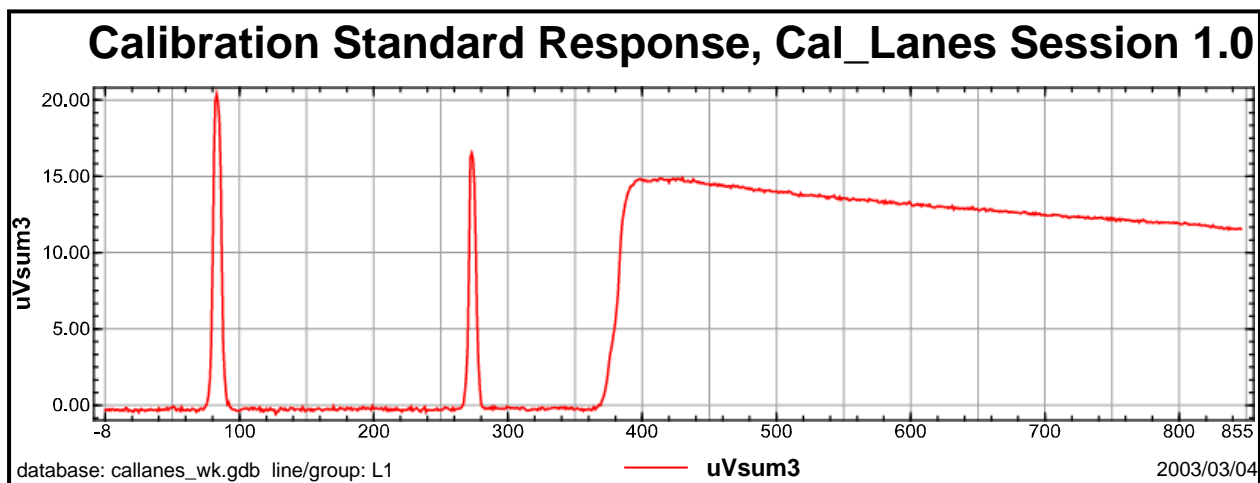


Figure 3.11. An example of unstable system response in DNT data from a calibration run made without sufficient system warm-up time. Uvsum3 is the vertical component, dBz/dt , composite windows 12-21.

necessary so that signals generated by unknown targets during a UXO survey are unbiased by random or systematic changes in internal system response. For example, for our DNT system, we require that the EM response from the calibration test sphere deviate by less than 10% from the established standard value. In the Appendix, *StandardTests.pdf* contains the calibration responses for the entire Aberdeen survey. The data includes the mean dBz/dt response and its standard deviation from the mean for composite window 12-21 for the test sphere. The mean and standard deviation are computed from the static data portions of each calibration run (the level shift, or 'plateau', in *Figure 3.10*).

We calculate a Percent Error by comparing the mean value to the defined standard value of 5.96 uV/am^2 . Most calibration measurements deviate from the standard by less than 5%. However, there are a few outliers where the errors exceed 10%. These outliers occur early in the Aberdeen survey when several calibration runs were conducted without sufficient system warm-up time (*Figure 3.11*). When we modified our survey procedures to include a mandatory system warm-up time of 5 minutes, the problem was effectively eliminated. *Figure 3.12* shows histograms of beginning and ending session calibration standard responses (outliers discussed above have been removed). Note that there is a small bias between the two populations; the ending session calibration responses are consistently lower in magnitude than the beginning session responses. This systematic drift in system response is on the order of 2% per hour, possibly suggestive of a temperature dependent phenomenon.

Latency Tests. For the DNT system, we define latency as the time difference between the recording of an EM transient measurement and the recording of the GPS position associated with the measurement. Latency effects can be problematic when merging real-time data that is acquired from multiple instruments on moving platforms. Precise clock synchronization minimizes the problem. Latency corrections are almost never necessary with the DNT system because of our precision crystal-driven real-time clock that is electronically set directly from a GPS receiver. However, we do test for variable latency effects at the beginning and end of each acquisition session by analyzing the calibration run data. In the unlikely event that one of the instrument clocks were to drift or shift, or if the operator were to improperly synchronize the clocks at start-up, then the latency tests provide the means to correct all DNT data acquired during the session.

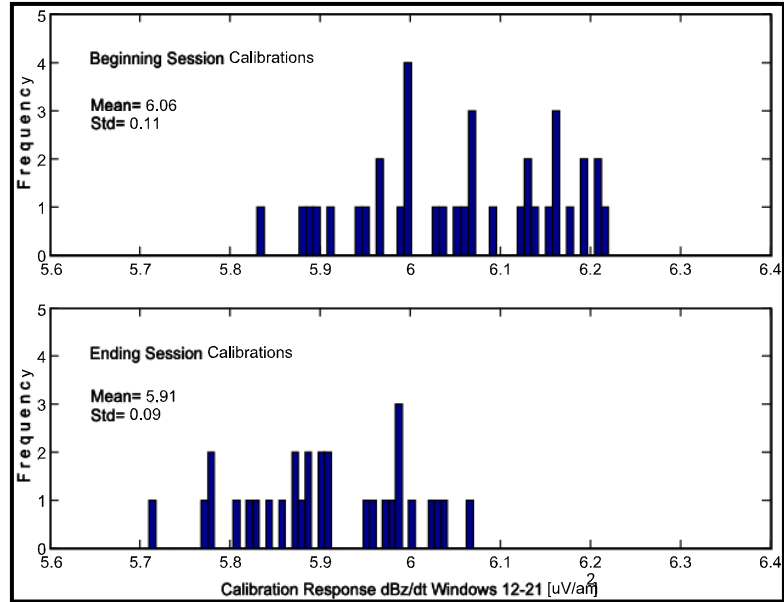


Figure 3.12. Standard response histograms for beginning session (top) and ending session (bottom) calibration runs from the Aberdeen DNT survey. Note that while the variances are similar, there is a small, about 2%, bias in the mean standard response for ending sessions compared to beginning sessions.

Our latency test involves plotting the data from the two passes over the calibration sphere. When the calibration run data are plotted as a function of distance along the profile line, the two target peaks must be aligned (*Figure 2.14*). A separation in the two peaks usually signifies that there is a time difference between the DNT data acquisition system and the GPS system that is unaccounted for. In this case, the two data streams would be re-merged using a computed latency correction that best aligns the target peaks.

Position Test. We perform a position test to verify that the GPS system is functioning properly and that it is generating coordinates in the appropriate reference system. At the end of each calibration run, we center the DNT system over the test sphere, acquire the static GPS coordinates, store them as a named station and check their values visually. We have provided a list of all of the static GPS position estimates for the calibration sphere in the file *PositionTests.pdf* in the Appendix. In the table, we define the Position Standard as the mean of all individual estimates of the test sphere's location (with the exception of two outliers that were most likely due to operator error (e.g., cart was moved while in static GPS mode)). The standard deviation of those 120 measurements is approximately 5 cm, and the standard error of the mean, which we define as the 'true' position, is about 0.5 cm. For our position tests, we require that the test measurement errors be < 0.5 ft, or 15 cm. The positional checks are all well within 15 cm of the Position Standard (with the exception of 2 outliers noted above).

Several factors affect the final resolution of target positions including the precision and accuracy of real-time GPS positions, the GPS data rate and instrument travel speed, and the resolution of data processing procedures for anomaly picking and target modeling. We can give an empirical estimate of anomaly position accuracy by evaluating data from the calibration runs. *Figure 3.13* is a map spanning a small region (about 60cm x 40cm) around the calibration target. The true location of the sphere is shown in black and the static GPS positions used to determine this solution are shown as green crosses. The red crosses are the 'dynamic' position estimates for the calibration target. Note that for both the static and dynamic estimates, the variance is greatest in the along track direction: in this case the calibration run track was oriented northwest-southeast. The dynamic position estimates (red) were generated by picking the peak of the target anomaly from the DNT data. The standard deviation of the dynamic estimates is 10 cm, about twice

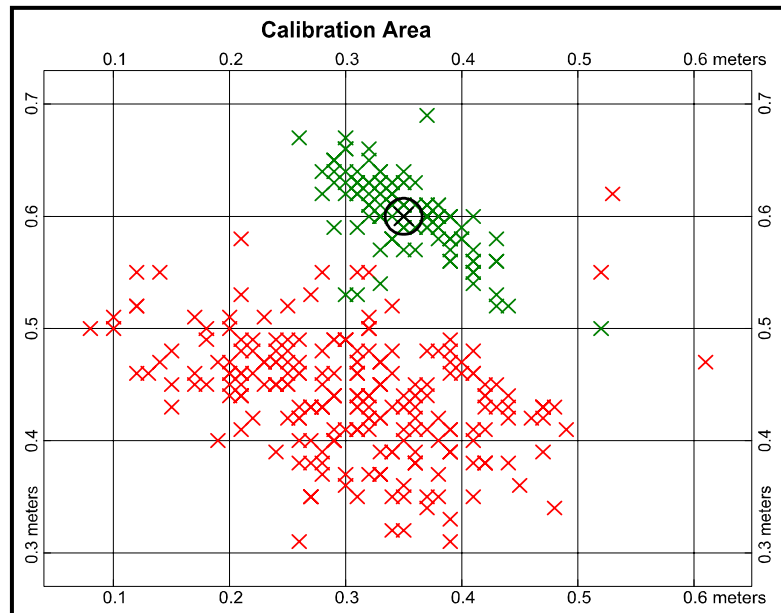


Figure 3.13. Static (green) and dynamic (red) GPS position estimates for the calibration target. The 'true' position (black circle) is the mean of 120 static occupations with a standard error of about 0.5cm. The dynamic position estimates are based on the calibration target peak anomaly location from the merged DNT data with a standard deviation of 10 cm. There is also approximately 19cm bias in the dynamic estimates.

that of the static estimates. Note also that there is clearly a bias in these two populations of approximately 19 cm. The bias is in the cross-track direction, and is the same for both northwest and southeast traverses.¹⁷

Data Completeness. Our sampling plan, discussed above, was designed to obtain 100% coverage of the survey area. In order to check for completeness of coverage, we post the data track using Oasis Montaj, and check for obvious missing lines, segments, or areas. In addition, the data from a standard composite window are gridded and displayed as a color-filled map using Oasis Montaj. A blanking distance of 0.5 m is chosen when gridding the data so that no data are shown which fall outside the footprint of the 1 m wide cart. In this way, line separations that exceed the 0.5 m specification can be seen on the color maps as gaps in color-fill.

Sample Analysis

We followed steps outlined in detail in *Section 2.3* for data processing and analysis. Using the ground truth provided to us for the calibration lanes, we were able to generate the detection ROC curve for our system shown in *Figure 3.14*. The curve was generated using targets picked by the Oasis Montaj grid-based peak picker. For this curve we gridded a composite time gate (NanoTEM gates 12 through 21 centered at $68 \mu\text{s}$) of the residual vertical field transient (dBw/dt). We compand (mathematically compress) the data using the function illustrated in *Figure 3.15*. The function \sinh^{-1} behaves logarithmically when the absolute value of its argument is greater than 1, and can be scaled to SNR in decibels. Its appeal is that, unlike the \log_{10} function, it can be applied to bipolar functions with both positive and negative values, such as horizontal TEM components. The ROC curve suggests that the optimum detection threshold is about 7dB ($0.12 \mu\text{V/A-m}^2$).

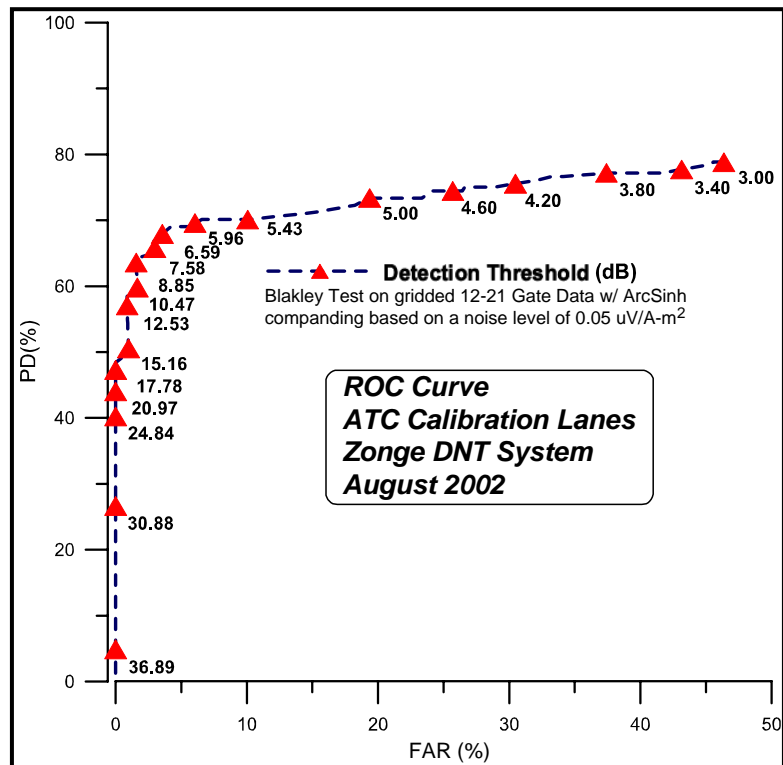


Figure 3.14: A receiver operation curve (ROC) for DNT data acquired over the Calibration Lanes at ATC. The knee of the curve, shown at about 7dB signifies that the optimum threshold of detection is at $0.12 \mu\text{V/A-m}^2$ where the RMS background noise level has been estimated to be at $0.05 \mu\text{V/A-m}^2$.

¹⁷ The cross-track bias is partly due to the offset of the GPS antenna from the cart reference point. *DNTreduce* corrects for this offset while static GPS positions are uncorrected. Another source of systematic error would be a small roll angle. A roll of just three degrees offsets the antenna by 5 cm.

Detection. We set the detection threshold at about 0.12-0.18 $\mu\text{V}/\text{A}\cdot\text{m}^2$, or about 2 to 3 times the RMS background noise level, and ran a grid-based peak detector on data grids generated from our intermediate time composite gate (i.e., sum of gates 12 through 21) of the vertical component DNT data. We visually examined each target anomaly using profile plots of the vertical component from the intermediate time gate used in the peak detection, and from an early time composite gate (5-10).

In Figure 3.16 we show profile plots over cell row J of the Blind

Test Grid. The profiles are for Early and Intermediate composite time gates of the vertical field DNT transient (dBw/dt). We show both a companded plot (top) and a linear plot (bottom). These plots illustrate the importance of the early time gates for use in detection because of their significantly better SNR. By examining these profiles in Oasis Montaj, we are able to add targets to our list that were not picked by the automatic peak pickers, and to reject targets that are more likely due to spurious noise in the intermediate time gate. This figure shows targets at locations J11, J17, and J19 that may have been missed by the automatic picker but are obvious in the Early-time composite gate.

Classification. To meet the requirements of the Classification phase of the demonstration, we parameterized each target by fitting the 4D anomalous data within a small area, typically a 1-m radius circle, around the identified target location. We have discussed our dipole modeling procedure in Section 2.3.6. In Section 2.3.7 we have discussed in detail the implications of many of these parameters for classifying targets. However, the application of determinant analysis for computing a *ranking metric* has been a recent development and the method was not used to prepare our target lists for ATC. At that time, our method for classifying targets involved a manual review of inversion modeling results from our *DNTDipole* program (Sections 2.3.6 and 2.3.7). For each target, an interpreter analyzed polarizability parameters from each of three inversion models (ellipsoid, spheroid and sphere) that were based on increasing symmetry constraints (e.g. Figures 2.19-2.21). Each interpreter classified a portion of the target list using shape-based criteria obtained from the polarizability plots. Using these model-generated parameters, two of us identified each target as **Ordnance (OE)** or **Clutter** (a binary classification scheme). We based our classification primarily on the shape characteristics of the polarizability plots together with the fit statistic (*NSR*). To be classified Ordnance, we required that the model exhibit an axis of symmetry, preferably with rod-like characteristics ($P01 > (P02=P03)$).¹⁸ We classified as Clutter those targets whose model either had no suggestion of

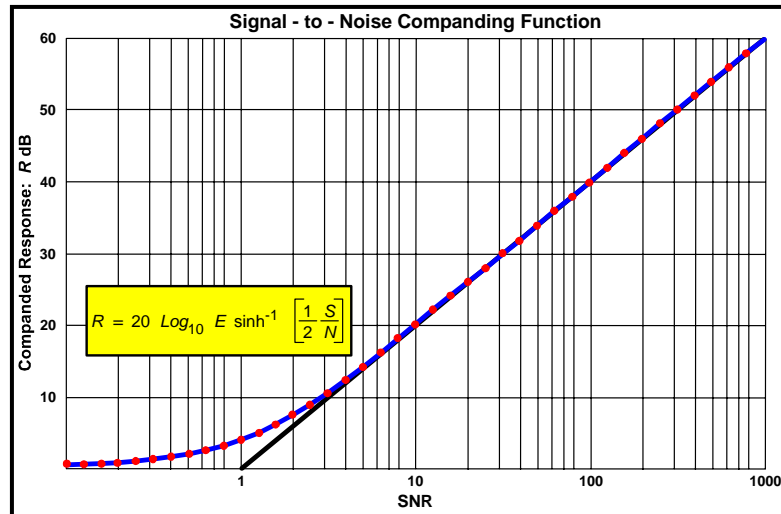


Figure 3.15: Function used to affect bipolar companding. When scaled as indicated in the formula, the function approximates the signal-to-noise ratio (SNR) expressed in dB for SNR>1.

¹⁸ The large anti-tank mines (T62) exhibit plate-like characteristics. Hence, we were reluctant to declare targets with definite plate-like symmetry as Clutter.

symmetry (e.g., three distinct and separate dP/dt curves for the Ellipsoidal model, large f -test value when viewing the Spheroidal model). We also classified as Clutter all targets whose parameterizations exhibited large NSR (i.e., $NSR > 80\%$), or unrealistic depths and total polarizability ($P0$). To meet the requirements for a monotonically increasing ranking metric that is suggestive of confidence level that a target is UXO, we used the formula

$$\begin{aligned} \text{If OE } P &= \frac{(100 - NSR)}{2} + 50 \\ \text{Else } P &= \frac{100 - NSR}{2} \end{aligned} \quad (3.1)$$

Since low NSR signified a good model fit, *Equation 3.1* maps targets classified as OE onto the interval $50 \leq P \leq 100$, with 50 being low confidence that the target is OE and 100 being high confidence. Similarly, targets classified as Clutter are mapped onto the interval $0 \leq P \leq 50$ where 0 corresponds to high confidence the target is Clutter. From *Equation 3.1* one can see that we used the model fit statistic (NSR) as a basis for expressing confidence in our choice with 50 percent as the threshold.

The third person involved in the classification of targets at Aberdeen used an interpretive ranking scheme based on the criteria shown in *Table 3.2*. The target rank (P) that we submitted with the target list was therefore a combination of the subjective interpretation rank R and an objective fit statistic NSR according to the formula

$$P = \frac{R + (100 - NSR)}{2} \quad (3.2)$$

In *Equation 3.2*, the rank value R expresses the interpreters level of confidence as suggested in *Table 3.2*. NSR is a percentage ranging from 0% (perfect fit) to 100% extremely poor fit. The

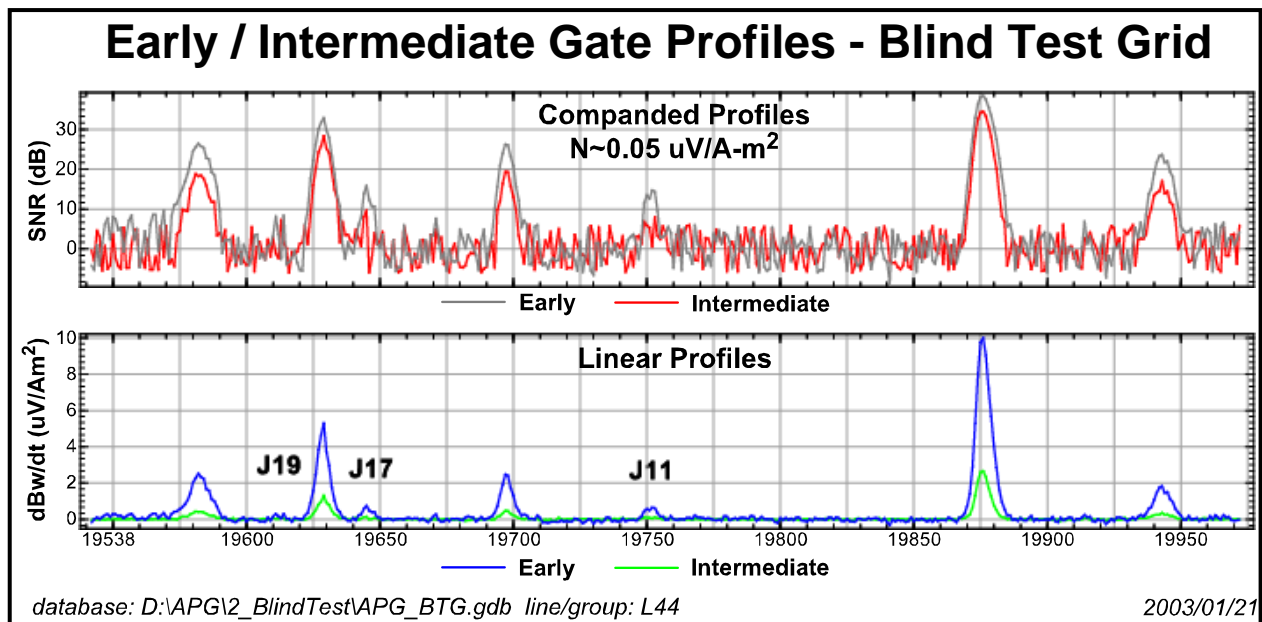


Figure 3.16: DNT profiles at Early (10 μs) and Intermediate (68 μs) time composite gates illustrate improved SNR at early times.

rank P for a target interpreted to be OE with high confidence ($R=80$) will be given a rank between 50 and 100 with the low value indicating a very poor model fit ($NSR > 80\%$) and the high value for a perfect fit ($NSR < 20\%$). If the interpreter classifies the target as Clutter, the target rank

is biased so that it falls between 0 (High Confidence) and 50 (Low confidence – could be OE). The scoring formula results in a scale ranging from 0 representing very high confidence that the target **is not** OE to 100 signifying very high confidence that the target **is** OE.

Table 3.2: Definitions of Interpretive Rank - Aberdeen

<i>Qualitative Rank Definition</i>	<i>Best Model Type:</i>	<i>DNTdipole Rank (R)#</i>
High probability UXO	Spheroid-Rod-like	80
Moderate probability UXO	Sphere	50
Low probability UXO	Spheroid-Plate-like or Ellipsoidal / amorphous	20
Clutter	Noise	5

Table 3.3: UXO Library Target Types - Aberdeen

TRG	NC	PK_1	PK_2	PK_3	PA_1	PA_2	PA_3	PB_1	PB_2	PB_3	PC_1	PC_2	PC_3
20mm	1	2.3	2.3	2.3	2	2	2	0.9	0.9	0.9	0.25	0.25	0.25
40mm	1	100	100	100	1	1	1	0.9	0.9	0.9	0	0	0
57mm	2	60	60	60	6	6	6	0.8	1.1	1.1	0.2	0.2	0.2
60mm	2	554.3	1269.3	1269.3	7.15	9.01	9.01	0.77	0.97	0.97	0.74	0.59	0.59
81mm	2	1087.9	1745.4	1745.4	9.42	8.66	8.66	0.87	1.03	1.03	0.53	0.37	0.37
90mm	2	1035.4	2375.6	2375.6	10.2	10.76	10.76	0.75	0.98	0.98	0.36	0.35	0.35
105mmH	2	9000	9000	9000	9	9	9	1	1.1	1.1	1.5	1.5	1.5
105mm	2	692.8	2219	2219	8.04	11.01	11.01	0.76	0.99	0.99	0.25	0.19	0.19
155mm	1	460	460	460	11	11	11	0.8	0.8	0.8	0.58	0.58	0.58
2.75R	2	1127.7	2901	2901	7.48	11.05	11.05	0.85	1.19	1.19	0.4	0.45	0.45
MK118	1	1	1	1	5	5	5	1	1	1	0.2	0.2	0.2
BLU26	1	7	7	7	5	5	5	0.7	0.7	0.7	3.5	3.5	3.5
BDU28	1	18	18	18	2.5	2.5	2.5	1	1	1	0.3	0.3	0.3
M42	1	2.3	2.3	2.3	4.3	4.3	4.3	0.6	0.6	0.6	2	2	2
Loop	2	12000	1.00E-05	1.00E-05	1	1	1	0	0	0	1	1	1
8#_SP	1	12000	12000	12000	23	23	23	2	2	2	6.80E-03	6.80E-03	6.80E-03
12#_SP	1	2200	2200	2200	20	20	20	1.4	1.4	1.4	15.8	15.8	15.8
16#_SP	1	22000	22000	22000	17	17	17	1.1	1.1	1.1	1.08	1.08	1.08
T16ATM	2	309	1.53E+03	1.53E+03	6.3	14	14	0.7	0.9	0.9	5.6	9.38	9.38

The final step in our classification was to run the set of targets that we classified as OE through a final pass of our modeling program *DNTDipole* together with a model library file containing a set of prototypical target items. With such a library, *DNTDipole* indicates the library item that best fits the target data. Table 3.3 shows the library of 19 prototype target items that were used for final target classification at Aberdeen. The 'NC' column is the number of components

defining target symmetry and the remaining columns are the theoretical Pasion model parameters (*Equation 2.4*). Note that the Pasion parameters given for each library UXO item were estimated from calibration data from both the Blossom Point and Aberdeen surveys.

3.6.7 Demobilization

All equipment was disassembled and packed in their shipping containers in less than 2 hours on Tuesday, September 3. We shipped the equipment back to our home office in Tucson, AZ directly from the Aberdeen Test Center. A few wooden stakes were used (with permission) during the early part of the demonstration. Midway through the demonstration, we were advised that the use of stakes would no longer be allowed. Thereafter, we used sandbags as a means of anchoring our survey ropes. A normal job would no doubt require some survey markings (e.g. flagging, paint marks, stakes). These, of course, would be removed at the end of a survey.

4. PERFORMANCE ASSESSMENT

4.1 PERFORMANCE CRITERIA

The ultimate objective of this ESTCP project is to demonstrate that the 4D fast TEM technology is better at both detection and discrimination than competing 1-D (EM-61) or 2-D (EM-63) TEM instruments commonly used for UXO site characterization. Performance must be judged, therefore, using metrics such as probability of detection P_d and probability of false alarms P_{fa} . These parameters apply equally to the detection phase as well as to discrimination phase of the interpretive process. We list in *Table 4.1* a set of performance criteria that the DNT system meets or exceeds. Most of these performance criteria have been tested during the course of our demonstration at Aberdeen. They are further buttressed by our experience at Blossom Point and at the former Fort Ord (not discussed here).

Table 4.1: Performance Criteria for DNT System

Performance Criteria	Description	Pri/Sec
Prob. of Detection (P_d) Detection Discrimination	# Detections/(# OE)	Primary
Prob. Of False Alarm (P_{fa}) Detection Discrimination	# non-OE Detected/# non-OE	Primary
Factors Affecting Perf	Weather Conditions Terrain / Topography	Secondary
Ease Of Use	Crew Size / Training	Secondary
Reliability	Down-Time	Primary
Versatility	Adaptable to a broad range of high resolution shallow exploration problems	Primary
Maintenance	Low-Maintenance – field technician level	Secondary

4.2 PERFORMANCE CONFIRMATION METHODS

Based on demonstrations we have conducted at Blossom Point and at Fort Ord where we had access to the ground truth, we believe that the DNT system has a P_d that is comparable to that of the ubiquitous EM-61. Analyses from our Blossom Point demonstration [17], for example, showed that the DNT system has a sensitivity that is nearly equivalent to that of the man-portable MTADs system that is based on a modified EM-61. We anticipate therefore that our performance scores in the detection phase will be comparable to surveys run with that instrument.

A good score on discrimination is largely dependent on the interpretive experience of the scientists and technicians involved. An important objective of this ESTCP project has been to demonstrate that we are able not only to efficiently acquire DNT data but that we also have developed software tools that permit us to utilize these data for interpretation. We have developed state-of-the-art modeling tools that are able to utilize the full dimensionality of the data that we acquire (i.e., time, and 3 orthogonal vector components). Therefore, our ability to perform effective discrimination provides testament not only to the analytical methods that we

have developed (e.g., *DNTDipole*) but also to the fact that we have progressed in our ability to interpret the results of our data processing and computer analyses. *Table 4.2* is a tabulation of the primary performance criteria, our expected pre-demo performance metric, and the actual performance scores returned to us by the scoring committee for the Aberdeen Standardized UXO Technology Demonstration Site.

Table 4.2: Expected Performance and Performance Confirmation Methods

Performance Criteria	Expected Performance Metric	Performance Confirmation Method	Actual Performance (post demo)
Response Stage			
P _d	> 90%	Government Evaluation	80%
P _{fa}	> 90%		90%
Bkg Alarms			50%
Discrimination Stage			
P _d	?	Government Evaluation	45%
P _{fa}	?		50%
Bkg Alarms	?		0
Efficiency	?		46%
Rejection Ratio	?		51%
Reliability	< 10% down time	Survey Statistics	13 hr (~10%)
Ease of Use	3-man crew (1 professional)	Demonstrations	3-man

4.3 DATA ANALYSIS, INTERPRETATION, AND EVALUATION

The utility of a multi-component TEM system lies in its ability not only to detect an anomaly but also in its ability to make use of the added dimensionality of the resulting data set to better characterize any targets that are detected. We base our target characterization on analysis of anomalous data patches using a point dipole model. That analysis has been explained in detail in *Section 2.3.6*. The efficacy of that analysis depends on many factors among which are: the number of sample points that fall within the anomaly footprint (typically within a radius of approximately 1 m), the quality of the positioning information, and the overall amplitude of the anomaly. Adequate characterization of target anomalies is critically dependent on the number and overall quality of the data points falling within a small radius of the target center which is, in turn, affected by both survey speed and line spacing. With a base sample rate of 32 samples/sec, subsequently reduced by filtering and decimation to 8 samples/sec, the only impediment to survey speed at Aberdeen were the physical demands placed on the operator to move the cart at normal walking speeds. Our maximum survey speed never exceeded 1 m/sec and, therefore, the sample interval along a survey line was never more than 12 cm and was generally about 8 cm. Lane spacing is therefore the critical parameter that guarantees that each target anomaly is not only adequately sampled in the direction transverse to the lanes but also has been adequately illuminated by a horizontal primary field from the transmitter loop as it passes the target along a lane that is laterally offset to the right or left from the target (*Figure 3.4*). With a ½-m lane spacing, we are usually guaranteed that there are a minimum of 3 lines that pass through the

anomaly footprint and that the resulting transient data represents the illumination of the target from all directions.

Our operational and data analysis requirements are very similar to those described in connection with the EMMS system developed at the Naval Research Laboratory [27, 38]. We believe, therefore, that it is appropriate that the baseline system against which the DNT system can be compared is NRL's EMMS based on the Geonics EM61 MkII.¹⁹ The NRL reports that they have found that they obtain significantly better target classifications with their "**3- β** " analysis when they use data derived from two surveys run with orthogonal lanes [39]. We agree with this assessment since it effectively doubles the number of data points that fall within the target footprint. However, for budgetary reasons we were constrained to survey the Standard Site at ATC in a single direction.

As we indicated in *Section 3*, our demonstration at Aberdeen included DNT surveys over 3 pre-defined areas, the Calibration Lanes, the Blind Test Grid, and the Open Field Area. Ground truth is available to us only for the Calibration Lanes. In the remainder of this section, we will discuss our analysis of data that we acquired in the Calibration Lanes and how we applied that information together with other calibration data obtained at Blossom Point (*Section 2.3.7*) to classify and rank targets in the Blind Test Grid. Although we use the same target list, the target classification and rank that we present here for the Blind Test Grid are different from those we submitted in early October to Aberdeen for scoring. These revised classifications and ranks represent an effort on our part to incorporate not only a better understanding of the requirements for a **ranking metric** but also an improved ability on our part to exploit **DNTDipole** model-parameter characterization for target classification.

4.3.1 The Calibration Lanes

In *Section 3*, we used a color map of the Calibration Lanes during our discussion of the demonstration start-up (*Figure 3.2*). It will be necessary to refer to that figure for this discussion of our analysis and interpretation of the DNT data from the Calibration Lanes at Aberdeen. The cell numbering convention for the Calibration Lanes is illustrated in *Figure 4.1*. Rows are numbered from A through M starting on the north side and proceeding southward (Right to Left). Columns are numbered starting on the east side and proceeding westward (Top to Bottom). To further facilitate our discussion, we have placed a circle with a 1-m radius over the center of each cell containing a target. Each circle has also been annotated with an abbreviated description of the target. For a more complete target description, the reader is advised to consult the file *ATC Calibration Lanes.pdf* in the Appendix. That spreadsheet contains a detailed description of the target (e.g., "20mm M55"), coordinates for its position, and its attitude angles (azimuth and pitch).

¹⁹ The EM63 is also a system with characteristics similar to the DNT system. We invite their comparison. However, at present we have available a data set acquired at Blossom Point with a very early version of the EM63. To our knowledge, there are as yet no other data available that we can use for comparisons.

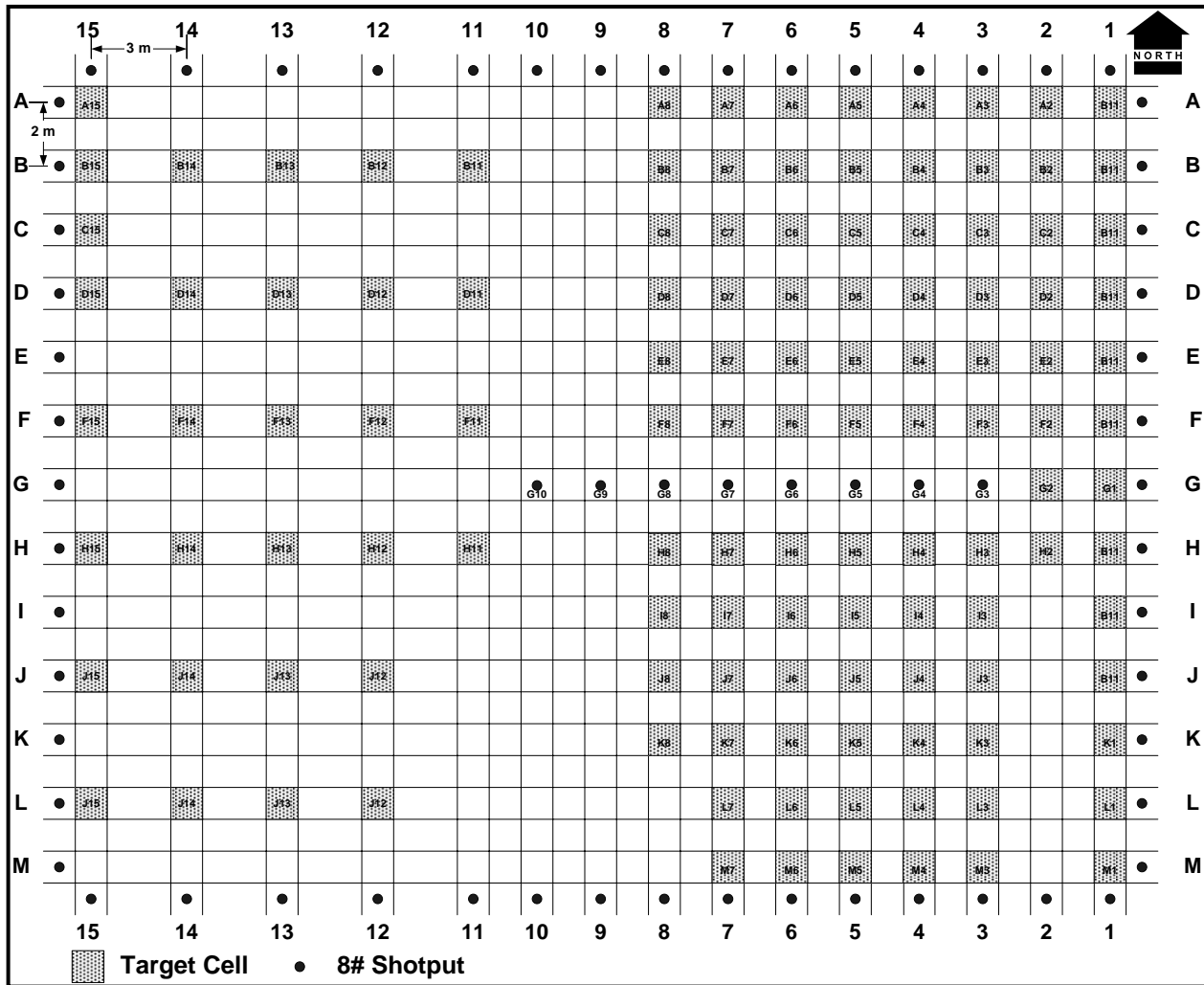


Figure 4.1: Figure showing the cell numbering convention in the Calibration Lanes at ATC.

Target Detectability

A cursory study of *Figure 3.2* indicates that many of the targets have very low signal-to-noise ratio (SNR). Indeed, there are 12 cells with targets (i.e., those with 1-m circles in *Figure 3.2*) that exhibit no detectable anomaly, at least not from a map of the intermediate composite time gate. Clearly, the Calibration Lanes were designed primarily for the purpose of testing a system's ability to detect the target. There are 17 target types in the Calibration Lanes that have been placed at more than one depth and/or attitude. Therefore, by tabulating whether or not we detected a target at a particular depth provides, in a tabular form, a qualitative measure of system performance by which our system may be judged against other systems. In *Table 4.3*, we have tabulated the detectability of each of the 17 targets in the Calibration Lanes that were buried at more than one depth. To give the reader a sense of the target-anomaly amplitude, we also tabulate the average observed anomaly SNR for the vertical field dBw/dt, expressed in dB, for each target. In compiling this table, we used the intermediate composite time gate (channels 12-21 centered at 68 μ s) for detection and measured our SNR relative to the RMS noise value of 0.05 μ V/A-m², a value that is consistent with the background noise for that composite channel.

Our table does not include the Loop targets in Lanes 1 or 2 because they were all placed at the same depth. Nor does it include the mine targets in Lane 15 for the same reason.

In *Table 4.3*, the SNR values represent the average anomaly SNR for all the targets at the same depth. We deemed a target as “detectable” at the indicated depth provided that it can clearly be seen on the map for all the attitudes represented.²⁰ Where a target

detection is deemed questionable, we placed a “?” in the box. Questionable detections occur at low SNR (generally < 6 dB) and indicate that at one or more attitudes the target did not produce a recognizable anomaly in the detection gate. The table shows that many of the target types are at or near the limit of detection for the DNT system. We consider the target depths in *Table 4.3* with SNR values at or around 5-8 dB as the maximum depth at which those targets can be detected. For those targets generating a larger anomaly SNR, we have estimated a depth at which the SNR would be at a just detectable level²¹ so that we arrive at a maximum depth of detection for each target. These values are summarized for the DNT system in *Figure 4.2*.

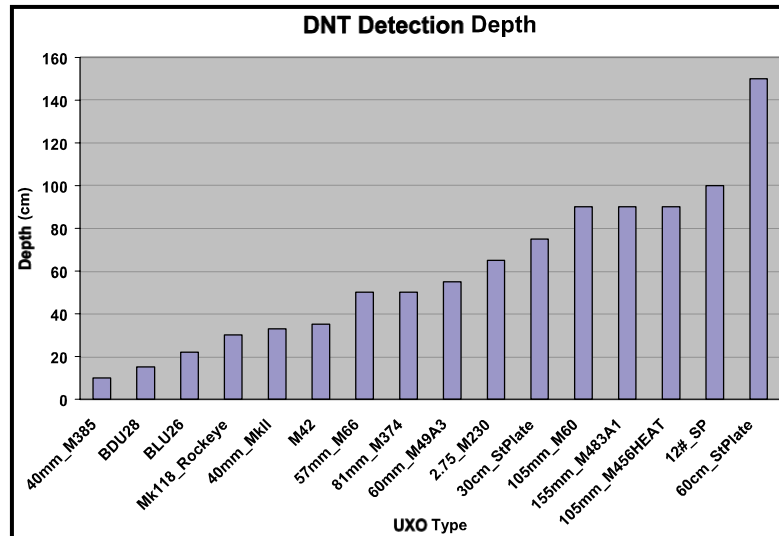


Figure 4.2: Figure summarizing the maximum DNT detection depth for targets in the Calibration Lanes at ATC.

Target Parameterization

Figure 3.2 together with the SNR values tabulated in *Table 4.3* show that the great majority of the targets in the Calibration lanes have anomaly SNR values that are far too low for reliable model parameterization. Compounding the problem is that the Calibration Lanes were built with the boundary shotputs placed a distance of 1 m from the adjacent target cell. It is clear that the placement of the boundary shotputs was a mistake by the field party that constructed both the Calibration Lanes and the Blind Test grid. Documents transmitted to us by ATC show that the Calibration Lanes were designed so that the boundary shotputs were located at a distance of 2 m from the nearest target cell. We communicated the problem to George Robitaille (Standard Test Site Principal Investigator) and the shotputs were immediately moved to their design locations. Unfortunately, that was after we had demobilized from the site. As a result, all targets located in rows A and M, and in columns 1 and 15 (33 targets in all) are contaminated with the anomalous response from an adjacent 8 lb shotput.

²⁰ For the smaller targets there were usually 4 targets with pitches at $\pm 45^\circ$ and $\pm 90^\circ$, respectively, located at the shallow depth. At the deeper depth, there were 2 targets at 0° pitch with azimuths at 0° and 90° , respectively.

²¹ We attenuated the SNR by 23dB for a doubling of the target depth (slightly greater than z^{-4}). This factor agrees with observed attenuations when we can measure anomaly SNR for targets at two depths, as for example with the 60 cm Steel Plate at 50 cm and 100 cm depth.

Table 4.3: Target detectability based on DNT survey results over the Calibration Lanes at Aberdeen.

Target Type	Depth (cm)	SNR (dB)	Detectable?	Comment
20mm_M55	10	7	Yes	
20mm_M55	20	5	?	Azimuth Dependent
40mm_MkII	30	11	Yes	
40mm_MkII	60	6	?	Azimuth Dependent
40mm_M385	10	6	Yes	
40mm_M385	30	2.5	?	Azimuth Dependent
M42	15	8	Yes	
M42	35	5	Yes	
BDU28	10	21	Yes	
BDU28	20	5	Yes	
BLU26	10	15	Yes	
BLU26	20	11	Yes	
57mm_M66	40	12	Yes	
57mm_M66	91		No	
Mk118_Rockeye	30	5	Yes (?)	Nose-up/Nose-dn Dep
Mk118_Rockeye	60		No	
81mm_M374	50	6	Yes	
81mm_M374	150		No	
60mm_M49A3	50	11	Yes	
60mm_M49A3	100		No	
2.75_M230	50	17	Yes	
2.75_M230	120		No	
30cm_StPlate	50	23	Yes	
30cm_StPlate	100		No	
60cm_StPlate	50	45	Yes	
60cm_StPlate	100	22	Yes	
105mm_M456HEAT	40	22	Yes	
105mm_M456HEAT	80	14	Yes	
105mm_M60	90	7	Yes	
105mm_M60	180		No	
155mm_M483A1	90	8	Yes	Highly Attitude Dependent
155mm_M483A1	200		No	
12#_SP	50	16	Yes	
12#_SP	100		Yes	Shot Put Interference
12#_SP	150		No	
12#_SP	200		No	

Fortunately, however, there are a number of targets that have sufficiently large anomaly SNR and are separated by 2 m or more from adjacent targets so that we obtained good dipole model results. Targets worthy of discussion include the following:

- The 18 ga and 20 ga shorted wire loops buried in cells B-2 through F-2.
- The 60mm mortars buried in cells H-8 through K-8
- The 30 cm and 60 cm steel plates buried in cells B-11, F-11, and H-11

- The 8 lb boundary shotputs that are buried everywhere. In particular, shotputs along the south boundary Lanes 8-15 and along the north boundary, Lanes 9-15 are all at least 2 m away from the nearest target cell. Those anomalies plus a few more along the west boundary form a good statistical population for the characterization of the 8 lb shotput.

Shorted Loops. Lane 2, cells B-2 through F-2 contains a series of shorted single-turn 15-cm and 30-cm diameter wire loops made with 18 and 20 ga wire (*Figure 3.2*). The theory for the TEM response of shorted loops is presented in Grant and West [28]. They show that the transient waveform is a simple exponential decay with a time-constant $\tau = L/R$ where L is the self-inductance of the loop and R is the loop resistance. A relation for the self-inductance of a single-turn circular loop is given in Smythe [40]. For copper wire imbedded in a non-permeable host medium, the inductance of the loop can be computed by the formula

$$L = \mu_0 \frac{D}{2} \left(\ln \frac{8D}{d} - \frac{7}{4} \right) \dots\dots\dots (4.1)$$

where D = Diameter of the loop,

d = Diameter of wire, and

μ_0 = Magnetic permeability of free space ($4\pi \cdot 10^{-7}$ h/m)

The polarizability magnitude (P_0) of the loop is derived by recalling that a loop carrying a current I behaves like a dipole perpendicular to the plane of the loop whose moment is the product of the current and loop area ($M = \pi d^2 I / 4$). It then follows from mathematics presented in *Section 2.3.6* that $P_0 = M/H$, where H is the source magnetic field component perpendicular to the plane of the loop. Using the classic development for the coupled loops [28, 41], we find the relation

$$P_0 = \mu_0 \frac{\pi^2 D^4}{16L} \dots\dots\dots (4.2)$$

A dimensional analysis of *Equation 4.2* shows that it does have the dimensions of length cubed which is consistent with our definition of polarizability.

We used a table from The Radio Amateur's Handbook [42] together with the previously cited relations for the self-inductance to compute the expected polarization magnitude P_0 , and corresponding time constants for the wire loops in the Calibration Lanes. We tabulate those values in *Table 4.4*.

Table 4.4: Table showing theoretical and observed time constants (tau) and polarizability magnitude (P0) for wire loop targets in the Calibration Lanes at ATC.

Loop D (cm)	Cell	Wire Gage	Wire d (mils)	Wire R (Ohm/Kft)	Loop_L (uh)	Loop_R (mOhm)	Comp_Tau (us)	SNR (dB)	NSR (%)	Obs_Tau (us)	Comp_P0 (cm^3)	Obs_P0 (cm^3)
30		12	80.8	1.619	1.00	5.01	200				6268	
		16	50.8	4.094	1.09	12.66	86				5765	
		18	40.3	6.510	1.13	20.13	56				5543	
	E-2	20	32.0	10.350	1.18	32.00	37	36	65	32	5338	2714
15		12	80.8	1.619	0.44	2.50	174				901	
		16	50.8	4.094	0.48	6.33	76				819	
	C-2	18	40.3	6.510	0.50	10.06	50	26	69	49	783	738
		20	32.0	10.350	0.52	16.00	33				751	

[illegible]

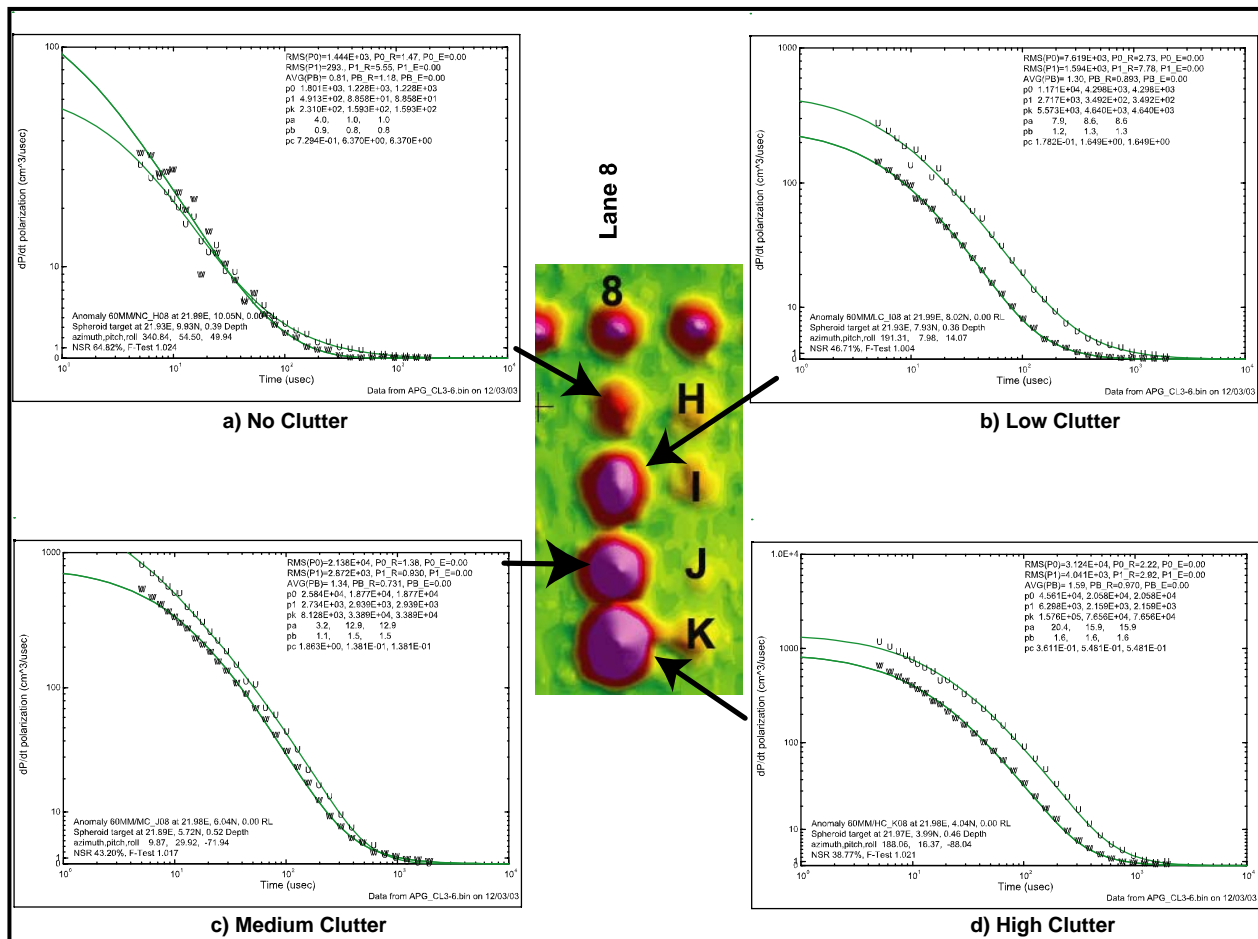


Figure 4.4: Polarizability plots for clutter-masked 60mm targets at the Calibration Lanes of the Standardized Test Site at ATC.

The color intensity map (*Figures 3.2 and 4.3*) shows two types of anomaly signatures generated by the wire loops. The first type (cells A-2, C-2, E-2, and G-2) is characterized by a single peak signature and is caused by a horizontal loop. The second anomaly type (cells B-2, D-2, F-2, and H-2) exhibits a double-peaked signature with the two peaks displaced in the east-west direction. This type of anomaly is produced by a vertical loop that is oriented north-south and centered at the same depth as the horizontal loops. For reference, the target description and attitude of the 8 loop targets in Lane 2 of the Calibration Lanes at ATC are tabulated in *Table 4.5*. In the table we also tabulated the SNR scaled off of *Figure 3.2*, the NSR, polarizability magnitude (P_0), Pasion b , and time constant (Tau) for associated *DNTDipole* modeling solutions. We have highlighted the target cells containing horizontal loops since these targets have on the order of 15-20 dB better SNR than the corresponding vertical loops (SNR column of *Table 4.4*). We were able to get reasonably good model solutions for the horizontal loops. For comparison with their corresponding theoretical values, we have inserted into *Table 4.4* the modeled results for targets C2 and E-2 (see highlighted lines). We also show the polarizability plots that were generated by *DNTDipole* in *Figure 4.3*. When the SNR of the anomaly is greater than 20dB, the model results compare quite favorably with the theoretical results. Even at marginal signal levels (for example targets B-2 and F-2), the estimated time constants are consistent with theory. In two cases (targets A-2, and H-2) the Pasion parameterization prefers to fit the curve with a

large power-law decay parameter (Pasion b) rather than a time constant (Pasion $1/c$). That is acceptable, however, since in either case (i.e., large Pasion b or small Pasion $1/c$) the parameterization tags the anomaly as having an anomalously rapid decay rate and so is an indicator of low permeability. Our modeling software does not do as well with the estimation of P_0 at low (i.e. ≤ 20 dB) anomaly SNR.

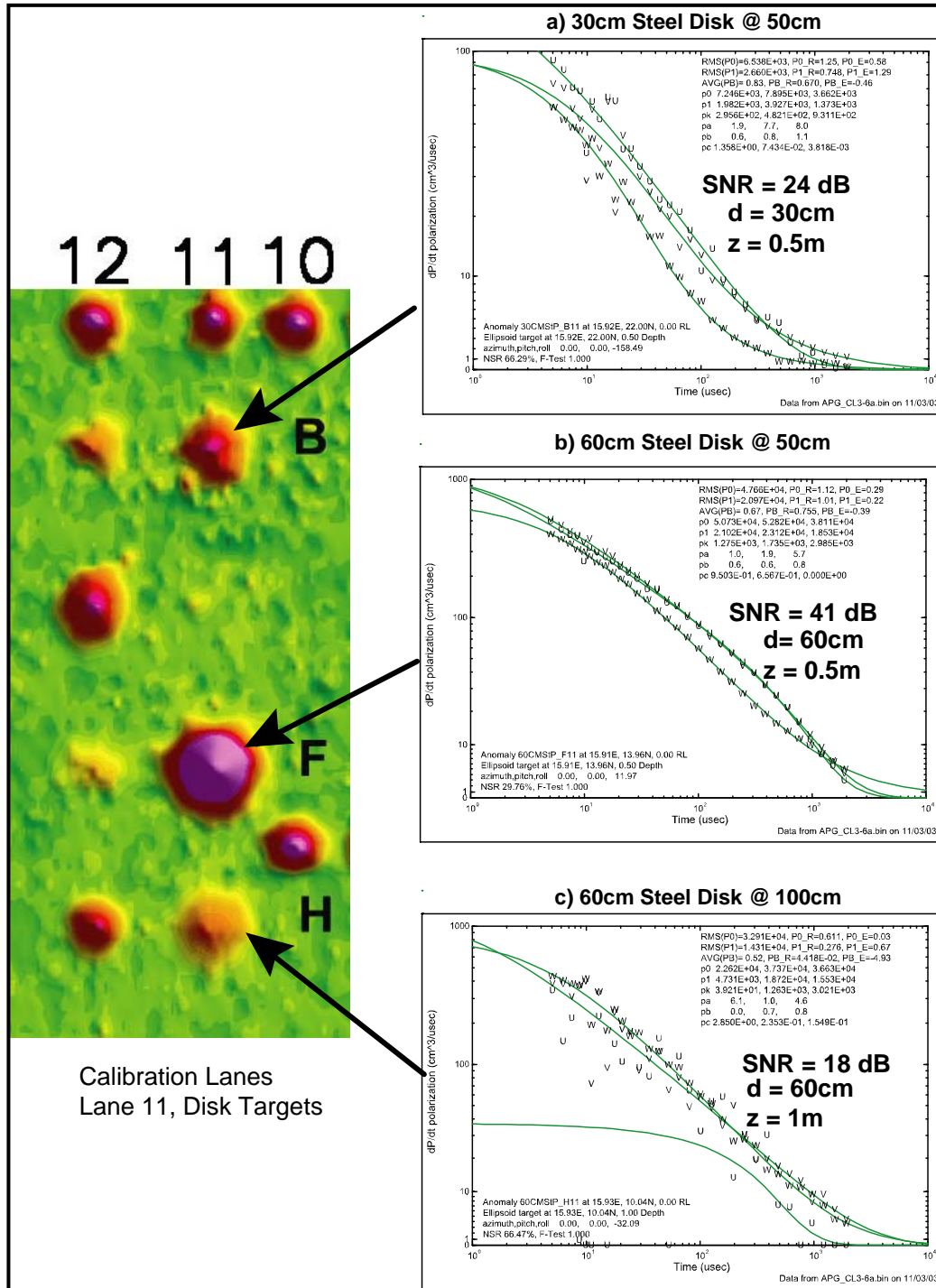


Figure 4.5: Polarization plots for the steel disks located in Cells B-11, F-11, and H-11 at the west end of the Calibration Lanes, ATC Standardized UXO Demonstration Test Site

Clutter-Screened 60mm Mortar Targets. Figure 4.4 shows polarizability model plots for the four targets H-8 through K-8. Each of these targets is a 60mm M49A3 mortar surrounded with varying degrees of clutter. The mortar round has been buried at 25cm in a horizontal attitude pointing north. The target polarizability transients for the target with no clutter (Figure 4.4a) indicate a target with an axis of symmetry, in fact almost spherical symmetry at a depth of 39 cm. Only at late times do the results suggest a rod-like shape. As the clutter level increases, model polarizability increases. Depth estimates for the medium clutter and high clutter targets (Figures 4.4c and 4.4d) are marginally greater by 10-15 cm. Regardless of the clutter level, modeling indicates bodies of revolution with varying degrees of rod-like behavior and therefore we would have classified them as OE with high probability.

Steel Disks. There are 3 detectable steel disks in Lane 11 (Target Cells B-11, F-11, and H-11). These cells contain flat-laying steel disks with diameters of 30 cm and 60 cm as annotated on Figure 4.5. The figure also shows the polarization plots (Ellipsoidal model) for the three targets. The model results clearly exhibit plate-like behavior even though the model has no cylindrical symmetry constraints. Moreover, SNR annotations for the three anomaly amplitudes again show that the modeling algorithm can produce useful results even at signal levels that are less than 10 times the noise floor. When we have a very large SNR, as we have with target F-11, the plate-like symmetry is so clear that the polarization transients look almost synthetic.

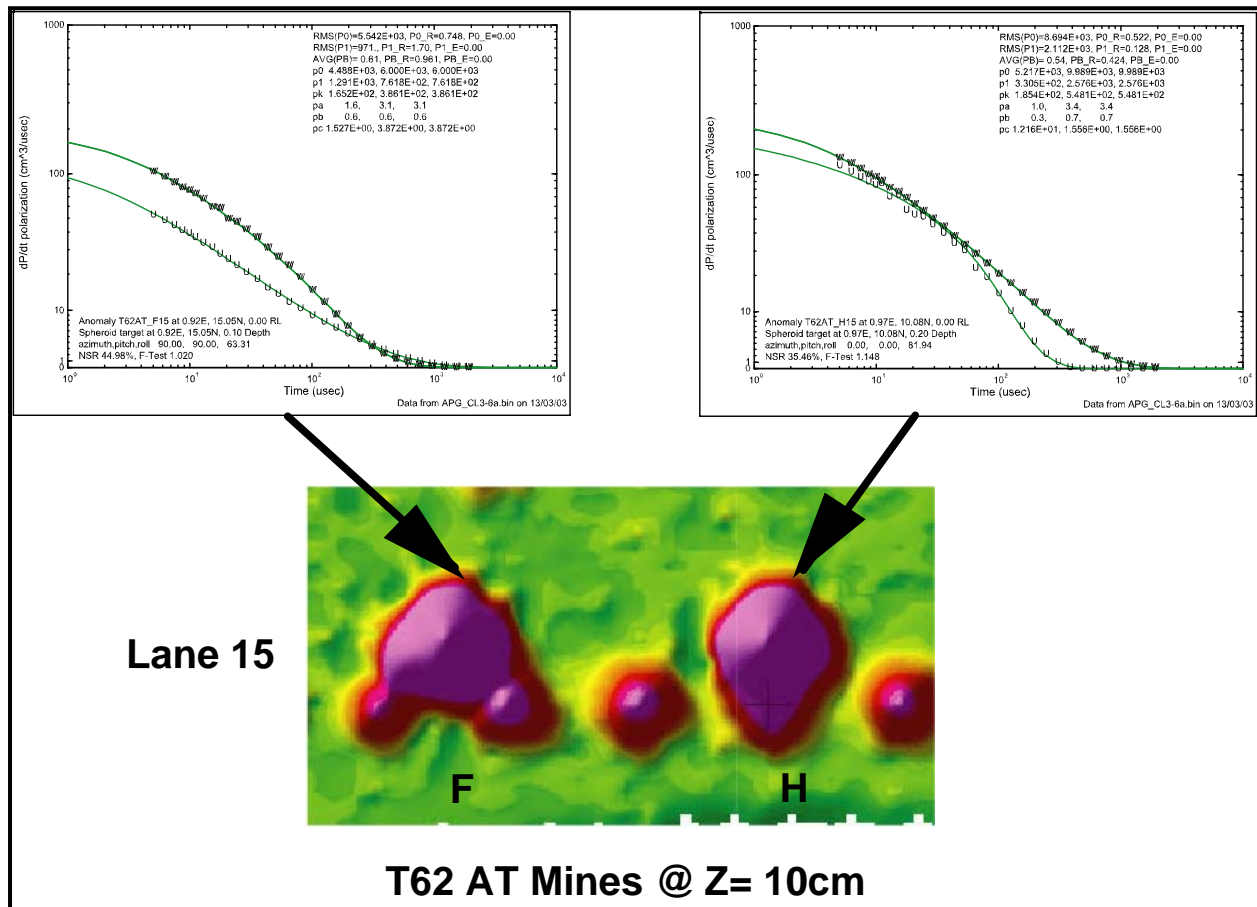


Figure 4.6: Polarization plots for the T62 AT Mines located in Cells F-15 and H-15 at the west end of the Calibration Lanes, ATC Standardized UXO Demonstration Test Site

T62 Anti-Tank Mines. In *Figure 4.6*, we show polarization plots for the two large T62 anti-tank mines located at the west end of the Calibration Lanes. These targets have huge SNR ($\sim 50\text{dB}$) and therefore model particularly well. We show these modeling results to illustrate how the target polarizability exhibits different shape behavior at different times during the transient decay process, and also how nominally identical targets at identical depths and attitudes can generate modeled responses that are remarkably different when data are distorted by overlapping anomalies. Both targets have roughly identical polarizability magnitude parameters, P_0 and both exhibit plate-like behavior over much of the 2 ms decay time shown in the plots. However, target F-15 starts out exhibiting very strong plate-like behavior (as manifested by the ratio of the longitudinal to transverse P_0 's) at early and middle time. At late time, the target looks quite isotropic (i.e., like a sphere). In contrast, target H-15 is nearly isotropic at early and middle times and becomes strongly rod-like at late times. This behavior is typical of many larger Calibration Lane targets. It is probable that the different characteristics are caused by varying degrees of contamination of data patches by the response from nearby boundary shotputs.

8 lb Shotputs. If the Calibration Lanes have nothing else, they have 8 lb shotputs! There are 56 shotputs marking the end points of the rows and columns and another 8 in row G (lanes 3-10). All these shotputs are nominally at the same depth (0.2 m to their tops). Forty-nine (49) of the 64 shotputs are at least 2 m away from the nearest occupied target cell, or the adjacent target was small enough that it does not seriously distort the EM anomaly. These target spheres, therefore, provide us a sample population of presumably identical targets with which to test our modeling algorithms. An important question that we have yet to directly address is how well our modeling estimates target depth. Using the test population of 49 8-lb shotput anomalies, we have compiled the statistics for the depth (z) and P_0 magnitude estimates for the 49 spheres. These data are displayed in *Figure 4.7* as histograms. The figure shows that we estimate that the spheres have a mean depth of 29 cm with a standard deviation of 4 cm. Likewise, the estimates on P_0 are

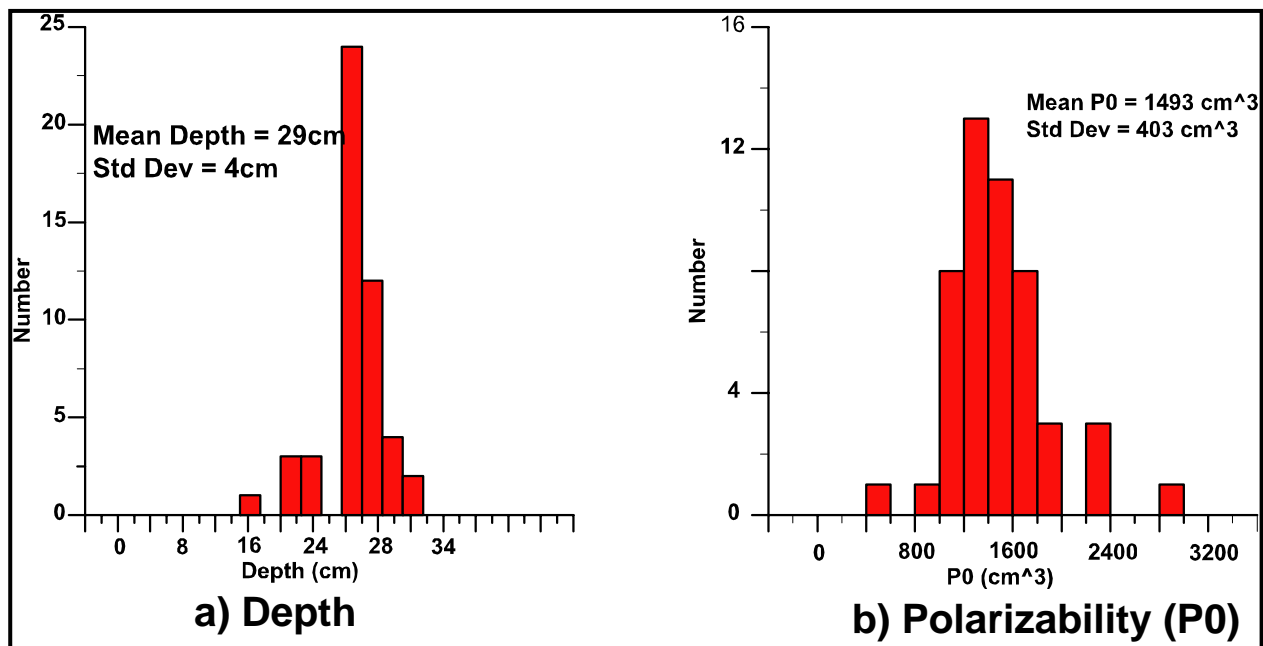


Figure 4.7: Histogram showing range of estimates of target depth and polarization amplitude (P_0) for a population of 49 8-lb shotputs located in the Calibration Lanes at Aberdeen.

around 1500 cm^3 , equivalent to a sphere radius of 4.9 cm. The ground truth we were given (20 cm depth to top of the shotput) would indicate that the centers of the spheres are at a depth of 25 cm. Thus our depth estimates are high by 5-7cm and our P_0 estimates will likewise be somewhat high. We measured the anomaly peak amplitudes (relative to the intermediate 12-21 composite gate noise floor) and found that the mean SNR for this anomaly population is 27 dB. This exercise gives us a benchmark statistic on depth estimates for compact targets at one given noise level. It seems safe for us to conclude that we get depth estimates that are good to within 20% (perhaps biased on the high side) with properly sampled anomalies having SNR in the 25-30 dB range.

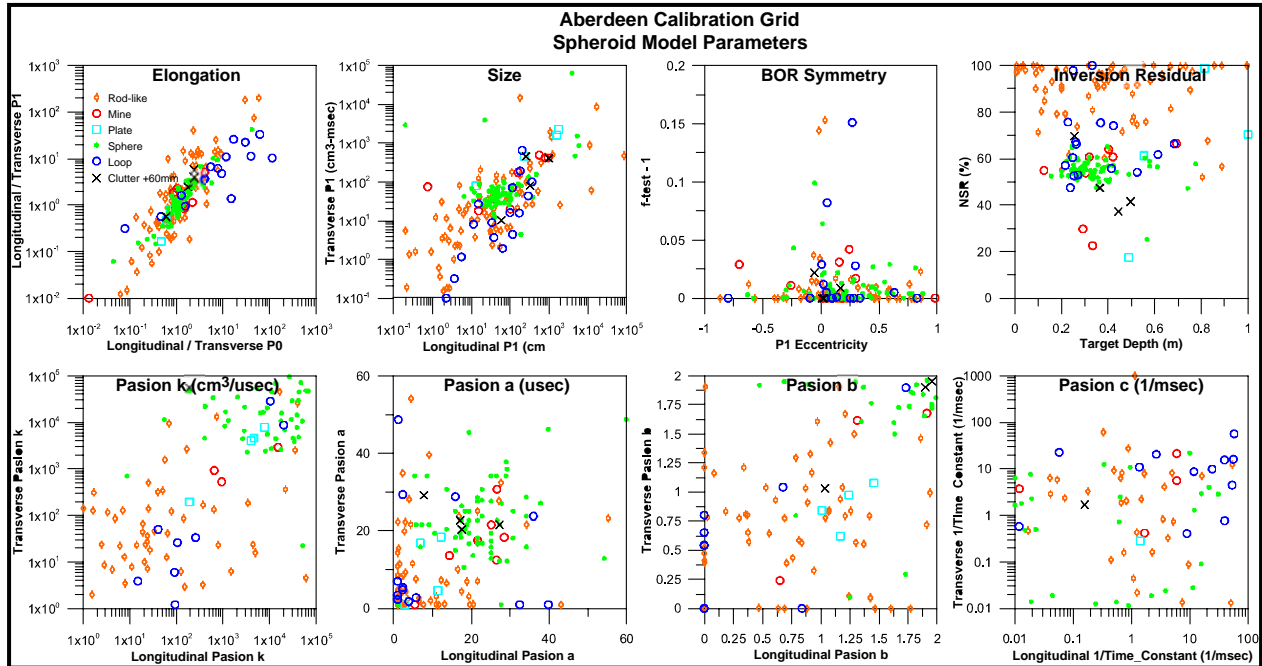


Figure 4.8: Model parameters from inversion of ATC Calibration Lane DNT Cart data with target (x,y,z,h,p,r) fixed at known values.

Aberdeen Parameterization Summary

Figure 4.8 summarizes the results of our model parameter estimates from inversion of Aberdeen Calibration Lane data. As indicated above, a large sample of 8 lb shotputs generates good statistics for the response of a permeable, conductive sphere. Longitudinal/transverse P_0 and P_1 seem to hold up as robust shape indicators for spheres, loops, and mines, although UXO with rod-like shapes have a wide distribution of ratio values. In Figure 4.8, we have used P_1 as the indicator of target size; P_0 (not shown in Figure 4.8) and Pasion k (lower left graph in Figure 4.8) are also good size indicators. Inversion residual noise/signal ratios (NSR) are high for all targets in the Calibration Lanes. The plot in the upper right, showing NSR versus target depth confirms what the map already tells us. That is, that with a few exceptions (e.g., T62 AT mines) the SNR level of the UXO target population in the Calibration Lanes is marginal for parameterization with models. As we have stated earlier in this report, the low SNR of the target population probably reflects a design objective on the part of ATC to test the limits of detection. To achieve that objective, ATC placed the targets at depths where the anomaly SNR is marginal

for good modeling results. Regrettably, that makes the data we acquired in the Calibration Lanes less useful for developing and testing methods for discrimination and classification. Having said that, however, our results show that many parameters, particularly the moments P_0 and P_1 and their ratios are sufficiently robust that they provide a useful basis for discriminating targets based on target shape and size. As we have demonstrated above, for the simple case of the 8 lb shotput population, the parameter f-test-1 (Sphere Model) is a robust indicator for objects with spherical symmetry. The importance of the f-test-1 parameter is reconfirmed by the **BOR Symmetry** plot in *Figure 4.8* where in this case, the ordinate parameter is f-test-1 (Spheroidal Model). As we stated in *Section 2.3.6*, the f-test-1 parameter is a χ -square statistic ratio on the constrained model. Discrimination based on f-test-1 is therefore similar to the approach outlined in the recent report by Nelson and others [27] on advanced discrimination techniques for use with the MTADS system.

Aberdeen Ranking Metric

The Classification phase of our demonstration at Aberdeen required that we submit a list of targets within 30 days after the completion of our fieldwork. The list was to include the coordinates of the target position, its amplitude, and a classification indicating whether the target is UXO or Clutter. In addition, the demonstration guidance required that we provide a rank for each reflecting our assessment of the probability that the target is UXO. During the initial interpretation of the Aberdeen data, we struggled with this concept of a target rank. Our difficulties were partly the result of our own inexperience with UXO classification and partly the result of an inadequate explanation of the requirement for the ranking metric. Consequently, we submitted target lists²² that used an expedient ranking metric based on interpretive judgment together with a penalty function based on the NSR parameter generated by the model fit in DNTDipole. That ranking metric is explained in more detail in *Section 3.6.6* and *Equation 3.1*.

Since we submitted our target lists in early October 2002, not only do we have a better understanding what was (is) required of a good ranking metric but also we have had a chance to fully study the data from the Calibration Lanes. As a result of our studies both of the Blossom Point data set as well as the data set from the Calibration Lanes at Aberdeen, we have started using multivariate analysis in an effort to derive ranking metrics that are appropriate for target classification. In *Section 2.3.7*, we applied the method to the Blossom Point targets using a **shaped-based** ranking metric. In an effort to improve on our initial target classification at Aberdeen, we have expanded on our use of multivariate analysis techniques to develop a ranking metric for Aberdeen.

Shape and Size Discrimination. For the specific target categories in the Aberdeen Calibration Lanes, classification can be improved by considering both shape and size. We divided the target parameter data from the Calibration Lanes into 19 groups and applied multiple discrimination analysis to compute parameter weights for shape- and size-based discrimination (*Table 4.6*).

Shape and size discrimination parameter $d1$ accounts for 54% of the discrimination power in Aberdeen Calibration Grid model parameters, $d1$ and $d2$ account for 76% of the power and $d1$ through $d5$ provide 99% of the discrimination by shape and size. All five discrimination parameters put heavy weight on $\log_{10}(P0_R)$, $\log_{10}(P0_1)$ and $\log_{10}(P0_2)$, suggesting that $P0$

²² We submitted separate target lists for the Blind Test Grid and for the Open Field.

is the most robust model parameter for size and shape discrimination between Aberdeen UXO types.

The RMS distance between an individual target's discrimination parameter values and group means can be used for classification. The target is placed in the group with the closest discrimination parameter mean. To provide a scalar ranking metric, discrimination parameter distance can be transformed to a probability. Histograms of RMS discrimination distances for Blossom Point and Aberdeen calibration data have a long-tailed shape fit reasonably well with exponential probability distributions. We map discrimination distances into relative probabilities of membership in each group. For the UXO versus clutter classification probability for each target, we combine the relative probability of the closest UXO group, p_{uxo_j} , and the closest clutter group, $p_{clutter_k}$, to estimate the probability of the target being a UXO.

$$p_{uxo} = \frac{100 \cdot p_{uxo_j}}{p_{uxo_j} + p_{clutter_k}} \quad \dots\dots\dots (2.8)$$

p_{uxo} varies from 100% if the target's discrimination parameters match a classification group mean exactly to 0% if it's discrimination parameters place it far away from any uxo classification groups. A p_{uxo} threshold can be used to select between categorization as UXO or Clutter.

Figure 4.9a is a scatter plot of the primary discriminants ($d1$, $d2$) for shape and size-based discrimination for targets in the Calibration Lanes. The discrimination ROC curve in Figure 4.9b shows how well targets in the Calibration Lanes at Aberdeen are classified as UXO as we vary the selection threshold from 100 to 0% p_{uxo} . Not surprisingly, including both target size and shape improves classification. Nearly 90% of the Aberdeen Calibration Lane UXO targets are classified correctly with a shape plus size p_{uxo} probability threshold of 50%. When applied to routine UXO surveys, the multiple discrimination analysis statistics used to classify targets

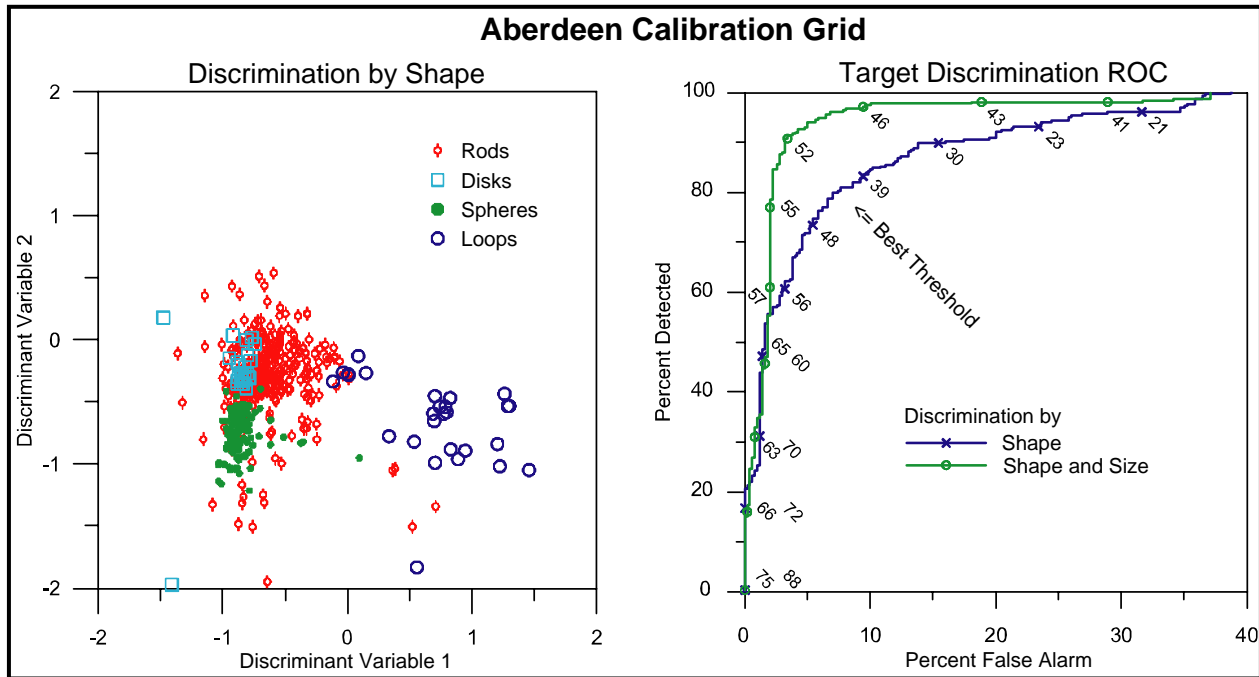


Figure 4.9: Target classification at ATC using Shape- and Size&Shape-based ranking metrics.

can be periodically updated as targets are recovered and the library of known targets grows. Although production UXO classification would generally use different groups (wire loops for example are specific to the Aberdeen test site), the methodology of multiple discrimination analysis together with mapping of RMS discrimination distances to probabilities that we have presented here is applicable. The selection of model parameters can also be varied depending upon the goals of the survey. A ranking metric specifically designed to identify mines, for example, would search for a disk-like shape, a shallow depth, and a vertical axis of symmetry for the longitudinal polarizability.

We obtain an additional improvement by adding a multiplicative term to lower p_{uxo} when inversion residuals indicate weak model-response signal with a high inversion NSR value. We have noted that the uncertainty in model parameter estimates increases significantly when NSR values are greater than about 75%. That observation can be formalized using the relation

$$f(NSR) = \frac{1}{1 + e^{\left(\frac{NSR - 22}{4}\right)}} \dots\dots\dots (4.4)$$

a function that stays close to one for NSR values less than 70%, drops to 0.5 at 90% and has a value of 0.08 when NSR = 100%. Multiplying p_{uxo} by $f(NSR)$ moves targets with high inversion NSR into the clutter category, because the associated observed data are dominated by background noise.

Table 4.6: Loading eigenvectors for shape and size based discrimination parameters.

Shape and Size Based Discrimination Parameters					
Model Parameter	d1	d2	d3	d4	d5
sphere/ellipsoid f-test	0	0	0	0	0
spheroid/ellipsoid f-test	0	0	0	0	0
loop/ellipsoid f-test	0	0	0	0	0
log ₁₀ (P0_R)	-0.5774	-0.5773	-0.5773	0.5773	0.5765
P0_E	0	0	0	0	0
log ₁₀ (P0_1)	0.5773	0.5773	0.5773	-0.5774	-0.5765
log ₁₀ (P0_2)	-0.5773	-0.5773	-0.5774	0.5773	0.5765
log ₁₀ (P1_R)	0.0007	0.0075	-0.0009	-0.0010	0.0311
P1_E	0	0	0	0	0
log ₁₀ (P1_1)	-0.0007	-0.0075	0.0009	0.0010	-0.0311
log ₁₀ (P1_2)	0.0007	0.0075	-0.0008	-0.0010	0.0311
PB_1	0	0	0	0	0
PB_2	0	0	0	0	0
PC_1	0	0	0	0	0
PC_2	0	0	0	0	0

4.3.2 The Blind Test Grid

ATC Scoring Report

Table 4.7: Summary of performance scores for the Blind Test Grid (after Table 6 in [43])

Metric				By Size			By Depth (m)		
	Overall	Standard	Non-Standard	Small	Medium	Large	< 0.3	0.3 to <1	>= 1
RESPONSE STAGE									
P_d	0.80	0.90	0.65	0.90	0.70	0.90	1.00	0.80	0.10
P_d Low 90 % Conf)	0.75	0.83	0.53	0.82	0.55	0.66	0.95	0.68	0.01
P_{fp}	0.90	-	-	-	-	-	0.90	0.90	1.00
P_{fp} Low 90 % Conf)	0.85	-	-	-	-	-	0.81	0.81	0.56
P_{ba}	0.50	-	-	-	-	-	-	-	-
DISCRIMINATION STAGE									
P_d	0.45	0.50	0.35	0.45	0.40	0.50	0.55	0.40	0.00
(P_d Low 90% Conf)	0.38	0.41	0.25	0.32	0.30	0.27	0.48	0.30	0.00
P_{fp}	0.50	-	-	-	-	-	0.50	0.45	0.50
(P_{fp} Low 90 % Conf)	0.42	-	-	-	-	-	0.42	0.35	0.14
P_{ba}	0.00	-	-	-	-	-	-	-	-

Response Stage Noise Level: 0.00

Recommended Discrimination Stage Threshold: 50.00

Only our target list for the Blind Test Grid has been scored thus far by ATC. The complete scoring report [43] is included in the Appendix (see file *ATC8642_SR37_BlindTestGrid.pdf*²³). Some of the performance grades are included in Table 4.2. For completeness, however, we have duplicated the complete summary table from the report as Table 4.7. The DNT system was the first to be demonstrated at the newly constructed Aberdeen demonstration site. Consequently, we have no baseline system with which we can compare our results. It is clear from these results that the overall P_d for the *response stage* is biased downward by poor performance in detecting targets buried deeper than 1m. With regard to the discrimination stage performance, we can only reiterate that our principal objective for the ESTCP project was to demonstrate the hardware system and not to demonstrate an advanced system for target classification. We had 30 days after the completion of our field demonstration in which to submit our target lists for both stages of scoring. Although we had developed model-based interpretation software (DNTDipole) to parameterize target properties and indeed we used to prepare our *discrimination stage* target lists, we were inexperienced in analyzing those model parameters to classify targets. Since that time we have refined our ability to interpret the target model parameters that are generated by DNTDipole. We have prepared a revised target list for the Blind Test grid wherein the target

²³ (June 8, 2004) The scoring report for the Open Field survey was not delivered to Zonge until May, 2004. At the request of ESTCP, we have added that report to the Appendix (see Appendix_ \2_Aberdeen Test Center\7_ATCScoringReports\ATC8675_SR38_Open Field 31804.pdf) without comment.

discrimination stage has been revised using multi-variant statistical analysis techniques that we described in this report (see sections 2.3.7 and this section). We hope to resubmit a revised target list reflecting our new approach to discrimination stage analysis. We trust that when this revised list is re-scored the results for the discrimination stage will significantly improve.

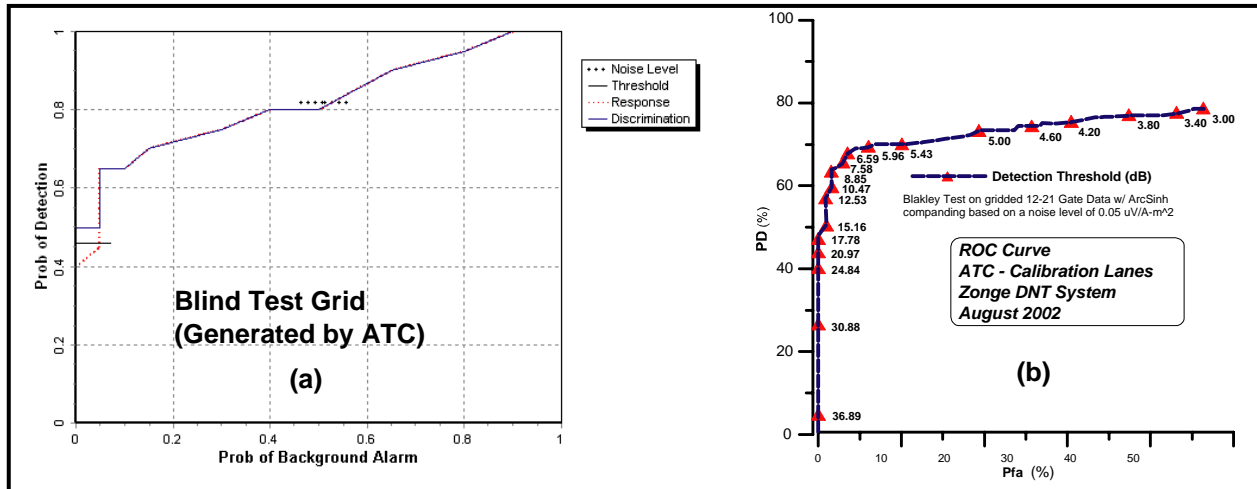


Figure 4.10: Response-stage ROC curves for the Aberdeen Standardized test site data. The curve for the Blind Test Grid (a) was generated by ATC. The Calibration Lane curve (b) was generated by Zonge.

Response Stage Performance - Figure 4.10a shows the ROC curve generated by ATC based on ground truth (unknown to Zonge) for the Blind Test Grid. The curve is rather coarse, but to our eyes, it exhibits a sharp knee at about $P_d=70\%$ with a $P_{ba}=15\%$. These results are consistent with our in-house ROC analyses (response stage only) based data acquired over the Calibration Lanes (Figure 3.2) and ground truth provided by ATC. We show that ROC curve in Figure 4.10b.

As we stated in our demonstration test plan [44], the over-riding performance objective for this demonstration was to "... demonstrate that early time multi-component TEM measurements significantly enhance the value of broadband EMI measurements for UXO classification." Until we know the performance results from other systems, we cannot make conclusions about whether or not we have met our primary objective. We are disappointed (but not surprised) that our overall P_d score for the response stage is not higher. The ROC curve that we generated from the Calibration Lanes (Figure 4.10a) suggested that our P_d score would be approximately 70% long before we received our formal scores.

Discrimination Stage Ranking Using Multivariate Statistics

We applied both our shape and shape plus size discrimination to model parameter estimates from inversion of Aberdeen Blind Test Grid data. Figure 4.10 compares results from the two discrimination methods in a two-dimensional scatter plot.

Categorization by shape into the four shape groups (rods, plates, spheres and loops) is indicated by posted symbol shape and color. Categorization by shape and size into more refined grouping by ordnance caliber and clutter type is indicated by posted numbers ranging from 1 to 19. A key on the left side of Figure 4.10 gives the correspondence between posted numbers and ordnance type. The figure's horizontal axis is the shaped-based ranking metric and its vertical axis is the shape and size based ranking metric. There is fairly good correlation between the two ranking methods, with a correlation coefficient of 0.67 between the two ranking metrics. Discrimination

by shape and size should be more accurate than discrimination by shape alone when there is a well-defined group of possible UXO and clutter items. Discrimination by shape only may have its place in situations when there are many possible UXO types or possible UXO types are unknown. Shape discrimination assumes that UXO will have rod-like shapes and that clutter will be disk-like or irregular.

The original target lists that we submitted for the Aberdeen grids were based on subjective interpretation of target polarizability transients. We expect that target categorization by multiple discriminant analysis of model shape and size parameters will be significantly more effective.

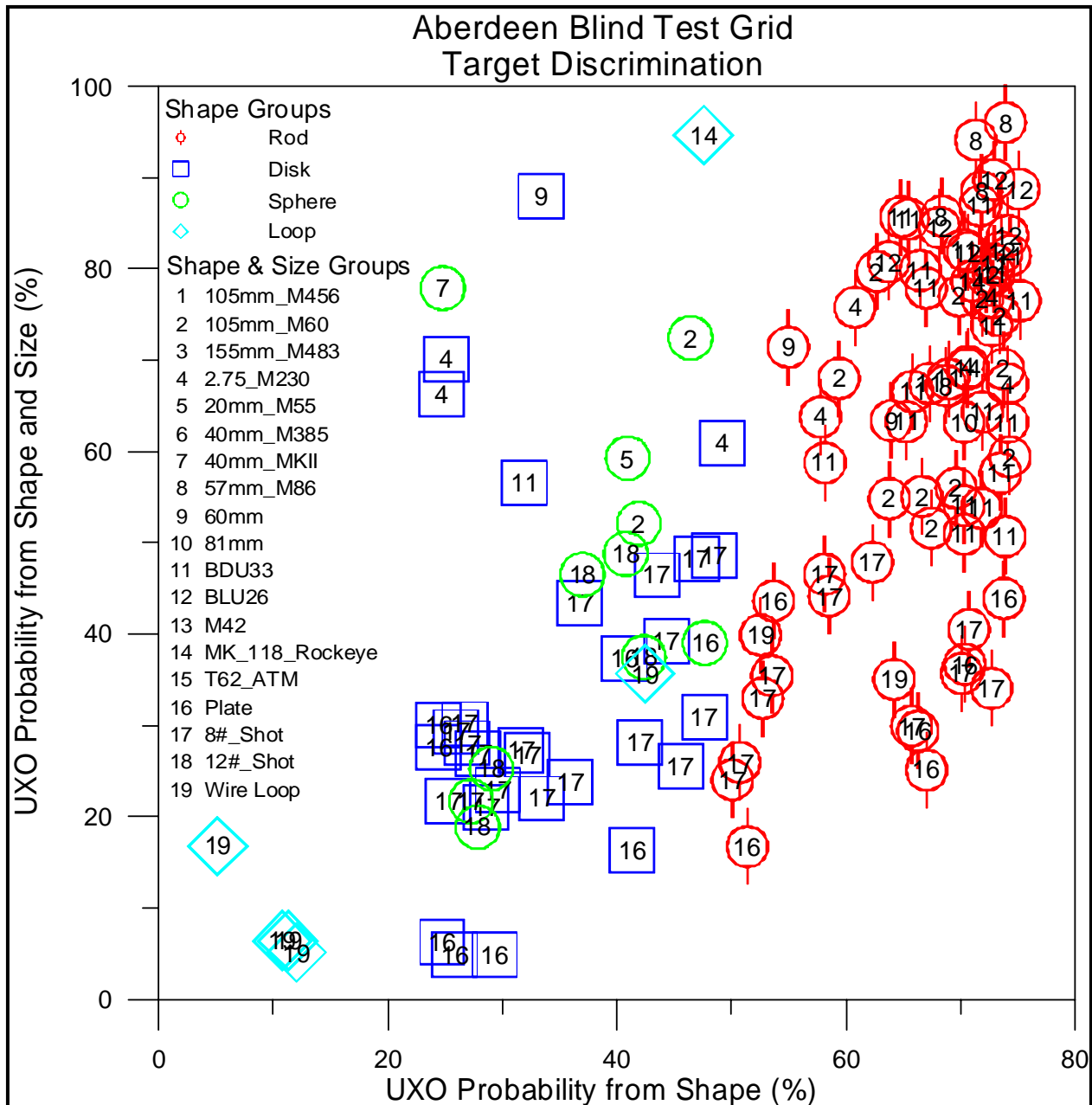


Figure 4.11: Aberdeen Blind Test Grid target discrimination by shape (color symbols) and discrimination by shape+size (posted numbers).

Although we have submitted a revised Aberdeen Blind Test Grid target list for scoring, those test results are not yet available for inclusion in this report.

4.3.3 The Open Field

We analyzed over 1500 targets that we detected in the open field area at Aberdeen using the methods we have explained in some detail in *Sections 2 and 3*. As we have explained above, we based our submittal for the classification phase on a very subjective ranking system that used the model-fit NSR parameter to de-rate the score according the quality of the model fit. We are waiting to receive our score for both the Open Field and for the Blind Test Grid.

5. COST ASSESSMENT

The costs involved in conducting the demonstration at the Standardized Site at the ATC are very useful in estimating both the productivity and the costs involved in the routine implementation of the DNT technology. *Table 5.1* lists the total costs that Zonge incurred from activities related to preparation, mobilization/demobilization, data acquisition, and data processing for this demonstration.

Table 5.1: ATC Demonstration Expenses

Cost Category	Labor	Travel & Per Diem	Misc. Fld Expenses	Shipping	Equip. Amort	Totals
Mob/Demob	\$4,680	\$3,299	\$349	\$2,134		\$10,462
Field Data Acquisition	\$20,234	\$5,195	\$600		\$2,550	\$28,579
Data QC & Interpretation	\$36,952					\$36,952
Totals	\$61,866	\$8,494	\$949	\$2,134	\$2,550	\$75,993

A few comments on the demonstration costs listed above are warranted since they impact on our projections of costs for a similar job as this technology is being implemented commercially. The cost of this demonstration is higher than what we project a similar job will cost in the future. The labor charge is inflated for all Cost Categories because of the involvement of the Principal Investigator (Snyder) in all phases of the operation and the involvement of the Principal Scientist (MacInnes) in Data QC and Interpretation category. In regard to the latter, there was a significant amount of software development being conducted during the 30-day period between the demobilization of the crew (9/2/03) and the deadline for the submission of our target lists (10/2/03). Partially offsetting the high labor costs, however, is the fact that the charge for the amortization of capital equipment does not fairly reflect the cost of that equipment. We believe that the cost of Data QC and Interpretation can easily be reduced by a factor of 50% in routine deployment. Similarly, we can expect reductions of approximately 20% and 10%, respectively, in labor costs for data acquisition, and mobilization and demobilization during a routine deployment of the technology. The cost of the demonstration was approximately \$12K/ha (\$4.8K/acre).

Table 5.2: Estimated job costs for a hypothetical DNT survey of a 6 ha (15 acre) site

Cost Category	Labor	Travel & Per Diem	Misc. Exp	Shipping	Equip Amort	Totals
Preparation	\$1,220		\$220			\$1,440
Mobilization	\$1,400	\$1,375		\$1,320		\$4,095
Field Data Acquisition	\$20,996	\$7,837	\$1,870		\$8,775	\$39,478
Data QC & Interpretation	\$6,629					\$6,629
Demobilization	\$1,071	\$1,265		\$1,320		\$3,656
Totals	\$31,316	\$10,477	\$2,090	\$2,640	\$8,775	\$55,298

We have re-figured the costs for a hypothetical 6 ha (~15 acre) job similar to the ATC Standardized site. The costs are based on an average daily production of 0.4 ha/day (1 acre/day) with a crew of three people in which the Principal Investigator has been replaced with a Site Geophysicist. Likewise, the responsibility for data QC and interpretation has been devolved to a Sr. Staff Geophysicist.²⁴ Note however, that we have increased the travel expenses to reflect

²⁴ The Project Geophysicist will continue to be responsible for initial field QC before the data are transported to the Zonge office for complete processing and interpretation by the Sr. Staff Geophysicist

working a 5-day work week, and we have added cost for amortization of capital equipment.²⁵ We report those costs in *Table 5.2*.

Table 5.2 suggests that were we to now treat the demonstration survey at ATC as a routine job, we can reduce the total survey cost by 13% or more. Moreover, these estimates suggest that the incremental cost of data acquisition and interpretation (i.e., cost per area exclusive of preparation, mobilization, and demobilization) is \$7.7K/ha (\$3.1K/acre).

5.1 BASELINE SYSTEM COST COMPARISON

The field services division of Zonge Engineering has conducted a number of UXO site surveys using the baseline system, the EM-61. Therefore, we are in an excellent position to compare the operating costs of acquiring EM-61 data for both detection and shape-based interpretation. As we indicated in *Section 3* of this report, we regard the EM-61 MkII as a baseline system against which we can compare the performance of DNT. In making that comparison, we accept the NRL's conclusion that satisfactory modeling requires that the area under investigation be surveyed twice with orthogonal surveys [27].

We have had recent experience with the interpretation of EM-61 MkII data with our proprietary modeling program *DNTDipole*. We treat the 4 time gates acquired from the coincident receiver as a coarsely sampled TEM transient. Thus the EM-61 MkII can be treated as a single-component multi-gate system – sort of a poor-man's EM-63. The capital cost of the EM-61 MkII is considerably less than that of the DNT system (\$20K versus \$50K) and this reduces the daily operating cost by approximately \$200/day. Offsetting the lower equipment cost is the need to survey the area twice (in orthogonal directions) to adequately sample target anomalies to permit satisfactory shape-based modeling and discrimination.

Table 5.3 contains a cost-breakdown for the hypothetical 6 ha survey that we previously estimated with the DNT system (*Table 5.2*) but now surveyed in orthogonal directions with the EM-61 MkII and processed both for target detection and target classification using DNT processing software. These tables confirm that regardless of how the equipment is amortized, the main cost element in these UXO surveys is the cost of labor. If we ignore for the moment the obvious performance advantages for classification of the DNT system, the added cost for the EM-61 MkII survey when deployed for both detection and shape-based classification is due almost entirely to the need for double the survey coverage. To put it another way, single-coverage (i.e., profiles in a single direction) with EM-61 MkII survey works well for detection but will not permit reliable model-based interpretation. At the cost of an additional \$500/ha (\$200/acre), the DNT survey can be used for both detection and model-based interpretation.

Table 5.3: Estimated job costs for a hypothetical EM61 MkII (bi-directional) survey of a 6 ha (15 acre) site

Cost Category	Labor	Travel & Per Diem	Misc. Exp	Shipping	Equip Amort	Totals
Preparation	\$1,220		\$220			\$1,440
Mobilization	\$1,400	\$1,375		\$1,320		\$4,095
Field Data Acquisition	\$41,995	\$21,630	\$3,300		\$15,150	\$82,075
Data QC & Interpretation	\$10,606					\$10,606
Demobilization	\$1,071	\$1,265		\$1,320		\$3,656
Totals	\$56,292	\$24,270	\$3,520	\$2,640	\$15,150	\$101,872

²⁵ During the demonstration at ATC, we worked straight through thereby saving money on per diem expenses.

6. CONCLUSIONS AND RECOMMENDATIONS

During the course of this ESTCP project, we have demonstrated that the Zonge 4D NanoTEM technology greatly expands the capabilities of EMI beyond instruments such as the EM-61 that are now being routinely being deployed for UXO detection and classification. There is value added in both phases of UXO site characterization, for detection, as well as for classification.

At the operational level, we have shown that productivity in the field is comparable with that of competing man-portable systems. As we have pointed out, the capital cost for the DNT system is significantly higher than the EM-61. However, the cost differential is not as significant when DNT is compared with the multi-gate single component EM-63.

As results from Blossom Point have shown, the Zonge DNT system is only marginally less sensitive than the NRL's man-portable MTADS system. That system uses a modified EM-61 sensor with a somewhat higher transmitter moment than "off-the-shelf" models from Geonics. Hence, for practical purposes the DNT system gives up nothing in detection sensitivity to much simpler systems. Moreover, because DNT acquires TEM data a decade earlier in time, it is significantly more sensitive in detecting small targets that may be non-permeable. Admittedly, added detection sensitivity can be a blessing or a curse. At Aberdeen, for example, the system detected far more targets than were actually buried, probably because these items were not detected and removed before the site was seeded with known targets.

The multi-axis receiver capability of the DNT system adds significant value in several ways. The horizontal components, particularly the component transverse to the cart motion, helps to locate targets that are laterally offset from the profile line. This is particularly important in the case of a detection survey using 2-ft or 1-m lane separations. In such cases, the transverse horizontal component can be used qualitatively to determine which side of the profile the target lays. But we were unable to demonstrate that the horizontal component data improved our target parameterization or classification. Model studies, and indeed an excellent study performed by Grimm [50] based on static measurements, conclude that horizontal components significantly improve target classification. Our results do not support those conclusions. We ascribe the difference in our conclusion to higher noise levels that we characteristically observed on the horizontal components. Noise levels on static data are significantly lower due to synchronous stacking during data acquisition. The numerical modeling studies of which we are aware all appear to apply a uniform noise level to all three components. An important result of our efforts to show that there is "added value" in the horizontal components is that we conducted a small survey using a YZZ receiver coil (1 horizontal receiver oriented transverse to the direction of cart travel together with 2 vertical receivers one above the other). Our comparative analyses of the YZZ data with XYZ data acquired on the same day with the same equipment suggest that the YZZ receiver antenna is better than either a single Z antenna, a ZZ antenna, or an XYZ antenna.

The 4D acquisition capability of the DNT system cannot be realized without an integrated system of processing software. Geosoft's Oasis Montaj, provides the central core of that software, with its data base structure, its ability to handle array channels, and its built-in provisions to display profiles and/or maps. We have supplemented standard capabilities within Oasis with our own custom software in the form of GX's and loosely integrated software programs such as *DNTReduce* and *DNTDipole*. Clearly, however, without the DNT software, the ability of the DNT system to acquire 4D data sets would remain unused. We trust that the examples included in the body of this report together with all of the supporting graphics and data

contained in the *Appendix* demonstrate conclusively that the software tools are available to handle the added dimensionality of the data.

There are a number of areas in which further research should lead to improvements in the DNT system. Increasing effective transmitter moment by using more transmitter loop turns would sacrifice some quality in early time data, but would reduce noise levels and improve late-time data quality. Lower noise levels will increase SNR at longer transient delay times and will improve the ability to discriminate between small targets, often fragmentation clutter, and larger intact UXO.

Three-component data and the DNT system's high sample rate produces large data sets with large redundancy. We have observed that background noise levels in the horizontal components are greater than in the vertical component and that noise is often highly correlated between receiver loop components. We also noted that we believe that these higher noise levels in the horizontal components degrades if not outright destroys the value of these horizontal components when included in our model analyses. Coherent noise is particularly evident in our Fort Ord data, which is afflicted by strong synchronous noise that dominates the horizontal component response and is evident in the vertical component. Spies [34] describes an adaptive filtering algorithm which reduces noise in vertical component TEM data by using the correlation between noise between orthogonal receiver loop components. Similar ideas could be adapted to the special case of our DNT system and should significantly reduce background noise levels in many situations.

Another way to take advantage of the high redundancy in DNT data sets is to use a specialized matched filter to combine data from all three receiver loop components and from a patch of measurements to spherical target polarizability $P0$ (cm^3) or polarizability first moment, $P1$ ($\text{msec}\cdot\text{cm}^3$). The approach will be computationally intensive, but will collapse data from 31 time windows, three components and hundreds of measurement locations to a single scalar value with positive peaks over the most likely UXO target locations. The weighted averaging of thousands of measurements into a single scalar value should reduce noise levels considerably.

Interference from the over abundance of 8 lb shotput markers in the Aberdeen Calibration Grid highlights the need for modeling routines that can cope with overlapping anomalies. **DNTDipole** could be extended to simultaneously invert data from large data patches to groups of point-dipole models, including the effects of overlapping anomalies in the modeling calculations and improving results in areas with closely spaced targets.

We have made a good start on methods for target categorization using multiple discriminant analysis, but the approach can be improved. Discriminant analysis assumes Gaussian probability distributions that are often inappropriate due to the presence of outlier model-parameter values. Multinomial logistic regression may be more effective because it does not require normally distributed variables and does not assume homoscedasticity²⁶.

DNTDipole's inversion to libraries of UXO types depends upon having good estimates for prototypical model parameter values. Model parameter statistics for target discrimination would be improved by tabulating high-quality free-air measurements for a variety of UXO calibers. We

²⁶ The assumption that the variability in scores for one variable is roughly the same at all values of the other variable (all variables are normally distributed).

had neither the time nor the funding to initiate a program to systematically characterize a set of targets using static free-air measurements. We believe that such a program would produce dividends not only for our own efforts to understand and document the response parameters of various genres of UXO and clutter, but also the efforts of others. In this regard, we note that the NRL and AETC have collected and documented the broadband response of a large number of targets in the frequency domain using the GEM-3 instrument. An effort to do likewise in the time-domain is likely to be useful. At some point, moreover, we will be able to convert broadband frequency domain measurements to multi-gate TEM measurements and vice versa.

7. IMPLEMENTATION ISSUES

The technology that has been demonstrated under this ESTCP contract is non-intrusive and the environmental impact of its deployment at a particular site is confined to problems and/or needs of a number of field personnel while conducting a typical field survey operation. The antenna cart is extremely light and after 24 hours there will be no discernible evidence that a survey has ever been conducted over an area. One might say, therefore, that the greatest impact from the survey comes from the field people who must systematically push the antenna cart over every part of the area much like mowing the lawn. To our knowledge, there are no pertinent environmental regulations, with the exception of anti-litter laws, that relate to conducting this type of field survey. The only permit that may be required is permission to access the site from the appropriate jurisdictional authority. And, as far as we know, there are no other regulatory issues.

The end-users for this technology will consist of state and federal agencies, military organizations, and private engineering organizations that conduct geophysical site investigations to detect buried metal objects in general, and UXO in particular. On face of it, DNT technology is no different from the metal detection TEM technology (e.g., Geonics EM-61) that is widely accepted and frequently specified for routine UXO site surveys. The DNT system greatly expands on the capabilities of the technology that is already routinely deployed. As we have explained here in this report, we have customized the DNT technology by building a special antenna array, by modifying our acquisition software to permit dynamic data acquisition at a high effective sample rate, and by developing the software tools required to exploit the additional dimensionality provided in the DNT data. The hardware (i.e., the NT-32^{II} transceiver) in the form that we have demonstrated at Blossom Point and at Aberdeen has been available as a standard Zonge product for approximately 3 years. Moreover, the Zonge NanoTEM system has an 11-year history of successful application to many other problems in shallow mining exploration and environmental site investigations. A complete DNT system is available for rent or purchase from Zonge even as we complete this report. Moreover, Zonge Engineering has a 30-year history of conducting field surveys worldwide in all types of environments. In short, this technology is available not only to those wishing to own or rent the equipment and operate it on their own but it is also available as a service.

8. REFERENCES

1. DERP, *Fiscal Year 2001 DERP Annual Report to Congress*. 2001, U.S. Department of Defense: Washington, DC.
2. OADUSD, E.C., *Fiscal Year 2000 BRAC Cleanup Plan Abstract Analysis*. 2000, U.S. Dept. of Defense: Washington, DC. p. 36+.
3. ODUSD, E.S., *Unexploded Ordnance (UXO)*. 1999, U.S. Dept. of Defense.
4. ODUSD, I.E., *Management Guidance for the Defense Environmental Restoration Program*. 2001, U.S. Dept. of Defense: Washington, DC. p. 92.
5. Barrow, B., and H. H. Nelson, *Model-Based Characterization of Electromagnetic Induction Signatures Obtained with the MTADS Electromagnetic Array*. IEEE Trans Geosci & Rem. Sensing, 2001. **39**(6): p. 1279-1285.
6. Bell, T.H., Bruce J. Barrow, and Jonathan T. Miller, *Subsurface Discrimination Using Electromagnetic Induction Sensors*. IEEE Trans Geosci. & Rem Sensing, 2001. **39**(6): p. 1286-1293.
7. Nelson, H.H., J.R. McDonald, and Richard Robertson, *Design and Construction of the NRL Baseline Ordnance Classification Test Site at Blossom Point*. 2000, Naval Research Laboratory: Washington, DC. p. 13.
8. Robitaille, G.E. *UXO Technology Standardized Demonstration Sites*. 2001. Partners in Environmental Technology 2001: SERDP/ESTCP.
9. Snyder, D.D., David C. George, Scott C. MacInnes, and Kenneth L. Zonge. *Demonstration of a Fast 4D TEM System at the NRL Baseline Ordnance Test Site*. in *UXO/Countermining Forum 2002*. 2002. Orlando, FL: U.S. Dept. of Defense.
10. MacInnes, S.C., Donald D. Snyder, and Kenneth L. Zonge. *Physics-Based Characterization of UXO from Multi-Component TEM Data*. in *UXO/Countermining Forum*. 2002. Orlando, FL: U.S. Dept. of Defense.
11. Nabighian, M.N., and James C. Macnae, *Time Domain Electromagnetic Prospecting Methods*, in *Electromagnetics in Applied Geophysics*, M.N. Nabighian, Editor. 1991, Soc. Expl. Geophys.: Tulsa, OK. p. 427-520.
12. Frischknecht, F.C., *Electromagnetic Physical Scale Modeling*, in *Electromagnetic Methods in Applied Geophysics - Theory*, M.N. Nabighian, Editor. 1988, Soc. Explor. Geophys.: Tulsa, OK. p. 365-441.
13. Carlson, N.R., C.S. Lide, and K.L. Zonge. *A New Shallow-Sounding TEM Method for Vados Zone Monitoring (Abs.)*. in *85th Annual Mtg, Joint Sess. Am Soc Agron, Crop Sci. Soc. Am., & Soil Sci. Soc. Am.* 1993. Cincinnati, OH.
14. Carlson, N.R., and K. L. Zonge. *Case Histories of Buried Borehole Detection: An Exercise in Flexibility*. in *SAGEEP 1996*. 1996. Keystone, CO: Environ. Eng. Geophys. Soc.

15. MacInnes, S., Jon Durham, John Dickerson, Skip Snyder, and Ken Zonge. *Fast TEM for UXO Mapping at Gambell, Saint Lawrence Island, Alaska.* in *UXO/Countermining Forum*. 2001. New Orleans Marriott: U.S. Dept. of Defense.
16. Carlson, N.E., and Kenneth L. Zonge. *The utility of horizontal component measurements in random-walk TEM measurements.* in *SAGEEP 2003*. 2003. San Antonio, TX: Environ. Eng. Geophys. Soc.
17. Zonge, *Demonstration at BP ... (Revised)*. 2002, Zonge Engineering & Research Organization, Inc: Tucson Arizona.
18. Nelson, H.H. *Careful Timing is the Key to Sensor Location Precision.* in *UXO/Countermining Forum*. 2001. New Orleans: U.S. Dept. of Def.
19. Papoulis, A., *The Fourier Integral and Its Application*. 1962, New York: McGraw-Hill Book Company, Inc.
20. Gold, B., and Charles M. Rader, *Digital Processing of Signals*. 1969, New York: McGraw-Hill Book Company.
21. Aseltine, J.A., *Transform Method in Linear System Analysis*. 1958, New York: McGraw-Hill Book Company, Inc.
22. Leick, A., *GPS Satellite Surveying*. 1999, New York: Wiley.
23. Parkinson, B.W., and P.K. Enge, *Differential GPS*, in *Global Position System: Theory and Applications*, B.W. Parkinson, Editor. 1996, Am. Inst. of Aero. & Astro., Inc. p. 3-50.
24. Das, Y., John E. McFee, Jack Toews, and Gregory C. Stuart, *Analysis of an Electromagnetic Induction Detector for Real-Time Location of Buried Objects*. IEEE Trans. Geosci. & Remote Sensing, 1990. **28**(3): p. 278-288.
25. Pasion, L.R., and Douglas W. Oldenburg. *Locating and Determining Dimensionality of UXOs Using Time Domain Electromagnetic Induction*. in *SAGEEP 1999*. 1999. Oakland, CA.
26. Smith, R.S., and T.J. Lee, *The moments of the impulse response: a new paradigm for the interpretation of transient electromagnetic data*. Geophysics, 2002. **67**(4): p. 1095-1103.
27. Nelson, H.H., T.H. Bell, J.R. McDonald, and B. Barrow, *Advanced MTADS Classification for Detection and Discrimination of UXO*. 2003, Naval Research Laboratory: Washington, D.C. p. 53.
28. Grant, F.S., and G.F. West, *Interpretation Theory in Applied Geophysics*. 1965, New York: McGraw-Hill Book Company.
29. Pasion, L.R., and D.W. Oldenburg, *A Discrimination Algorithm for UXO Using Time Domain Electromagnetics*. Jour. Eng. & Envir. Geophys., 2001(28): p. 91-102.
30. Davis, J.C., *Statistics and Data Analysis in Geology*. 1986, New York: John Wiley & Sons.
31. Mauldin-Mayerle, C., Norman R. Carson, and Kenneth L. Zonge. *Environmental Application of High Resolution TEM Methods*. in *The 4th Meeting on Environmental and Engineering Geophysics*. 1998. Barcelona, Spain: European Section, EEGS.

32. Carlson, N.R., and Kenneth L. Zonge, *Early-time, Multi-component Mobile TEM for Deep Metal Detection*. in *SAGEEP 2002*. 2002. Las Vegas, NV: EEGS.
33. Asch, T., Tamir L. Klaff, Craig Murray, Edward G. Staes, and Gregg Peterson. *An Overview of the Ordnance Detection and Discrimination Study at Former Ford Ord, California*. in *SAGEEP 2002*. 2002. Las Vegas, NV: Environ. & Eng. Geophys. Soc.
34. Spies, B.R., *Local noise prediction filtering for central induction transient electromagnetic sounding*. *Geophysics*, 1988. **53**(8): p. 1068-1079.
35. Bell, T., Bruce Barrow, Jonathan Miller, and Dean Keiswetter, *Time and Frequency Domain Electromagnetic Induction Signatures of Unexploded Ordnance*. *Subsurface Sens. Tech. Appl.*, 2001. **2**(3): p. 153-175.
36. Robitaille, G. *Standardized UXO Technology Demonstration Sites Program*. in *The UXO/Countermines Forum 2002*. 2002. Orlando, FL: U.S. DoD.
37. USAEC, *Standardized UXO Technology Demonstration Site*. 2002, U.S. Army Environmental Center.
38. McDonald, J.R., and H.H. Nelson, *Man-Portable Adjuncts for the MTADS*. 2001, Naval Research Laboratory: Washington, DC. p. 60.
39. Nelson, H.H., and Bruce Barrow, *Electromagnetic Induction and Magnetic Sensor Fusion for Enhanced UXO Target Classification*. 2000, Naval Research Laboratory: Washington, DC. p. 35.
40. Smythe, W.R., *Static and Dynamic Electricity*. 3rd ed. 1968: McGraw-Hill Book Company. 623.
41. Hill, D.A., and J.R. Wait, *EM transient response of a small wire loop buried in a homogeneous conducting earth*. *Pure & Appl. Geophys*, 1973. **105**: p. 869-878.
42. DeMaw, D., *The Radio Amateur's Handbook*. 47th ed. 1970, Newington, Conn.: The American Radio Relay League. 611.
43. Bell, T., Bruce Barrow, Jonathan Miller, and Dean Keiswetter, *Time and Frequency Domain Electromagnetic Induction Signatures of Unexploded Ordnance*. *Subsurface Sens. Tech. Appl.*, 2001. **2**(3): p. 153-175.
44. Carlson, N.R., and Kenneth L. Zonge, *Early-time, Multi-component Mobile TEM for Deep Metal Detection*. in *SAGEEP 2002*. 2002. Las Vegas, NV: EEGS.
45. Carlson, N.E., and Kenneth L. Zonge. *The utility of horizontal component measurements in random-walk TEM measurements*. in *SAGEEP 2003*. 2003. San Antonio, TX: Environ. Eng. Geophys. Soc.
46. Zonge, E.R.O., *UXO Characterization with a Fast 4-D TEM System: Blossom Point Tests*. 2002, Zonge Engineering & Research Org: Tucson, AZ. p. 39.
47. MacInnes, S.C., D.D. Snyder, D.C. George, and Kenneth L. Zonge. *Model-Based UXO Classification Based on Static 3-Component TEM Measurements*. in *SAGEEP 2002*. 2002. Las Vegas, NV: Environ. & Eng. Geophys. Soc.

48. Smith, J.T., and H.F. Morrison, *Estimating Equivalent Dipole Polarizabilities for the Inductive Response of Isolated Conductive Bodies*. submitted to IEEE Trans. Geosci. Remote Sensing, 2002.
49. Smith, J.T., H. Frank Morrison, and Alex Becker, *Resolution Depths for Some Transmitter Receiver Configurations*. submitted to IEEE Trans. Geosci. Remote Sensing, 2002.
50. Grimm, R.E., *Triaxial Modeling and Target Classification of Multichannel, Multicomponent EM Data for UXO Discrimination*. Jour. Environ. & Eng. Geophys., 2003. **Accepted for Publication.**

9. POINTS OF CONTACT

Contact	Organization	Telephone	FAX	E-Mail	Role
Zonge					
Dr. D.D. "Skip" Snyder	Snyder Geoscience, Inc 3870 N River Oak Lane Tucson, AZ 85718	(520) 529-9169	N/A	SkipS@worldnet.att.net	Principal Investigator
Dr. Scott C. MacInnes	Zonge Engineering & Research 3322 E Fort Lowell Rd Tucson, AZ 85716	(907) 262-5072	N/A	zonge@alaska.net	Principal Scientist
Dr. Jennifer Hare	Zonge Engineering & Research 3322 E Fort Lowell Rd Tucson, AZ 85716	(520) 327-5501	(520) 325-1588	jennifer@zonge.com	Sr. Geophysicist
Dr. Kenneth L. Zonge	Zonge Engineering & Research 3322 E Fort Lowell Rd Tucson, AZ 85716	(520) 327-5501	(520) 325-1588	ken@zonge.com	President, Zonge Engineering
ESTCP					
Dr. Jeffrey Marqusee	901 E Stuart St. Arlington, VA 22203	(703) 396-2120	(703) 696-2114	Marqusee@acq.osd.mil	ESTCP Director
Dr. Anne Andrews	901 E Stuart St. Arlington, VA 22203	(703) 696-3826	(703) 696-2114	Anne.Andrews@osd.mil	ESTCP, UXO Proj. Mgr
NRL					
Dr. Herb Nelson	U.S. Naval Research Laboratory Chemistry Division, Code 6110 Washington, DC 20375-5342	(202) 767-3686	(202) 404-8119	Herb.nelson@nrl.navy.mil	Head, Molecular Dynamics Section
Mr. Jack Kaiser		(301) 870-2329	(301) 870-3130	jkaiser@arl.mil	Site Manager, Blossom Point
ATC					
George E. Robitaille	U.S. Army Environmental Center SFIM-AEC-ED APG, MD 21010	(410) 436-6865	(410) 436-3836	George.robitaille@aec.apgea.army.mil	Prog. Mgr, UXO Tech. Demonstration & Validation
Larry Overbay	U.S. Aberdeen Test Center 400 Collieran Rd APG, MD 21005-5059				ATC, Standardized UXO Technology Demonstration Site

SIGNATURE

Donald D. Snyder, III
Principal Investigator

Date

APPENDIX

Data CD contents

Root Directory	Final Draft Report	<i>F4DTEM_Final_Draft.pdf</i>
	Zonge GDP-32^{II} equipment brochure	<i>Gdp32ii.pdf</i>
	Zonge NT32 equipment brochure	<i>Nt32.pdf</i>

Directory – 1_Blossom Point

Blossom Point Report		<i>BPReport.pdf</i>
1_Ground Truth		<i>BP Baseline Area Layout Final.rtf</i>
2_Raw Data		<i>(separate DDS CD)</i>
3_Model Data	Polarization plots for each target	<i>BP_NS_PolPlts.PDF</i>
	Model parameters for each target	<i>BP_NSd_mod.csv</i>

Directory – 2_Aberdeen Test Center

1_Ground Truth	Calibration Lanes	<i>ATC Calibration Lanes.xls</i>
2_Raw Data		<i>(separate DDS CD)</i>

3_Model Data We have included the polarizability plots and the parameters, respectively, as a PDF file and an *_mod.csv file for both the Calibration Lanes and the Blind Test Grid. We have not provided those data for the Open Field Area.

1. Calibration Lanes

2. Blind Test Grid

4_Target Lists This directory contains the target lists that we submitted to ATC for scoring in early October 2002. The classification rank was subsequently modified to meet ATC requirements for automatic scoring. We also include a second revision to the target list for the Blind Test Grid.

1. Blind Test Grid

- a. Target list scored by ATC *Zonge_BLIND_TEST_GRID-RevisedRank.xls*
The word “Revised” refers to a simple mathematical manipulation of our original ranks so that the rank would be compatible with ATC’s computerized scoring routine. That revision was done in early November, 2002.

- b. Target list, revised discrimination stage ranks

Zonge_BLIND_TEST_GRID_Revised18March03.xls

We revised this list during the writing of this report to reflect discrimination according to shape & size as explained in Section 4. We plan to resubmit this to ATC for a re-score.

2. Open Field Area

Zonge_ATC_Open_Field-RevisedRank.xls

This is the target list scored by ATC. The word “Revised” refers to a simple mathematical manipulation of our original ranks so that the rank would be compatible with ATC’s computerized scoring routine.

